Spectroscopic analysis of modern Mg-carbonates from multiple mafic/ultramafic environments with relevance to Jezero crater, Mars

By

Nathalie Turenne

A Thesis submitted to the Faculty of Grad Studies in partial

fulfillment of the requirements for the Master of Science degree.

Department of: Environmental Science and Geography

Program: Masters of Science in Environmental and Social Change

The University of Winnipeg

Winnipeg, Manitoba, Canada

April, 2023

30   **Keywords:** Mars, Microbialites, Carbonates, Spectroscopy, Jezero crater.

31   **Abstract**

32   The detection and presence of carbonates on Mars and within Jezero crater implies and

33   supports an extensive aqueous history during the Noachian to early Hesperian and can help with

34   the reconstruction of paleoenvironments. Mg-carbonates have been identified using in-situ

35   spectroscopic instruments on board the Mars Perseverance Rover in the mafic and ultramafic

36   Máaz and Séítah units implying a potential past habitable environment. The goal of this study

37   was to conduct a multi-instrument examination of magnesium carbonates formed at several

38   terrestrial ultramafic and mafic sites and assess their relevance to the exploration of Jezero crater

39   on Mars. In this study we demonstrate the unique spectral features using a suite of spectroscopic

40   instruments of the microbialite samples from the Atlin playas, Clinton Creek, Lake Alchichica,

41   and Lake Salda analogue sites with relevance to Mars. The results of this study determined the

42   presence of magnesite, hydromagnesite and aragonite being the dominant mineralogy present.

43   The reflectance was determined to be the most useful spectroscopic instruments to identify

44   biological compounds while the Raman was determined to be most useful at identifying

45   mineralogy and comparing the microbialites to pure end members. From our study we have

46   determined the likely hypotheses for the current state of the Jezero crater bedrock to be

47   consistent with hydrothermal alteration and hypothesize lacustrine environments for the

48   formation of Marginal Carbonate unit. The use of analogue sites can help to indicate the

49   habitability of Mars and that the most successful determinant of Mg-carbonate formation on

50   Mars is to return the samples to Earth for further analysis.

51

52

53

54

55

56

57

58 **Co-authorship statement**

59   This thesis is based on a manuscript that will be submitted for publication in the journal

60 Icarus. I, Nathalie Turenne led the definition of the research problem, sample analysis, data

61 analysis, interpretation of the results, writing and will be the lead author of the manuscript. Ed

62 Cloutis, Ian Power, Dan Applin, Uriah Wolf, Andreas Beinlich, Hülya Alçiçek, Luisa I. Falcón

63 Stanley Mertzman contributed to the sample collection, data analysis, and interpretation of the

64 results and provided editorial guidance on the writing of the manuscript and will be co-authors.

65

66

67

68

69

70

71

72

73

74

75

76

77

78

79

80

81

Contents

133

134

135

136

137

138

139

140

141

142

143

List of Figures

List of Tables

251 **1. Introduction**

252   The purpose of this study was to analyse microbialite samples from several analogue sites

253 including the Atlin playas and bedrock, British Columbia, Canada, Clinton Creek, Yukon,

254 Canada, Lake Alchichica, Puebla State, Mexico and, Lake Salda, Turkey using rover-like

255 instruments. This study hypothesized the formation of Jezero crater bedrock to be consistent with

256 hydrothermal alteration. In addition to the formation of Mg-carbonates within the Marginal

257 carbonates to have formed through precipitation and evaporation processes. This study undertook

258 a multi-instrument approach of samples using analogues sites from diverse Mg-carbonate

259 deposits, including fluviolacustrine and playa environments. By characterizing Mg-carbonates

260 from diverse environments, using instruments similar to those on the Perseverance rover such as

261 VNIR (Visible Near-Infrared) and Raman spectrometers, to gain insights into the detectability

262 and characterization of these minerals and how their properties may link to formation conditions,

263 with a focus on Jezero crater. The goal of this study was to advance the abilities to detect and

264 characterize different Mg-carbonates on Mars, and the understanding of processes under which

265 Mg-carbonates can form and precipitate in mafic/ultramafic lacustrine environments. This study

266 conducted spectral measurements to determine and give insight into the ability of rover and

267 orbital spectral interpretations of Jezero crater. This study was conducted analysis using VNIR

268 and Raman spectra similar to the rover instruments, SEM elemental mapping was conducted to

269 determine regions of high Ca vs Mg amounts. XRD and XRF analysis were used to compliment

270 and support the mineral identification along with the rover like instruments. These analyses were

271 used to complement and support the stated hypothesis.

272 **1.1.   Mars habitability and carbonates**

273   No compelling evidence of life has yet been identified on Mars. However, the planet's

274 fluvial valleys, paleolake deposits, and alluvial fans/deltas provide geomorphological evidence of

275 a past hydrologic cycle (e.g., Cabrol and Grin, 1999; Irwin et al., 2002; Malin and Edgett, 2003;

276 Moore and Howard, 2005; Fassett and Head, 2008, 2011; Fairen et al., 2010; Grant et al., 2008,

277 2014; Metz et al., 2009; Grotzinger et al., 2015; Goudge et al., 2015). The presence of water on

278 early Mars (4.1 – 2.9 billion years ago) indicates the potential for a habitable more Earth-like

279 environment with preservation potential for past or present life (Fairén et al., 2010; Westall et al.,

280 2013; Westall et al., 2015, McMahon et al., 2018). The detection of hydrated minerals on Mars

281 can strengthen our understanding of surface geology and determine the presence of past

282   habitable environments (Ehlmann and Edwards, 2014). The potential of past or present life on

283   Mars is closely related to the extent of water on early Mars, though it remains unresolved

284   (Westall et al., 2013; 2015; McMahon et al., 2018).

285   Carbonates have been identified in several different localities on the Martian surface from

286   Earth-based observations, orbiters, and rovers. The Compact Reconnaissance Imaging

287   Spectrometer for Mars (CRISM) on the Mars Reconnaissance Orbiter (MRO) (e.g., Ehlmann et

288   al., 2008b; Ehlmann et al., 2009; Ehlmann et al., 2010; Carter and Poulet 2012; Bramble et al.,

289   2017; Goudge et al., 2017), CRISM identified Mg-carbonates based on absorption bands in the

290   2.3, 2.5, and 4 µm regions (Ehlmann et al., 2008b). The Planetary Fourier Spectrometer aboard

291   the Mars Express Orbiter identified that the wavelength position of a 3.9 µm region absorption

292   feature in the spectra of across selected regions on Mars best corresponded to Mg-carbonates.

293   (Palomba et al., 2009), the Mössbauer spectrometer onboard the Mars Exploration Rover Spirit

294   (MER) detected magnesium rich-carbonates (magnesite; $MgCO_3$) interpreted to be a product of

295   hydrothermal alteration (Morris et al., 2010) or evaporite precipitates (Ruff et al., 2014). The

296   carbonates identified by MER have also been detected by the CRISM orbiter, confirming their

297   presence through *in situ* detection (Ehlmann et al., 2009; Carter and Poulet 2012). Telescopic

298   Earth-based and Earth-orbiting observations (Blaney and McCord, 1989; Pollack et al., 1990;

299   Lellouch et al., 2000) such as the short wavelength spectrometer of the Infrared Space

300   Observatory detected absorption bands within the 2.4-45 µm wavelength region (Lellouch et al.,

301   2000). The University of Hawaii 2.2-m telescope at the Mauna Kea Observatory, Hawaii

302   detected an absorption feature band in the 3.8 to 3.9 µm spectral region (Blaney and McCord,

303   1989); both detections were ascribed to carbonates.

304   The detection of carbonates in many areas on Mars implies and supports an extensive

305   aqueous history (Morris et al., 2010) and a more conducive environment for life during the

306   Noachian to early Hesperian (4.1 – 2.9 billion years ago) than that of the present-day Martian

307   surface (Fasset and Head., 2011). Despite these detections, there is a perceived shortfall in

308   carbonate abundances on the surface of Mars compared to Earth (Catling, 1999). Carbonates are

309   normally the first precipitate in an evaporitic sequence due to their very low solubility (Catling,

310   1999). Therefore, more soluble salts such as sulfates and halides could have crystallized above

311   the carbonates, hiding them from detection (Catling, 1999). The discovery and identification of

312 specific carbonates on Mars can aid in the reconstruction of paleoenvironments and trace the

313 evolution of the atmosphere (Palomba et al., 2009), in addition, to helping clarify the debate

314 about the early Martian environment and atmosphere.

315   The most recent detection of carbonates on Mars is within and proximate to Jezero crater.

316 Jezero crater is an impact crater located in the Nili Fossae region on Mars of Noachian age

317 (Mandon et al., 2022) with a diameter of ~45 km (Goudge et al., 2015) and a fluvial system of

318 ~3.9 Ga in age (Fassett and Head, 2008a). Jezero crater lies at the edge of the Isidis basin, an

319 ~1900 km diameter impact crater (Schultz and Frey,1990) that formed in the middle to early

320 Noachian (~3.95-3.97 Ga) (Werner, 2008; Fassett and Head, 2011). The crater lake contained a

321 standing water body with two inlet valleys and an outlet valley (Fassett and Head, 2005, 2008),

322 forming a western fan deposit within ~20-40 years (Schon et al., 2012).

323   The landing site of the Perseverance rover within Jezero crater provides a unique

324 opportunity to investigate carbonates of a possible fluvio-lacustrine origin in detail (Horgan et

325 al., 2020). Jezero crater is also of high value for microbialites preservation and detection because

326 of its unique complex fluvio-lacustrine paleoenvironment (Horgan et al., 2020) that shares

327 characteristics with many microbialite-hosting carbonate deposits on Earth. There is potential for

328 the rover to identify biosignatures within carbonates from macroscale biosignatures such as

329 microbialites being dominantly composed of carbonates (Riding, 2011), as well as the ability of

330 carbonates to form and preserve microbially-influenced macroscale to microscale formations and

331 fabrics (Grotzinger and Knoll 1995, 1999; Riding 2011; Dupraz et al., 2011).

332   On Earth, many carbonate deposits and processes have been documented, including

333 microbially-induced calcification which can be traced back to 2.6 Ga in the Earth's geological

334 record (Altermann et al., 2006). Carbonates can preserve and entomb microfossils by enclosing

335 or replacing the microbial cellular structures with carbonate mineralogy (Westall and Cavalazzi,

336 2011; Shapiro and Konhauser, 2015; Wang et al., 2015; McMahon et al., 2018) and calcifying

337 microbial filaments within microbialites and carbonate deposits (Burne and Moore, 1987;

338 Riding, 2011; McMahon et al., 2018). On Earth, well-preserved fossil microbes have been found

339 in laminated and nodular phosphates and carbonates (McMahon et al., 2018). Additionally,

340 ancient Archean carbonate deposits are known to have preserved evidence of microorganisms

341 (Walter 1983; Kazmierczak and Altermann 2002; Altermann and Kazmierczak 2003;

342 Kazmierczak et al. 2004, 2009; Altermann et al. 2006). The biogenic origin for some of the

343 oldest microbialite fossils on Earth are still debated, as microfossils or biosignatures are not

344 unambiguously associated with them (Buick et al., 1981; Grotzinger and Knoll 1999; Lepot et

345 al., 2008, 2009).

346   The rocks underlying the Martian regolith are largely ultramafic, some of which date back

347 to the Noachian (McGetchin and Smith 1978; Treiman 1986; Pinet and Chevrel; Burns and

348 Fisher 1990; Mustard and Sunshine 1995). It is possible that alkaline lakes and waters were

349 present on Mars during the weathering of these mafic/ultramafic terrains (Russell and Hall

350 1999). The proposed process of CO_2 metabolism on Mars would have had the potential for

351 stromatolite-like mounds to form (Russell et al., 1999). Given the association of carbonates with

352 ultramafic and mafic rocks on Earth and on Mars, this study investigated the relationships

353 between carbonate composition and the detectability for a number of terrestrial occurrences of

354 microbialites.

355 **1.2.   Jezero crater bedrock**

356   The NE Syrtis region adjacent to Jezero crater, contains both igneous and aqueously-

357 altered lithologies (Bramble et al., 2017). The Isidis basin, also in proximity to Jezero crater,

358 includes an Olivine-rich unit (Goudge et al., 2015); it may contain up to ~40% olivine (Poulet et

359 al., 2009). Several interpretations of formation are proposed for the Olivine-rich unit identified

360 within Jezero crater, including via the exposure of an olivine-rich subsurface intrusion (Hoefen et

361 al., 2003), an olivine-rich basaltic flow (Hamilton and Christensen, 2005), olivine-rich ash

362 (Kremer et al., 2019) or the emplacement of an olivine-rich impact sheet (Mustard et al., 2007,

363 2009). Of particular relevance to the current study, the geology within and adjacent to Jezero

364 crater includes a variety of mafic/ultramafic lithologies, as well as carbonate-, serpentine-, and

365 olivine-bearing units (Goudge et al., 2015; Ehlmann et al., 2008b).

366   In Jezero crater, the mafic/ultramafic units explored in most detail to date include the

367 Séítah and Máaz formations. In-situ hydration features have been detected by SuperCam

368 reflectance spectra in both Séítah and Máaz formation rocks with a prominent 1.9 µm absorption

369 pointing to similar hydration states (Wiens et al., 2022; Mandon et al., 2022). Minerals that may

370 cause the 1.9 µm absorption include oxyhydroxides, phyllosilicates, sulfates, and hydrated

371 carbonates (Mandon et al., 2022).

372   In Jezero Crater, the mafic/ultramafic units explored in most detail to date include the

373   Séítah and Máaz formations. In addition to the Séítah and Máaz formations, several other units

374   within Jezero Crater contain mafic and ultramafic minerals (Bramble et al., 2017; Mustard et al.,

375   2009). In situ analysis by the Perseverance rover has confirmed that the Jezero Crater floor is

376   consistent with igneous mineralogy, where altered basaltic rocks are found on top of the olivine-

377   rich rocks (Wiens et al., 2022; Farley et al., 2022; Liu et al., 2022; Beyssac et al., 2022; Udry et

378   al., 2022). Both the Séítah and Máaz units have signatures of their interaction with water, which

379   produced various alteration products (Farley et al., 2022). In-situ hydration features have been

380   detected by SuperCam reflectance spectra in both formation rocks with a prominent 1.9 µm

381   absorption pointing to similar hydration states (Wiens et al., 2022; Mandon et al., 2022). The

382   minerals that may cause the 1.9 µm absorption include oxyhydroxides, phyllosilicates, sulfates,

383   and hydrated carbonates (Mandon et al., 2022).

384   The Séítah unit rocks are Mg-rich, and consist of 2-3 mm olivine crystals as well as

385   pyroxenes (Farley et al., 2022; Wiens et al., 2022). The individual mineral grains are often

386   rimmed with Mg-rich carbonates, which are proposed to be produced by the interaction of CO_2-

387   rich water (Farley et al., 2022). Bosak et al. (2022) determined that the Mg-Fe-rich carbonates

388   present along the grain boundaries indicate a reaction with CO_2-rich water with water-poor

389   conditions within the Séítah formation. Séítah rocks also contain phyllosilicates, carbonates, and

390   oxyhydroxides (Mandon et al., 2022). The Séítah unit is classified as having ~41% olivine, and

391   ~15% plagioclase, which is strongly mafic but not strictly ultramafic (i.e., <10 wt.% plagioclase)

392   (Wiens et al., 2022). Fe-Mg carbonates might be present within the Séítah formation in low

393   proportions (Wiens et al., 2022; Clave et al., 2022). VISIR (Visible and Infrared) spectra of

394   Séítah rocks acquired by the Perseverance Rover's SuperCam instrument exhibit a 2.31 µm

395   absorption feature which could be attributed to a complex mixture of Mg-rich phyllosilicates

396   and/or Fe-Mg carbonates (Wiens et al., 2022). Carbonates comprise a small (<5 % fraction) of

397   the minerals in these rocks based on their detection in LIBS (Laser Induced Breakdown

398   Spectroscopy), VISIR, and Raman observations (Wiens et al., 2022). Due to the predominance of

399   igneous minerals, the degree of aqueous alteration was not extensive (Scheller et al., 2022). The

400   lack of alteration minerals such as serpentines suggests a time-limited interaction, low water rock

401   ratios, or ambient fluid temperatures during carbonation (Scheller et al., 2022).

402   The Crater Floor Fractured Rough (Cf-fr) unit, informally called the Máaz formation

403   (Wiens et al., 2022; Farley et al., 2022), is also likely igneous in origin (Udry et al., 2022).

404   Perseverance rover observational data indicate a mafic composition made up of 0.5–5 mm size

405   pyroxene crystals, plagioclase feldspar, Fe-oxides, and apatite (Wiens et al., 2022; Farley et al.,

406   2022; 2022, Udry et al., 2022). The Máaz formation is generally believed to have been formed

407   through a single volcanic process (lava flows) depositing a basaltic to basaltic-andesitic lava and

408   not through fluvial-lacustrine or sedimentary processes (Wiens et al., 2022; Mondon et al.,

409   2022).

410   **1.3.   Carbonates in and around Jezero crater**

411   Carbonates are distributed between three separate geomorphic units in the NE Syrtis region

412   (Basement unit, Fractured unit, Feature-Bearing slope unit) capped by the Syrtis Major lava

413   flows (Bramble et al., 2017; Ehlmann and Mustard 2012). The aqueous history of the region

414   extends from the late Noachian into the Hesperian and spans at least 250 Mya (Bramble et al.,

415   2017).

416   CRISM data have been used to identify a regional rock layer consistent with the presence

417   of Mg-rich carbonates in the Nili Fossae region (Ehlmann et a., 2008a, 2008b; Carter and Poulet

418   2012; Tarnas et al., 2021). The detected Mg-rich carbonates are closely associated with

419   phyllosilicate-bearing and olivine-rich rock units which are thought to have formed during the

420   Noachian and early Hesperian in this region (Ehlmann et al., 2008a), including the area in and

421   around Jezero crater (Goudge et al., 2015; Horgan et al., 2020; Tarnas et al., 2021).

422   Proposed mechanisms of carbonate formation within Jezero crater and the greater Nili

423   Fossae region includes hydrothermal alteration (Alfredson et al., 2013; Falk & Kelemen, 2015),

424   carbonate rind formation (Jull et al., 1988), and evaporation/precipitation (Ruff et al., 2014).

425   Several studies have hypothesized these formation conditions for carbonates found in Jezero

426   crater's geologic units.

427   The ultramafic host rocks detected by orbiters within the Fractured unit gave rise to several

428   hypotheses of Mg-carbonate formation, such as hydrothermal alteration at slightly elevated

429   temperatures, contact metamorphism, precipitation from shallow lakes, and the weathering of

430   olivine-rich rocks (Ehlmann et al., 2008b; Murchie et al., 2009, Mustard et al., 2009; brown et

431   al., 2010; Ehlmann and Mustard 2012; Viviano et al., 2013, Edwards and Elhmann 2015).

432   Goudge et al., (2015) used CRISM data to detect carbonates within several geological units

433   on Mars, including the Mottled Terrain unit, Lght-toned Floor unit, and delta deposits using the

434   paired absorption features at 2.30 and 2.51 µm. They also stated that the presence of both

435   carbonates and Fe/Mg smectites suggests moderate to neutral pH, creating a habitable

436   environment during at least the period of the two fan deposits, ceasing by 3.8 Ga (Fassett and

437   Head 2008). The Light-toned Floor unit in select dune-free locations have paired absorption

438   features near 2.30 and 2.51 µm (Goudge et al., 2015) which are consistent with the Mg-carbonate

439   magnesite (Hunt and Salisbury, 1971; Gaffey, 1987). The carbonates in the Light-toned floor

440   unit could have been emplaced prior to the lacustrine activity, alternatively the carbonates could

441   have been deposited during the lacustrine period and consist of either detrital carbonates

442   sediments or carbonates precipitated from the paleolake (Goudge et al., 2015). While both are

443   plausible, the latter aqueous explanation for carbonate seems less likely (Goudge et al., 2015).

444   The Mottled Floor unit interior and exterior of Jezero crater is interpreted as forming through

445   aqueous alteration of the Olivine-rich unit (Ehlmann et al., 2008b, 2009; Mustard et al., 2009).

446   The lack of clear contact between the Light-toned floor unit and the Mottled unit suggests the

447   two units are different expressions of the same unit (Goudge et al., 2015).

448   Tarnas et al., (2021) presented results consistent with the presence of Fe/Mg carbonates in

449   and outside of Jezero crater within the Regional Olivine-Bearing (ROB) unit. Fe/Mg carbonate

450   composition is a known product of the carbonation of olivine. The Regional Olivine-Bearing unit

451   drapes into Jezero crater connecting to the Margin Fractured unit (Sun and Stack, 2020). Tarnas

452   et al., (2021) described that the ROB unit would be expected to produce both Mg and Fe-bearing

453   carbonate phases. They estimated the chemistry based on the wavelength position of the

454   absorption feature minima, as natural carbonates can form solid solutions between Mg, Fe, and

455   Ca endmembers, causing shifts in band minima positions. They deemed the carbonates within

456   and outside Jezero crater to be Mg-rich to Fe-Mg-rich (Tarnas et al., 2021) with a possible

457   formation of the non-deltaic (western and northern sedimentary fan deposits) carbonates

458   hypothesized to be through the hydrothermal alteration of olivine (Tarnas et al., 2021). There

459   exists the possibility that the 1.9 µm H_2O band seen in the CRISM data is associated with these

460   Mg-carbonates (Calvin et al., 1994).

461   Viviano-Beck et al., (2013) proposed that the widespread carbonates observed in the region

462   could result from serpentinization and carbonation processes acting on ultramafic rocks, from

463   which talc and magnesite would have formed along with serpentinized olivine. The

464   serpentinization and carbonation processes have not undergone full completion, as both olivine

465   and serpentine are observed throughout the Nilli Fossae region (Viviano-Beck et al., 2013).

466   Brown et al. (2010) hypothesized the presence of talc as the Fe/Mg smectite, where the talc

467   spectral properties are hidden by the presence of carbonate, given the presence of the olivine-rich

468   protolith in association with Mg-carbonates. This led to a hypothesis of a single hydrothermal

469   event forming both the carbonate-bearing unit and the phyllosilicate talc (Brown et al., 2010).

470   From the CRISM data, the carbonates within Jezero crater are spectrally variable. They all

471   exhibit bands near ~2.31 µm and ~2.51 µm, hydration bands near ~1.93 µm, and with one or

472   more mafic (Fe^{2+}) components causing absorption features at ~1.0 µm and ~1.8 µm, a red

473   spectral slope, and a ~1.3 µm band or shoulder (Goudge et al., 2015; Horgan et al., 2020). A

474   possible interpretation of the 1.3 µm band or shoulder included Fe^{2+} within the carbonates, as

475   Mg-Fe carbonates form a solid solution series (Dubrawski et al., 1989; Boulard et al., 2012).

476   Within Jezero crater, several units contain evidence of Mg-carbonates: the western and

477   northern sedimentary fan deposits, the "Marginal Carbonates", the Light-toned Floor unit (Cf-fr,

478   Cf-f-1), and the Mottled Floor unit (Goudge et al., 2015; Horgan et al., 2020; Tarnas et al., 2021;

479   Ehlmann et al., 2008b, 2009; Mustard et al., 2009). The Mg-rich carbonates in these deposits are

480   suggested to be poorly lithified and naturally friable (Goudge et al., 2015). The Mg-carbonates

481   within Jezero crater have been suggested to originate from a lacustrine environment (Horgan et

482   al., 2020), formed due to the aqueous hydrothermal alteration or serpentinization in the

483   subsurface, or ambient temperature surface alteration of the Olivine-rich Basaltic unit that

484   comprises the underlying topography (Ehlmann et al., 2008b, 2009; Mustard et al., 2009; Tarnas

485   et al., 2021), and supported by the analysis of the crater watershed (Goudge et al., 2015).

486   The carbonates from the geological unit outlined as the "Marginal Carbonates" suggest

487   their origin to be lacustrine from detailed investigation of the mineralogy and morphological

488   properties (Horgan et al., 2020). The Marginal Carbonates unit has stronger and clearer

489   carbonate signatures, appearing at the base of the crater wall in a narrow strip, and representing

490   the strongest carbonate signatures at Jezero crater (Horgan et al., 2020). These signatures may

491   represent authigenic nearshore carbonates in Jezero crater's lake (Horgan et al., 2020). The

492   modeling of carbonates within Jezero crater conducted by Zastrow and Glotch (2021) supports

493   the hypothesis of lake-side precipitation laid out by Horgan et al., (2020) within the Marginal

494   Carbonates. Similarly, both agree that there are differences between the carbonates formed in the

495   mottled terrain and the Marginal Carbonates, likely from differences in formation processes and

496   environment in addition to heavier serpentinization and carbonation occurring. A comparison to

497   lacustrine environments on Earth suggests that the carbonate unit identified from orbit has the

498   potential to preserve macro- and micro-scale biosignatures represented by microbialite

499   formations (Horgan et al., 2020). Within the Marginal Carbonates unit in Jezero crater, the

500   strength of the 1.9 μm hydration band varies significantly (Horgan et al., 2020). Some of the

501   carbonate spectra do not exhibit a 1.9 μm band, some exhibit a strong 1.9 μm band, in addition to

502   some exhibiting a rounded 2.0 μm band, consistent with a hydrated Mg-carbonate or a

503   magnesite-hydromagnesite mixture (Horgan et al., 2020). Zastro and Glotch (2021) concluded

504   the presence of magnesite and siderite within the Marginal Carbonate unit.

505   The NASA Mars 2020 Perseverance rover has several instruments with the capabilities to

506   identify Mg-carbonates and any associated potential biosignatures. These include, the SuperCam

507   instrument, which could detect and characterize carbonates based on reflectance, Raman and

508   elemental analytical capabilities (Wiens et al., 2016, 2021), the Scanning Habitable

509   Environments with Raman & Luminescence for Organics & Chemicals (SHERLOC) (Beegle et

510   al., 2015), and the Planetary Instrument for X-ray Lithochemistry (PIXL) (Wade *et al.,* 2016;

511   Allwood *et al.,* 2020). The possible detection of hydrous magnesite in the Marginal Carbonates

512   and possible association with biosignatures consistent with formation in lacustrine environments

513   (Horgan et al., 2020) makes the Marginal Carbonates and Jezero crater ideal for targeting and

514   sampling.

515   **1.4.   Carbonates: Presence and stability on Mars**

516   To better assess the presence of Mg-carbonates on Mars and their survivability, previous

517   research in the C-TAPE lab has examined the stability of hydromagnesite under current Mars-

518   like surface conditions, as well as stability to low temperature (>300 °C) heating (Cloutis et al.,

519   2008; Turenne et al., 2021). Hydromagnesite was deemed stable and spectrally detectable after

520   exposure to Mars-like surface conditions for a few weeks, with no significant loss of absorption

521 bands or features (Cloutis et al., 2008). However, impact-induced heating of hydromagnesite

522 shows that it would not survive somewhere between 180°C and 300°C heating; such heating

523 leads to a nearly featureless reflectance spectrum with no characteristic absorption features

524 (Turenne et al., 2021). Previous studies have shown that hydromagnesite undergoes a series of

525 transformations (dehydration, dihydroxylation, and decarbonization) over the 135–474°C range

526 (Vagvolgyi et al., 2008) and its decomposition is sensitive to multiple experimental factors such

527 as temperature, pressure, and UV exposure (Hollingbery and Hull, 2010).

528   A set of studies by Stromberg et al. 2014 was conducted to determine the spectroscopic

529 stability of biological pigments as microbial life is commonly associated with carbonate

530 precipitation (Jarwar et al., 2022; Gomez et al., 2018; Zhu and Dittrich, 2016).

531 Chlorophyll/carotenoids and other carbonaceous compounds can be strongly indicative of

532 biogenicity (Stromberg *et al.,* 2019; Berg *et al.,* 2014). Laboratory experiments of the stability

533 and spectral detectability of chlorophyll/carotenoids under Mars surface conditions performed by

534 Stromberg et al. (2014) suggest that they may have some resistance to degradation under Mars-

535 like surface conditions. Microbial-driven carbonate precipitation experiments also suggest that

536 different carbonate polymorphs can form by different microbes (Ronholm et al., 2014) and bio-

537 organic spectral properties can persist (Berg et al., 2014).

538 **1.5.   Mg-carbonate formation environments on Earth**

539   Carbonates are expected weathering products in a basalt- and the water-rich environment

540 with the presence of CO_2 (Catling 1999; Gooding et al., 1978). Mg-carbonates can form in a

541 variety of geological environments. The formation of Mg-carbonates commonly occurs during

542 the evaporation of Mg-rich waters with relatively high ratios of Mg:Ca (Müller et al., 1972). Mg-

543 carbonates such as magnesite and hydromagnesite typically form in mafic and ultramafic terrains

544 that host environments such as alkaline lakes (Shirokova et al., 2013; Müller et al., 1972; Walter

545 et al., 1973; Braithwaite and Zedef, 1994), in playas (Vance et al., 1992; Renaut, 1993; Power et

546 al., 2014), by the weathering of serpentine-rich outcrops and mine tailings (Wilson et al., 2009,

547 2011; Bea et al., 2012), and in cave systems as speleothems (Oskierski et al., 2019; Beinlich &

548 Austrheim, 2012; Fishbeck and Müller, 1971; Canaveras et al., 1999). Magnesite is known to

549 occur in association with alteration products such as serpentinite (Wilson et al., 2006), in

550 addition to precipitating as microbial mats or microbialites (Grotzinger and Knoll 1995).

551 Hydromagnesite is a magnesium hydroxyl carbonate (e.g., Königsberger et al. 1999; Russell et

552 al. 1999; Edwards et al. 2005) that can also form in a variety of environments. Locations such as

553 Atlin in northwestern British Columbia, Canada (Power et al., 2009; Power et al., 2014), Lake

554 Alchihica in Pueblo State, Mexico (Armienta et al., 2008; Kaźmierczak et al., 2011), and Lake

555 Salda in southwestern Turkey (Braithwaite and Zedef, 1994, 1996; Russell et al., 1999) have

556 microbialites forming through biologically-mediated hydromagnesite precipitation.

2. Study Sites

558 We included four analogue sites in this study, including the Atlin playas, Clinton Creek,

559 Lake Salda, and Lake Alchichica, all of which have some relevance to Jezero crater. The sites

560 exhibit similarities in terms of being low-temperature, alkaline environments, with Mg-carbonate

561 formation occurring through precipitation, evaporative or subaerial processes in a closed or open

562 basin system with mafic or ultramafic precursor bedrock environments. Most importantly, they

563 all have authigenic carbonate formations in lacustrine settings. Site characteristics are provided

564 in **Table 1**.

2.1. Atlin playas, British Columbia, Canada

566 The town of Atlin is located in northwestern British Columbia, Canada (59°35′ N, 133°42′

567 W) at an elevation of 674 m, with a dry sub-arctic climate (Power et al., 2009). Temperatures

568 range between -15.4°C to 13.1°C, with an average of 0.5°C, and average precipitation of 348

569 mm/yr (Power et al., 2009). Near Atlin, hydromagnesite-magnesite playas are located in

570 ultramafic bedrock in topographic lows (Power et al., 2007, 2009). The pH documented around

571 the playa wetlands range from 8.0–8.6 (Power et al., 2009) (**Figure 1**). Power et al. (2014)

572 identified three sedimentary units composing the playa region, which includes siliciclastic mud,

573 Ca-Mg carbonate sediments deposited subaqueously, and Mg-carbonate sediments deposited

574 subaerially. The chemistry of the source water influences the deposition of such units (Power et

575 al., 2014). Fresh surface water from the last deglaciation will deposit siliciclastic sediments.

576 When the freshwater ceases, the alkaline Mg–HCO_3 groundwater being generated from the

577 weathering of ultramafic bedrock will primarily precipitate carbonates (Power et al., 2014).

578 The precipitation and evaporation processes forming carbonates in this region is

579 microbially-driven or -influenced by several biological processes operating, including

580 alkalization by cyanobacteria, sulfate reduction by sulfate-reducing bacteria, and silica removal

581   by diatoms (Power et al., 2007). The hydromagnesite-rich sediments precipitate and form

582   microbial mats influenced by benthic microbial communities (Power et al., 2009). The carbonate

583   mats are ~2 cm thick, non-lithified, and non-laminated, and have internal fabrics that resemble

584   clots with no evident sedimentary structures (Power et al., 2007). Beneath the hydromagnesite

585   microbial mats, anoxic black sediments consisting of aragonite and iron sulfides are present

586   (Power et al., 2009). Precipitation of aragonite also occurs within the playas due to CO_2

587   degassing of supersaturated groundwater that is being discharged into the wetland (Power et al.,

588   2009).

589   There are no inflow or outflow channels to the wetland, thus it is considered to be fed

590   primarily by groundwater (Power et al., 2009). The weathering of the bedrock, consisting of

591   serpentinized, carbonatized, and deformed harzburgite with minor dunite and pyroxenite veins

592   (Hansen et al., 2005), produces magnesium-rich groundwater that discharges into the playas

593   (Power et al., 2007). Most of the waters in the Atlin area are super-saturated in calcite, aragonite,

594   and magnesite, and the wetlands are supersaturated with hydromagnesite with an Mg/Ca ratio of

595   50:1 (Power et al., 2009). The concentrations of carbonates within this drainage basin are a result

596   of its closed nature (Power et al., 2009). For additional information on the Atlin Lake, study area

597   see Power et al. (2007, 2009). The Atlin samples included in this study are shown in **Figures 2**

598   **and 3** and described in **Tables 1 and 2**.
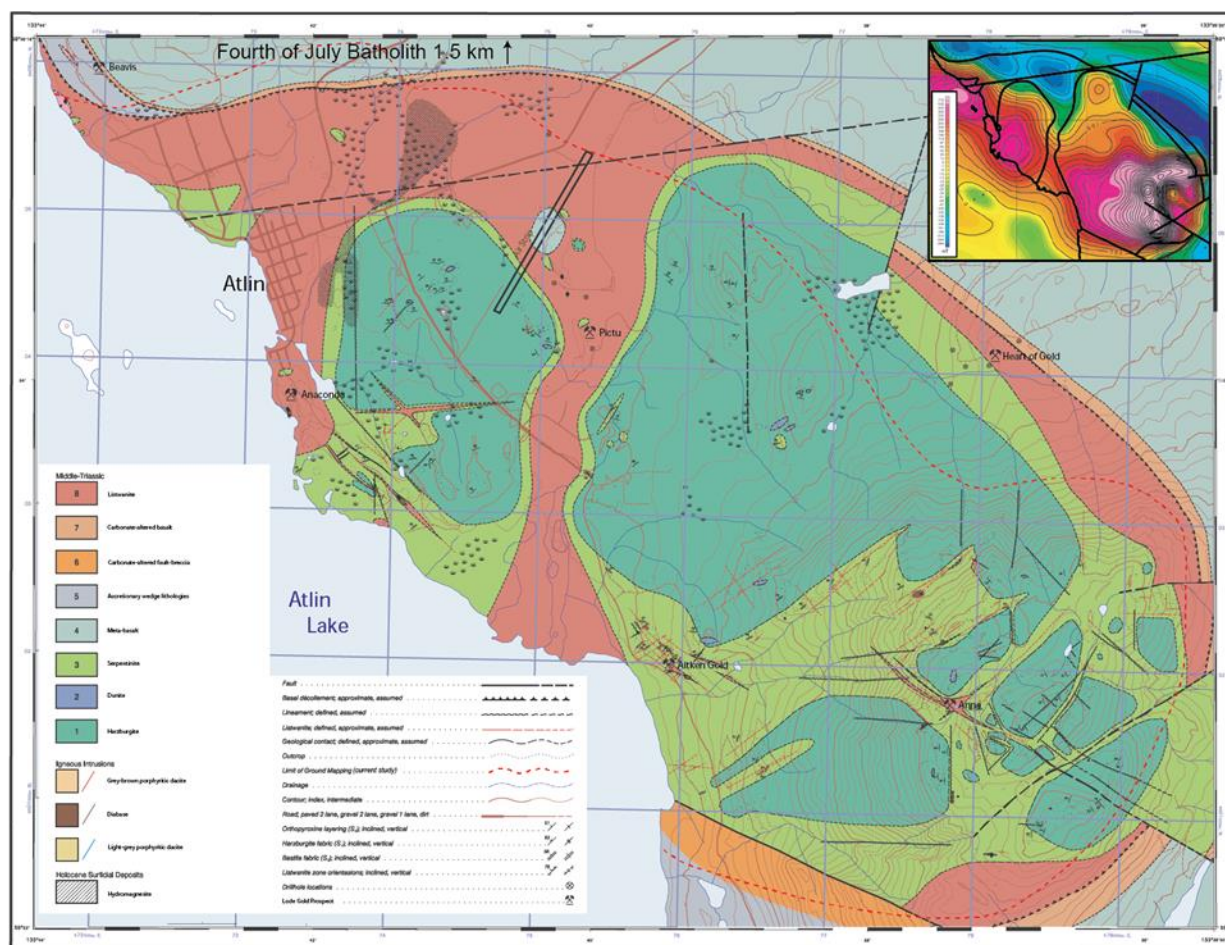
Figure 1. Location of the town of Atlin with respect to several mine sites including Pictu and Anna mines from which 16-AT-PI-1, 16-AT-PI-2, and 16-AT-Anna samples were harvested. The map was taken from Hansen et al. (2005).
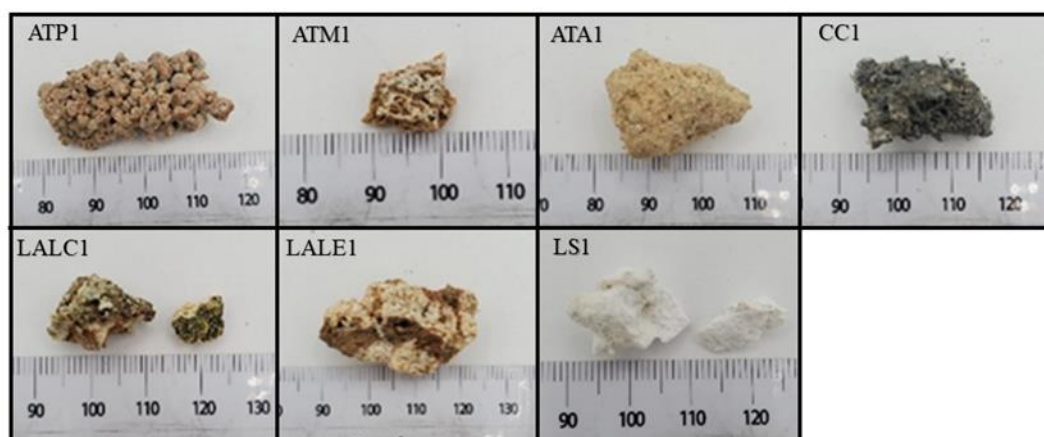
Figure 2. Whole rock sample images of the Atlin Lake (ATP1, ATM1, ATA1), Clinton Creek (CC1), Lake Alchichica (LAL-C1, LAL-E1), Lake Salda (LS1) samples used for analysis.
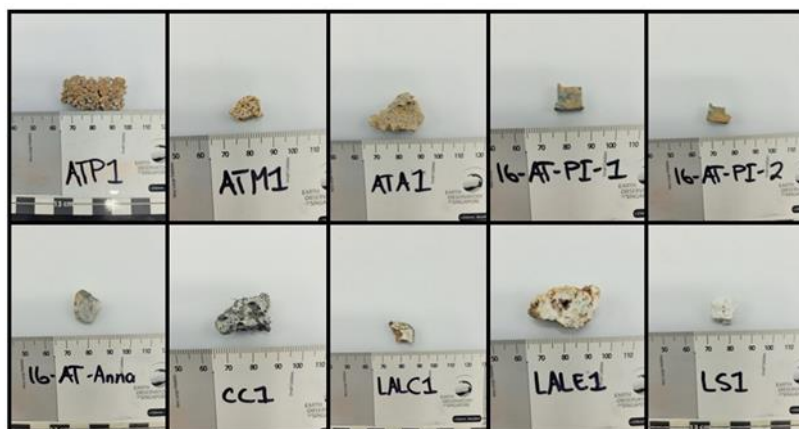
Figure 3. Polished samples images from Atlin Lake (ATP1, ATM1, ATA1, 16-AT-PI-1, 16-AT-PI-2, 16-AT-Anna), Clinton Creek (CC1), Lake Alchichica (LAL-C1, LAL0E1), Lake Salda (LS1) samples used for analysis.

2.2.   Pictou and Anna mines

The Pictou and Anna mines are very small diggings where prospecting was done in the past in the Atlin region (**Figure 1**). The mines should be related to regions where rocks have been collected from regions of exposed bedrock in this study. Magnesite samples were collected in 2016 from fuchsite-bearing (Cr-muscovite) quartz-carbonate altered harzburgite (listvenite) at the abandoned Pictou and Anna mine sites, in the Atlin ophiolite. The Atlin ophiolite is described as a tectonically emplaced mantle section of the dominantly harzburgitic and minor dunitic composition, situated within the regional Stikine and Cache Creek terranes (Ash, 1994; Hansen et al., 2005). The formation of the listvenite around Atlin postdates the ophiolite obduction with a date ranging between 168–172 Ma (Ash, 2001). Listvenite formation and magnesite precipitation are interpreted as the result of a hydrothermal fluid-driven alteration of the harzburgite precursor. Quartz fluid inclusion micro thermometry of quartz-carbonate veins has constrained the alteration conditions to 210–280 ˚C (see Andrew, 1985), consistent with the gconditions of similarly altered ultramafic rock elsewhere (e.g., Beinlich et al., 2012, 2020).

The Pictou mine site (sample ID: 16AT-PI-1/2) is located in a topographic depression between Monarch Mountain and the runway of Atlin airfield (59°34'11.46"N; 133°39'58.77" W). The outcropping listvenite is part of an N-S trending 500 m wide band of intense harzburgite alteration atop the basal thrust of the ophiolite. Both samples from Pictou are part of a transect across the hydrothermal alteration front between listvenite and completely serpentinized harzburgite. Sample 16AT-PI-1 is located approximately 6 m from the contact and 16AT-PI-2 is

629   located ~5 m from the contact. The Anna mine site (Sample ID: 16AT-ANNA) is located ~100

630   m to the west of the barren top of Monarch Mountain (59°32'48.31"N; 133°37'24.83" W) and

631   represents a 2 m wide and 1 m deep pit in listvenite. Listvenite alteration at this location is

632   restricted to the immediate vicinity of a NW trending fault intersecting partly serpentinized

633   harzburgite. Macroscopically, the listvenite appears strongly silicified, resembling chert, and

634   contains less magnesite and fuchsite than the samples from the Pictou site.

635   Listvenites are common in ultramafic bodies, with examples from Timmins Ontario,

636   Canada (e.g., Schandl & Naldrett 1992) and the Mother Lode camp in California, USA (e.g.,

637   Wittkopp 1983) Listvenites are produced through several reactions starting with the protolith

638   rock of serpentine + olivine + brucite. These react with CO_2 to form serpentine and magnesite,

639   then continue to decompose to produce magnesite and talc, and finally magnesite and quartz

640   (Hansen et al., 2005). The listvenite samples have reacted to completion and consist of quartz

641   and magnesite together with minor fuchsite and chromite but lack relicts of the precursor

642   ultramafic mineral assemblage. (Hansen et al., 2005). The samples with talc but no quartz

643   present are considered to have undergone reactions R_1 (olivine reacting to produce antigorite and

644   magnesite) (Hansen et al., 2005).

645   The following reactions are taken from Hansen et al. (2005).

646   R_{1a}: 34 Mg_2SiO_4 (Olivine) + 20 CO_2 + 31 H_2O $\Rightarrow$ $Mg_{48}Si_{34}O_{85}(OH)_{62}$ (Antigorite)+ 20

647    $MgCO_3$ (Magnesite)

648   R_{1b}: $Mg(OH)_2$ (Brucite) + CO_2 $\Rightarrow$ $MgCO_3$ (Magnesite) + H_2O

649   R_2: 45 $MgCO_3$ (Magnesite) + 17 $Mg_3Si_4O_{10}(OH)_2$ (Talc) + 45 H_2O
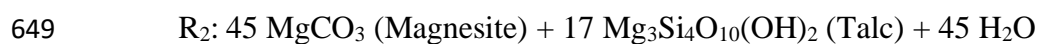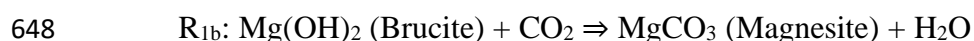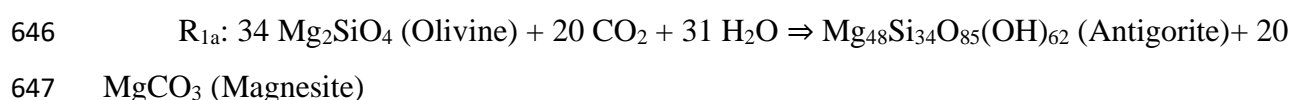
650   The Pictou and Anna mines samples included in this study are shown in **Figures 2 and 3**

651   and described in **Tables 1 and 2**.

652   **2.3.   Clinton Creek, Yukon, Canada**

653   Aragonite-dominated microbialite formations and Mg-carbonate coatings occur on various

654   rocks and boulders in the region.have been identified at the abandoned asbestos mine at Clinton

655   Creek Yukon, Canada, forming from ultramafic precursors (**Figure 4**) (Power et al., 2011). The

656   closure of the mine occurred in 1978, and the microbialites are presumed to have started forming

657   soon after (Power et al., 2011). The mine site is located 77 km northwest of Dawson City

658   (64°26'42" N, 140°43'25" W) within an asbestos deposit on the Klondike Plateau at an elevation

659   of ~380 m above sea level (Power et al., 2011). The Clinton Creek region has a subarctic climate

660   with a mean annual temperature of -4.4° C (Htoon, 1979). The Dawson City weather station

661   documented an average of 324 mm of precipitation yearly (Power et al., 2011)

662   This location can enhance our understanding of the weathering processes of ultramafic

663   material on early Earth (Power et al., 2011). The bedrock is almost entirely serpentinized to

664   chrysotile and antigorite from serpentine, harzburgite, lherzolite, dunite, and pyroxenite (Htoon,

665   1979). The water chemistry within the pit pond was determined by Power et al. (2011) to be

666   subsaline, and alkaline with a pH of 8.4 on average and supersaturated with aragonite, calcite,

667   dolomite, and magnesite (Power et al., 2011). The pond has neither inflow nor outflow and

668   varies substantially from year to year due to evaporation and low yearly precipitation (Power et

669   al., 2011).

670   The Clinton Creek columnar dark gray lithified microbialite sample were collected from the

671   Porcupine open pit in 2007 when the low water levels allowed for their discovery and collection

672   along the periphery of the pit (Power et al., 2011). The microbialites from the pit pond varied in

673   height from a few cm to 15 cm with an internal mm-scale spherulitic fabric. Previous studies

674   have identified the microbialites' mineralogy through X-ray diffraction to consist of aragonite,

675   minor clinochrysotile, magnesium-rich calcite, quartz, and possible vermiculite (Power et al.,

676   2011). The microbialites are suggested to be produced through microbe-influenced aragonite

677   precipitation, with the microbes acting as nucleation sites, eventually forming spherulites (Power

678   et al., 2011). The spherulite centers have varying morphology microbes (Power et al., 2011). The

679   low sedimentation rate, high calcification rate, and low microbial growth rate influence the

680   formation of microbialites at the site (Power et al., 2011). For additional information on the

681   Clinton Creek region and microbialites see Power et al. (2011). The Clinton Creek samples

682   included in this study are shown in **Figures 2 and 3** and described in **Tables 1 and 2**.

683
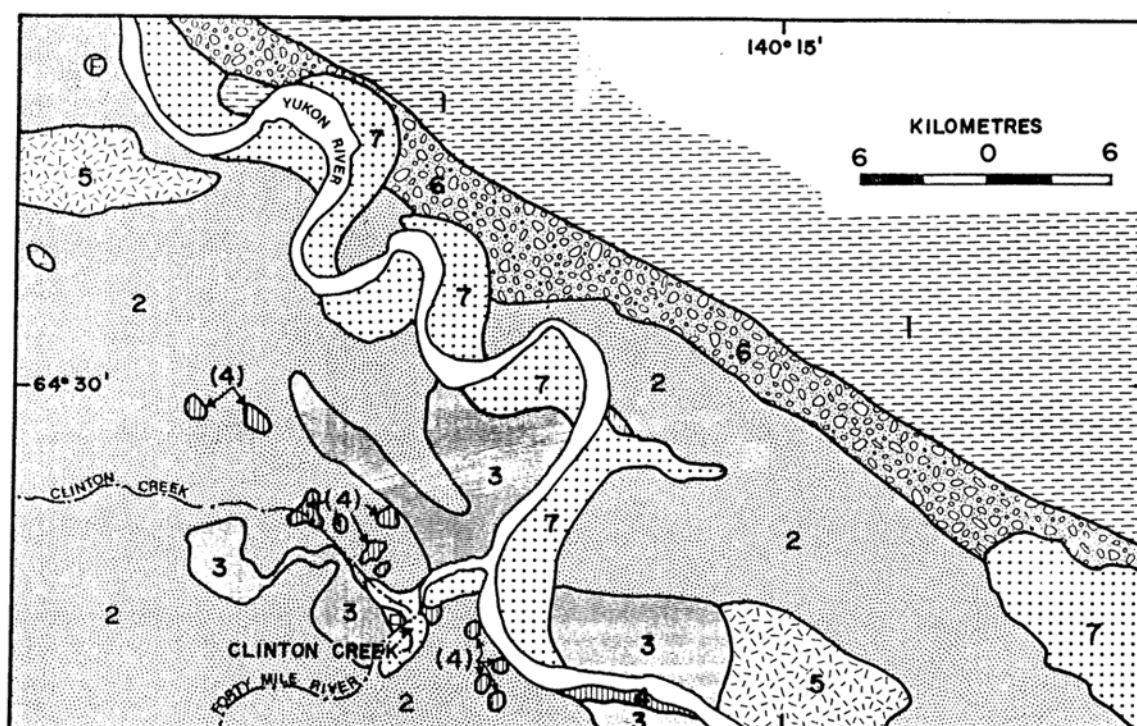
Figure 4. Clinton Creek, Yukon, Canada geology map taken from Green (1972). 1= Grit and slate; 2= Quartz-mica schist and quartzite; 3= Greenstone and quartz-muscovite-chlorite schist; 4= Serpentinized ultramafic rocks; 5= Biotite granodiorite and quartz monzonite; 6= Sandstone, shale conglomerate and lignite; 7= Alluvial deposits; F= Fossil locality.

2.4.   Lake Alchichica, Puebla State, Mexico

Lake Alchichica, Mexico (19°22′N 97°24′W) is a caldera lake that may also be a maar (low aspect crater formed by shallow explosive eruptions) with a closed drainage basin and no surface outflows, but it does get rainwater flow during the rainy season (**Figure 5**) (Armienta et al., 2008). Lake Alchichica has an average precipitation of 400 mm/yr, and an annual evaporation rate of 500–600 mm with a semi-arid climate (Armienta et al., 2008; Kaźmierczak et al., 2011), and the region has a mean annual temperature of 14.4° C (Armienta et al., 2008). It is located 2300 m above sea level (Kaźmierczak et al., 2011). The crater lake is 2 km in diameter and a maximum of 65 m in depth, filled with saline (alkaline) waters (Armienta et al., 2008; Silva-Aguilera et al., 2022). It is one of a number of endorheic lakes of the southern Trans-Mexican-Volcanic Belt (Kaźmierczak et al., 2011). The lake is supplied by both precipitation and Ca^{2+} and HCO_3- enriched groundwater due to the calcareous Cretaceous Mountain deposits (Ramirez-Garcia and Vazquez-Gutierrez 1989; Vilaclara et al. 1993; Alcocer and Hammer 1998; Caballero

702   et al. 2003). The surrounding geology is comprised of limestone and shale covered in basaltic

703   andesites, overlaid by pyroclastic and lacustrine deposits (Chako-Tchamabé et al. 2020).

704   The microbialites precipitation within Lake Alchichica are associated with diver benthic

705   filamentous and coccoidal varieties of cyanobacteria (Tavera and Komarek, 1996; Couradeau et

706   al., 2011; Kaźmierczak et al., 2011). Microbialites form on the periphery of the lake up to a

707   depth of ~14 m (Kaźmierczak et al., 2011), accreting by cyanobacterial mats. There are three

708   types of distinct morphologies of the microbialites at the site: spongy or foamy, columnar, and

709   flat crusty concentrated along the S and NE shores (Tavera and Komarek, 1996). Some

710   microbialites are present as emerged mounds above the lake water level, which are visually

711   distinct and represented by their differences in color and structure (Kaźmierczak et al., 2011).

712   Kaźmierczak et al. (2011) identified by XRD the dominance of hydromagnesite and huntite

713   within the "white" generation of microbialite and aragonite, with minor calcite dominating the

714   "brown" generation of microbialite. These generations are morphologically, mineralogically,

715   texturally, and isotopically distinct (Kaźmierczak et al., 2011). The "white" generation is older

716   than the "brown" generation, with an age of 2.8 ka BP representing the beginning of all the

717   precipitation in the lake (Kaźmierczak et al., 2011). The "brown" generation has an age of 1.1 ka

718   BP. The "white" microbialite form as large irregular mounds with surfaces that have a knobby

719   texture with no visible stratifications while the thin sections indicate microlaminated or

720   microstromatolitic textures preserved as aragonite within the diagenetic hydromagnesite

721   (Kaźmierczak et al., 2011). The "brown" microbialites are in direct contact and often grow on

722   the "white" microbialites as tightly clustered chimney-like structures with porous, spongy, and

723   non-laminated textures (Kaźmierczak et al., 2011). The "brown" microbialites microfabric

724   textures include clotted, fenestrated, laminated, (microstromatolitic), and micritic alternating

725   with spiritic layers, in addition to spherulitic and poloidal (Kaźmierczak et al., 2011). Both types

726   have distinct mineralogical differences as determined by EDS and XRD analysis (Kaźmierczak

727   et al., 2011). In all samples investigated by Kaźmierczak et al. (2011), a <1mm thick layer of Ca-

728   rich material was found; going further into the microbialite, this layer stops abruptly or

729   continuously turns into the main body which is dominated by Mg. Ca-rich carbonate is being

730   precipitated in the living cyanobacteria mat, which transitions downwards into hydromagnesite

731   replacing the diagenetic primary aragonite, but this process is poorly understood (Kaźmierczak et

732   al., 2011). The aragonite is usually microlaminated while the hydromagnesite is structureless

733 (Kaźmierczak et al., 2011). The identification of cyanobacteria remains is extremely rare in the

734 "white" microbialites (Kaźmierczak et al., 2011). The Lake Alchichica samples included in this

735 study are shown in **Figures 2 and 3** and described in **Tables 1 and 2**.
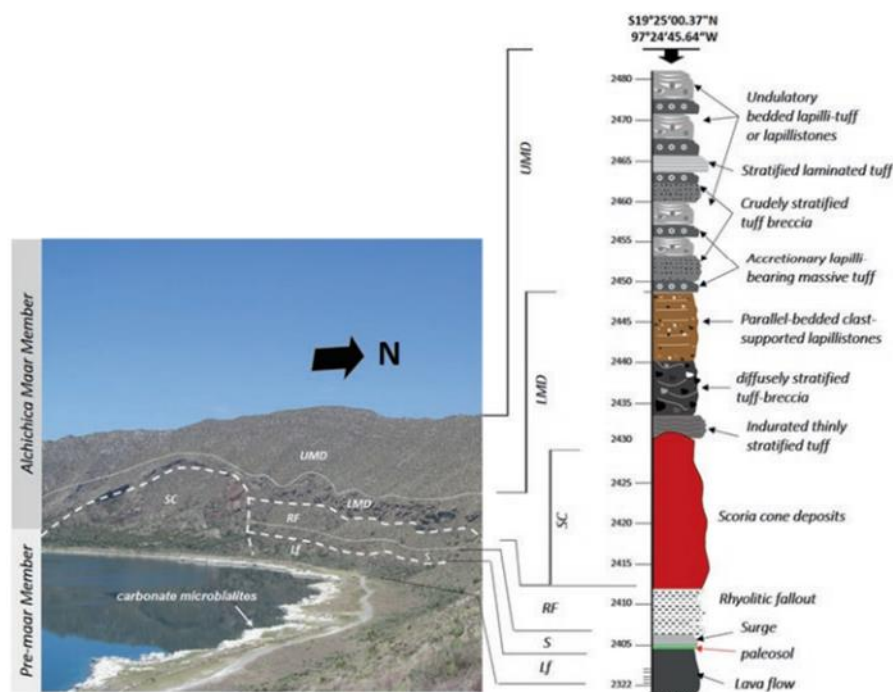
736

737 **Figure 5**. Image of the wester crater rim of Lake Alchichica and an interpretive stratigraphic column presented on
738 the right side taken from Alcocer et al. (2021).

2.5.   Lake Salda, Turkey

740 Lake Salda is a deep (~196m) alkaline (pH>9) closed-basin lake in southwestern Turkey

741 (Russell et al., 1999). The lake is located on a tectonic pit at an altitude of 1193 m above sea

742 level (Davraz et al., 2019). The average annual temperature of the area is 11.5 °C with a mean

743 precipitation of 493.086 mm; discharge of the lake occurs through evaporation, with an average

744 evaporation rate of 1725.2 mm (Davraz et al., 2019). Lake Salda has several streams recharging

745 the basin and groundwater inflow (Davraz et al., 2019). Davraz et al. (2019) assessed the water

746 quality of Lake Salda and identified the high Mg content and dominant water type being Mg-

747 CO_3-HCO_3 due to the weathering of the ultramafic bedrock.

748 Lake Salad's is surrounded by different geological formations. The Çameli Formation

749 unit is composed of sandstone, claystone, limestone, and conglomerate (Davraz et al., 2019), and

750 an alluvial unit consisting of gravel and sand, with an additional slope debris unit (Davraz et al.,

751   2019). The bedrock geology consists of serpentinized ophiolites with the dominant rock types

752   being harzburgite and serpentinized harzburgite, lizardite, and some dunite and limestone

753   (Russell et al., 1999; Davraz et al., 2019).

754   Braithwaite and Zedef, (1996) identify the lake as one of the only known deep perennial

755   lakes where Mg-carbonates such as hydromagnesite precipitate. This is due to the dissolution of

756   Mg-rich bedrock creating high Mg/Ca ratios within the lake waters (Braithwaite and Zedef,

757   1996). Zedef et al. (2000) identified the microbialites at Lake Salda to be related to the lake's

758   cool groundwater seepage, while Russell et al. (1999) indicated the probability of the

759   hydromagnesite precipitation being driven by evaporation processes. Hydromagnesite

760   stromatolites are abundant at Lake Salda present in the SW part of the Lake in the littoral zone

761   and found at a maximum water depth of 6–10 m (Braithwaite and Zedef 1996; Shirokova et al.

762   2013). Garczynski et al. (2021) identified microbialites occurring in shallow near-shore

763   environments and as subaerial islands to be spectrally dominated by hydromagnesites. Cemented

764   hydromagnesite muds and sands form 10–15 m high terraces that on occasion preserve textures

765   associated with microbialites (Braithwaite and Zedef, 1996). The deltas consist of large cobbles,

766   sands, and muds present near fluvial inputs (Garczynski et al., 2021).

767   Braithwaite and Zedef. (1994) were the first to state that the magnesite precipitation at

768   Lake Salda is a biologically-mediated process. The hydrated Mg-carbonates stromatolites from

769   Lake Salda have been documented to form solely from cyanobacteria and algal activity (Russell

770   et al., 1999). Microbial processes on microbialite formation may be due to CO_2 cycling, balanced

771   between photosynthetic and heterotrophic activity, regulating the formation of microbialites

772   (Balci et al., 2020). The photosynthesis-induced high pH and the change in the amount of

773   exopolymeric substances (EPS) processes may be involved in the formation of hydromagnesite

774   textures and the growth of stromatolite formations (Balci et al., 2020).

775   The microbialites are columnar with alternating fine and coarse mm-scale

776   hydromagnesite layers with central orifices, and are partially botryoidal (Braithwaite and Zedef,

777   1996b). The stromatolite morphologies do not survive lithification and become porous and

778   coarse-grained with no evidence of layering or laminations (Russell et al., 1999). The Lake Salda

779   samples included in this study are shown in **Figures 2 and 3** and described in **Tables 1 and 2**.
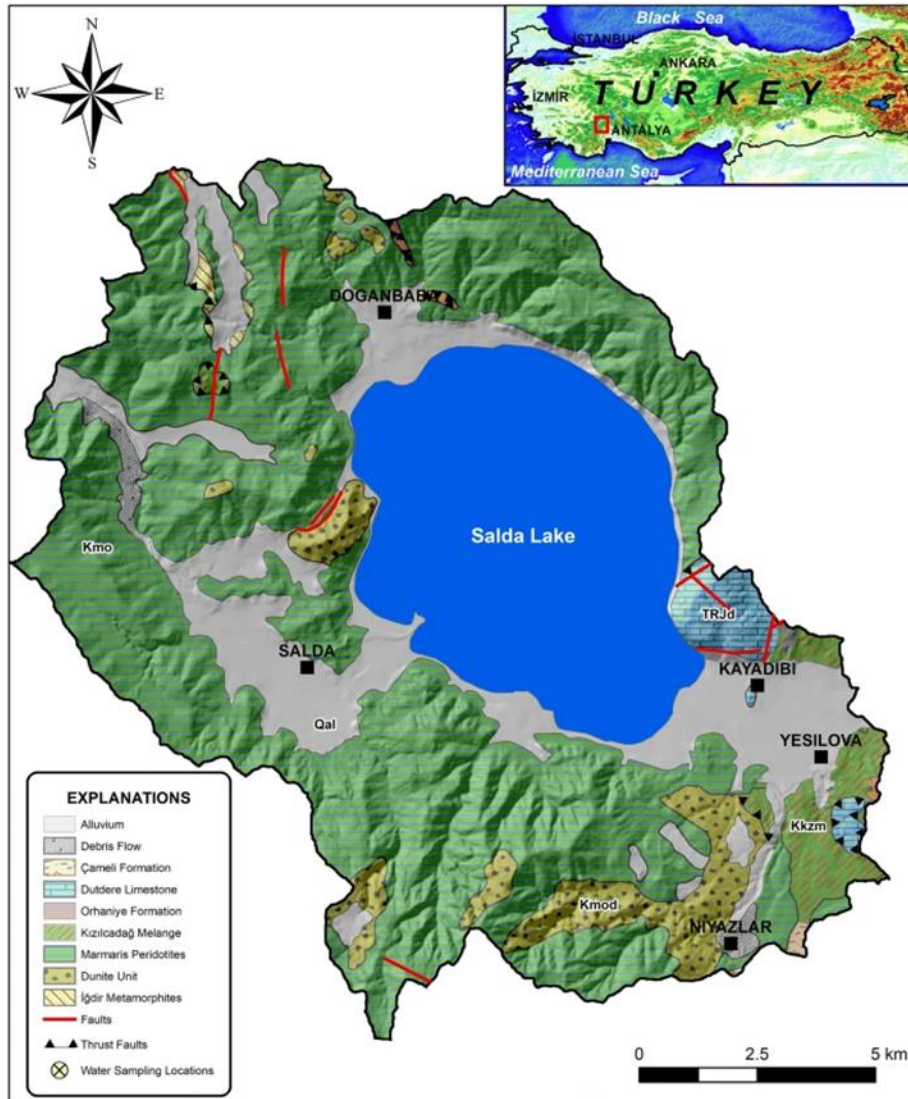
Figure 6. Geology of Lake Salda, Turkey taken from Duvraz et al., (2019).

2.6. Sample descriptions and preparation

Samples included in this study are a mix of whole rocks (including exterior surfaces and polished interior surfaces), unsorted powders (<1000 µm), and <45 µm fine-grained powders; sample descriptions are provided in **Tables 1 and 2**. Field samples were attained in the form of whole rocks (**Figure 2**) along with unsorted sediment samples noted as unsorted powders (<1000 µm) in this study. The polished interior surfaces were prepared by sanding down the side of the whole rock samples (**Figure 3**). The powder samples were prepared by crushing a subsample of each size in an alumina mortar and pestle and dry sieved with a combination of shaking and gently brushing the crushed sample while in the sieve.

791   **Table 1.** Environmental conditions at the analog sites, bedrock geology, and precipitates.

Analog sites	Temp ave (°C)	pH	Basin	Precipitation (mm/year)	Geology	Precipitates
Atlin playas and bedrock regions	0.5	8.0-8.6	Closed, groundwater	348	Ultramafic: harzburgite, dunite, pyroxenite	Hydromagnesite, magnesite, nesquehonite, langsfordite, dypingite, aragonite
Clinton Creek	-4.4	8.4	Closed	324	Ultramafic: chrysotile, antigorite, serpentine, harzburgite, lherzolite, dunite, pyroxenite	Aragonite, clinochrysotile, magnesium-rich calcite, quartz, and possible vermiculite
Lake Alchichica	14.4	8.7	Closed, groundwater	400	Mafic and sedimentary: Limestone, shale, basaltic andesites, pyroclastic deposits, lacustrine deposits	Aragonite, calcite, hydromagnesite, huntite
Lake Salda	11.5	>9	Open, groundwater	493	Mafic/ultramafic: harzburgite and serpentinized harzburgite, lizardite, dunite, limestone	Hydromagnesite, magnesite

792

793   **Note:** The geology column compositions were determined from the literature (Power et al., 2014; Hansen et al.,
794   2005; Beinlich et al., 2012, 2020; Chako-tchamabe et al., 2020; Russell et al., 1999; Davraz et al., 2019). The
795   precipitates column compositions were determined through literature (Power et al., 2007, 2009, 2011, 2014;
796   Kaźmierczak et al., 2011; Armienta et al., 2008; Braithwaite and Zedef, 1996; Russell et al., 1999) and X-ray
797   diffraction performed as part of this study.

798   **Table 2.** Descriptions of carbonate samples acquired at the analogue sites.

Sample	Description
ATP1	Atlin pisolith from Atlin playas: cemented 1-4 mm pisoliths; composed of aragonite; medium brown color; few grams sample.
ATM1	Atlin microbialite sample from Atlin playas: few grams of porous beige-brown fragment; composed of aragonite.
ATA1	Atlin aragonite consolidated sediments from Atlin playas. Acquired from depth of 30-40 cm; few grams of friable fragments of light brown material and abraded powder.
ATH	Atlin hydromagnesite and magnesite sediments from Atlin playas: surface sample; few grams of fine-grained white powder.
16AT-ANNA	White-orange-blue fragments and fine-grained white powder.
16AT-PI-1	White-orange-blue fragments and fine-grained white powder.
16AT-PI-2	White-orange-blue fragments and fine-grained white powder.
CC1	Clinton Creek microbialite. Dark gray.

LAL-C1	Lake Alchichica column-like microbialite. White and brown. Coated with what looks like a biological film.
LAL-E1	Lake Alchichica esponja (sponge-like) microbialite. More white than brown regions.
LS1	Rock. Lake Salda microbialite. White.

799 **Abbreviations:** AT: Atlin; CC: Clinton Creek. LAL: Lake Alchichica. LS: Lake Salda

800 ## 3. Analytical methods

801 ### 3.1. Reflectance spectroscopy

802   An Analytical Spectral Devices (Boulder, CO) LabSpec 4 Hi-Res® spectrophotometer was

803 used to characterize the samples whole rock exterior, unsorted (<1000 µm), and <45 µm surface

804 by collecting reflectance spectra from 350 to 2500 nm at a viewing geometry of i=30° and e=0°.

805 An in-house tungsten light source was used to provide incident lighting with a divergence of

806 <1.5°. A total of 500 spectra per sample, standard, and dark current were acquired and averaged

807 to improve the signal-to-noise ratio (SNR). The spectrometer collects data with a spectral

808 resolution of between 2 and 7 nm, and a spectral sampling interval of 1.4 nm at 350-1000 nm

809 (0.35-1 µm); 2.2 nm at 1000-2500 nm (1-2.5 µm), which is then internally resampled by the

810 spectrometer to output data at 1 nm intervals. The spectra were corrected for dark current, small

811 absorption features beyond 2 µm in the absolute reflectance of Spectralon, as well as occasional

812 small reflectance offsets at 1000 and 1830 nm, where detector changeovers occur. Laboratory

813 spectra were acquired, both as whole rocks on exterior surfaces, unsorted powders (<1000 µm),

814 and <45 µm powders. This study objective was to determine any spectral differences from

815 analysing whole rock samples and unsorted powders (sediments) that were collected in the field

816 at our analogue sites similar to what would be identified on Mars. The use of <45 µm powders

817 provides a more homogeneous mixture for spectral analysis, it provides a similar to grain size

818 Martian dust, and is easily compared to other datasets. The spot size for all the samples was ~ 6.2

819 mm. Reflectance spectra of <45 µm powders of pure aragonite (CRB124) and magnesite

820 (CRB106) were collected from RELAB (Reflectance Experiment Laboratory) and

821 hydromagnesite (CRB404) collected from C-TAPE all <45 µm spectra. These samples were

822 analysed as pure end member standards to our microbialite samples. These samples are not

823 lacustrine in origin and XRD was used to confirmed the purity of the samples.

824 ### 3.2. Raman spectroscopy

825   A BWTek BWS415 iRaman spectrometer with a 532 nm laser was used to characterize the

826 samples whole rock exterior, unsorted (<1000 µm), and <45 µm surfaces. The laser is coupled to

827   a silica fiber optic bundle and passed through a quartz focusing lens, which achieves a spot

828   diameter of ~85 μm FWHM while in focus. The Raman scattered light is collected through the

829   quartz lens, transmitted through an OD6 notch filter to remove the Rayleigh line, then coupled to

830   a silica fiber. The Raman scattered light is transmitted through a collection slit onto a diffraction

831   grating, and the light is then measured with a linear array CCD thermoelectrically stabilized at

832   14°C. This setup achieves a sampling interval of 2.85 Δcm^{-1} at 172 Δcm^{-1}; 1.45 Δcm-1 at 4002

833   Δcm^{-1}; and a spectral resolution of roughly 4 Δcm^{-1} FWHM (Full Width Half Maximum). The

834   system covers the spectral range of 175 to 4000 Raman shift ($\Delta\ cm^{-1}$). A laser power of 50 mW

835   was used, and various integration times were used, depending on the Raman scattering and

836   fluorescence of the samples, to achieve optimal S/N (Signal/Noise). The Raman spectra were

837   relative intensity corrected, per ASTM E2911 – 13. Raman spectra of <45 µm powders of pure

838   aragonite (CRB124), magnesite (CRB106), and hydromagnesite (CRB404) were collected using

839   the 532 nm laser Raman spectrometer to be analyzed as pure end-member standards to our

840   microbialite samples.

841 **3.3.   X-ray diffraction (XRD)**

842   XRD characterization of the samples was done using <45 µm powders. The XRD analysis

843   involved acquiring continuous scan data from 5 to 80º 2θ on a Bruker D8 Advance with a

844   DaVinci automated powder diffractometer. A Bragg-Brentano goniometer with a theta-theta

845   setup was equipped with a 2.5° incident Soller slit, a 1.0 mm divergence slit, a 2.0 mm scatter

846   slit, a 0.2 mm receiving slit, a curved secondary graphite monochromator, and a scintillation

847   counter collecting at an increment of 0.02° and integration time of 1 second per step. The line

848   focus Co X-ray tube was operated at 40 kV and 40 mA, using a take-off angle of 6º. Standard

849   peak matching was done using the PDF-2 database, the peak identified spectra were than

850   extracted as PDF's.

851 **3.4.   Scanning electron microscopy**

852   A Hitachi FlexSEM 1000 II was used to collect backscattered electron (BSE) images and

853   perform elemental mapping on uncoated samples at a working distance of ~10 mm. Variable

854   pressure mode (30 Pa air) was used to reduce charge buildup with ~15kV. X-ray elemental maps

855   were acquired using a Silicon Drift Detector (SDD) at the same working distance. Various

856   accelerating voltages and beam currents were used, depending on the target. The BSE and X-ray

857 maps were used to characterize variations in composition within the samples. Regions of interest,

858 interesting features, and organics were mapped at a higher resolution than the whole rock

859 elemental maps. The samples were not carbon-coated for analysis so that maps of carbon content

860 could be produced.

3.5. X-ray fluorescence and wet chemistry

862 Compositional analysis was carried out at Franklin and Marshall College using X-ray

863 fluorescence (XRF) to identify major and selected minor elements and wet chemistry (WC) to

864 determine ferrous iron content. Details of the procedures can be found in Reichen and Fahey

865 (1962), Govindaraju (1994), and Mertzman (2000). Compositional data are provided in **Table 3**.

866 **Table 3.** Compositional data for the analogue microbialite samples and Atlin region bedrock: X-ray fluorescence
867 and wet chemistry analyses.

SAMPLE ID WT.%	ATA	ATH	ATM	ATP	CC	LAL-C	LAL-E
SIO_2	7.30	1.56	4.48	3.29	24.39	1.12	6.47
TIO_2	0.01	0.00	0.01	0.01	0.31	0.01	0.03
AL_2O_3	0.11	0.15	0.13	0.13	5.76	0.28	0.75
$(FE_2O_3)^A$	4.59	0.20	1.81	1.88	3.50	0.57	6.38
MNO	0.05	0.00	0.69	0.06	0.11	0.03	0.24
MGO	5.30	97.45	1.78	2.23	7.98	76.52	6.92
CAO	81.31	0.22	89.81	91.02	56.14	21.01	76.45
NA_2O	0.06	0.28	0.02	0.06	0.23	0.32	0.69
K_2O	0.02	0.02	0.02	0.02	0.85	0.05	0.15
P_2O_5	0.06	0.03	0.02	0.01	0.09	0.05	0.30
SO_3	0.00	0.03	0.00	0.00	0.05	0.09	0.26
CL	0.00	0.08	0.08	0.06	0.00	0.05	0.00
$TOTAL^B$	**98.81**	**100.02**	**98.85**	**98.77**	**99.41**	**100.10**	**98.64**
LOI^C	44.50	56.79	44.20	43.96	34.69	56.55	45.80
FEO^D	1.35	0.06	0.83	0.31	0.66	0.09	0.84
$FE_2O_3{}^D$	3.09	0.13	0.89	1.54	2.77	0.47	5.45
PPM:							
RB	17	<2	20	20	49	5	15
SR	7596	71	10463	10696	3828	1371	5905

ZR	<2	8	<2	<2	<2	5	<2
CR	<2	<2	<2	<2	324	<2	<2
V	13	<2	11	<2	62	5	9
BA	1026	40	588	526	648	334	1666

SAMPLE ID WT.%	LS	16AT-ANNA	16AT-PI-1	16AT-PI-2	CRB124	CRB106	CRB404
SIO_2	1.45	73.59	48.01	50.88	0.00	0.19	0.00
TIO_2	0.00	0.00	0.00	0.02	0.00	0.00	0.00
AL_2O_3	0.15	0.70	1.33	1.87	0.00	0.08	0.05
$(FE_2O_3)^A$	0.03	6.06	8.73	8.11	0.10	1.38	0.22
MNO	0.00	0.09	0.16	0.14	0.00	0.03	0.03
MGO	95.35	18.02	39.12	37.13	0.19	96.73	98.55
CAO	2.59	1.17	2.86	1.22	99.52	1.59	0.61
NA_2O	0.19	0.00	0.04	0.03	0.35	0.00	0.15
K_2O	0.00	0.08	0.18	0.06	0.00	0.00	0.00
P_2O_5	0.00	0.00	0.00	0.00	0.02	0.02	0.017
SO_3	0.03	0.00	0.00	0.00			0.11
CL	0.06	0.00	0.04	0.00			
$TOTAL^B$	**99.85**	**99.71**	**100.47**	**99.46**	**100.18**	**100.02**	**99.791**
LOI^C	56.93	19.15	32.98	30.96	43.66	51.55	61.42
FEO^D	0.00	4.35	5.24	4.38		0.73	0.17
$FE_2O_3{}^D$	0.03	1.23	2.91	3.24		0.57	0.03
PPM:							
RB	<2	<2	7	<2	<2	40	<1
SR	53	<2	23	79	109	73	199
ZR	10	8	8	5	10	5	27
CR	<2	337	3300	2531	<2	<2	<1
V	5	9	32	57	15	3	30
BA	34	32	149	56			

868   a - all Fe reported as Fe_2O_3.
869   b – total expressed on a volatile-free basis and with all Fe reported as Fe_2O_3.
870   c – LOI: loss on ignition; % weight loss after heating sample in air for 60-90 minutes.
871   d - FeO was determined by wet chemistry (WC) and Fe_2O_3 was taken as difference between total Fe and FeO.
872   **Note:** Source and Analysis: Mertzman. Analyses by Stan Mertzman at Franklin and Marshall College (see
873   Mertzman, 2000). Analysis done by XRF and wet chemistry (for Fe oxidation state determination).
874   **Note:** ATA, ATH, ATM, ATP, CC, LAL-C, LAL-E, and LS are the precipitate samples.

875　　　　16AT-ANNA, 16AT-PI-1, and 16AT-PI-2 are the bedrock samples.
876　　　　CRB124, CRB106, and CRB404 are the pure end member samples.

4. Results

878　**Table 4.** Phases in the samples for all analogue sites using whole rock, unsorted (<1000 µm), and <45 µm powders
879　identified by reflectance spectroscopy, Raman spectroscopy, X-ray diffractometry (XRD), and spatial distribution of
880　elements studied by scanning electron microscopy.

Location	Sample	Reflectance	Raman	XRD	SEM
Atlin	ATP1	Magnesite, Aragonite	Aragonite		Ca, Mg, O, C
	ATP2	Magnesite, Aragonite	Aragonite		
	ATP3	Magnesite, Aragonite	Aragonite	Aragonite, magnesite	
	ATM1	Magnesite, Aragonite	No phase identified		Ca, Mg, O, C
	ATM2	Magnesite, Aragonite	Aragonite		
	ATM3	Magnesite, Aragonite	No phase identified	Aragonite, magnesite	
	ATA1	Magnesite, Aragonite	No phase identified		Ca, O, C
	ATA2	Magnesite, Aragonite	No phase identified		
	ATA3	Magnesite, Aragonite	No phase identified	Aragonite, hydromagnesite	
	ATH1	Hydromagnesite	No phase identified		N/A
	ATH3	Hydromagnesite	No phase identified	Hydromagnesite, magnesite	
	16-AT-PI-1	Magnesite, Dolomite	Magnesite, quartz	Magnesite, quartz, dolomite	
	16-AT-PI-2	Magnesite, Dolomite	Magnesite, quartz	Magnesite, quartz, dolomite	
	16-AT-Anna	Magnesite, Dolomite	Magnesite, quartz	Magnesite, quartz, dolomite	
Clinton Creek	CC1	Aragonite	No phase identified		Ca, Mg, O, C, Al
	CC2	Aragonite	No phase identified		
	CC3	Aragonite	No phase identified	Aragonite, quartz, muscovite, lizardite, antigorite	

Lake Alchichica	**LAL-C1**	Hydromagnesite, Chlorophyll/ Carotenoids	Chlorophyll/ Carotenoids		Ca, Mg, O, C
	LAL-C2	Hydromagnesite, Chlorophyll/ Carotenoids	No phase identified		
	LAL-C3	Hydromagnesite, Chlorophyll/ Carotenoids	No phase identified	Hydromagnesite, aragonite	
	LAL-E1	Hydromagnesite, Aragonite, Chlorophyll/ Carotenoids	No phase identified		Ca, Mg, O, C
	LAL-E2	Hydromagnesite, Aragonite, Chlorophyll/ Carotenoids	No phase identified		
	LAL-E3	Hydromagnesite, Aragonite, Chlorophyll/ Carotenoids	No phase identified	Aragonite, hydromagnesite, magnesite	
Lake Salda	**LS1**	Hydromagnesite, Chlorophyll/ Carotenoids	No phase identified		Ca, Mg, O, C
	LS2	Hydromagnesite, Chlorophyll/ Carotenoids	Hydromagnesite and magnesite		
	LS3	Hydromagnesite, Chlorophyll/ Carotenoids	No phase identified	Hydromagnesite, aragonite	

881

882 **Note:** XRD was not conducted on Whole rock or unsorted powder (<1000 µm) samples therefore, the entry was left
883 blank. SEM results were only collected on whole rock samples therefore, both the powdered sample entries were left
884 blank.

885 **4.1.   Reflectance Spectra**

886 **4.1.1. Carbonates**

887   Carbonate minerals have several characteristic spectral features that can be identified

888 using near- and mid-infrared wavelength ranges. On Mars, carbonate minerals are typically

889 identified by paired absorption bands at ~2.3 and ~2.5 µm (Ehlmann et al., 2008b, 2009). Longer

890 wavelength absorption features, such as near 3.4 and 3.9 µm are usually outside the wavelength

891 range of Mars orbiters and rovers (Goudge et al., 2015) and fall in a wavelength region of low

892 reflectance and emittance. The ~2.3 and 2.5 µm absorption bands are caused by the overtone of

893 the fundamental vibration mode of the CO_3^{-2} within the mineral structure (Schroeder et

894 al., 1962). The position of these absorptions is controlled by crystal structure as well as the

895 cation(s) present in the sample (Hunt and Salisbury, 1971; Gaffey, 1987). The ~3.4 and 3.9 µm

896 absorption bands are also caused by various combination tones and overtones of the fundamental

897 vibration modes of CO_3 (e.g., Schroeder et al., 1962). Carbonate end-members reflectance

898 spectra are identified in **Figure 7** of pure aragonite (CRB124), magnesite (CRB106) collected

899 from RELAB and hydromagnesite (CRB404) collected from C-TAPE. Carbonate band positions

900 are identified in **Table 5** for several relevant end members. Several types of hydrated Mg-

901 carbonates exist that exhibit distinct spectral properties compared to magnesite (Calvin et al.,

902 1994; Harner and Gilmore, 2015). The type of hydration within hydrous/hydroxylation

903 carbonates can influence their spectral properties (e.g., Calvin et al., 1994; Harner and Gilmore,

904 2015).

905 **Table 5.** Absorption band minima positions in reflectance spectra of various end member carbonates.

Carbonates	~1.4 µm region	~1.9 µm region	~2.3 µm region
Magnesite	1.4	1.9	2.30-2.31
Hydromagnesite	0.96, 1.4, 1.44, 1.46	1.96	2.26, 2.28, 2.32, 2.36, 2.43
Aragonite	1.4	1.9	2.33
Dolomite	1.4	1.9	2.32

906

907 Sources of data: Gaffey (1987); Bishop et al. (2013), Ehlmann et al., 2008b and Horgan et al. (2020).

908   For magnesite (ideal formula: $MgCO_3$), strong vibrational absorptions due to various

909 CO_3^{-2} combinations and overtones are found near 2.30, 2.50, 3.27, 3.42 and 3.95 µm in

910 magnesite spectra (e.g., Gaffey, 1987; Clark et al., 1990; Bishop et al., 2011; Ehlmann et al.,

911 2008b). Magnesite is an anhydrous mineral; however, it commonly exhibits hydration-associated

912 features near 1.4 and 1.9 µm due to incipient alteration and/or accessory phases and may have

913 formed through the dehydration or recrystallization of hydromagnesite (Horgan et al., 2020)

914 (**Figure 7**). Magnesite spectra often exhibit a broad variable-intensity absorption feature below

915 ~1.5 µm, that consists of two partially-overlapping absorption bands near 1.0 and 1.2 µm, which

916   are due to small amounts of Fe^{2+} (which can substitute for Mg) that undergo crystal field

917   transitions (Bishop et al., 2013).

918   Hydromagnesite (ideal formula: $Mg_5(CO_3)_4(OH)_2·4H_2O$) is the most stable and common

919   Mg-carbonate phase that includes both OH and H_2O in its crystal structure (Calvin et al., 1994;

920   Harner and Gilmore, 2015). The presence of OH and H_2O in its structure leads to additional

921   absorption bands beyond those associated with CO_3, as well as differences in the position of C-O

922   absorption bands as compared to magnesite. Hydromagnesite spectra exhibit sharp OH-related

923   bands at ~0.96 and ~1.4 µm, which are superposed on broader OH/H_2O-related bands at ~1.44

924   and 1.96 µm (Harner and Gilmore, 2015; Horgan et al., 2020). At longer wavelengths, the

925   carbonate 2.3 µm doublet band is replaced by a shallow triplet with centers near 2.26, 2.28, 2.32,

926   2.36, and 2.43 µm, with an additional shallow band at 2.53 µm (Harner and Gilmore, 2015;

927   Ehlmann et al., 2008b). At longer wavelengths, hydromagnesite has C-O-associated absorption

928   bands at ~2280, 2330, and 2430 nm (**Figure 7**).
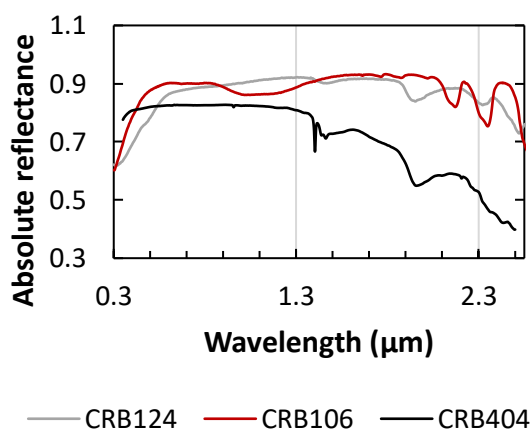
929

930   **Figure 7.** Reflectance spectra of <45 micron powders with a wavelength range of 0.35–2.5 µm collected at C-TAPE
931   of pure aragonite (CRB124), magnesite (CRB106) collected from RELAB and hydromagnesite (CRB404) collected
932   from C-TAPE all <45 micron spectra. XRD confirmed the purity of the samples.

933   **4.1.2. Microbialites**

934   In addition to carbonate absorption features, all the analogue site samples exhibit

935   characteristic spectral features associated with OH/ H_2O, and H_2O around 1.4 and 1.9 µm,

936   respectively (**Figures 8-11**). The reflectance spectra indicated that these samples are hydrous

937   carbonates or contain a spectrally-significant number of hydrous carbonates. The ATH, LAL-C,

938   and LS spectra show additional sharp OH absorption bands at 0.96, 1.4, and 1.44 µm that

939 represent additional higher-level overtones and combination bands (Clark et al., 1990) that are

940 superposed on the OH/H_2O bands at 1.44 and 1.96 (**Figure 8d, 10a, and 11**), associated with

941 hydromagnesite (Harner and Gilmore, 2015; Ehlmann et al., 2008b). The LAL-E1 whole rock

942 spectrum has sharp bands present at 0.96, 1.4, 1.44, and 1.96 µm which become less distinct in

943 the two powdered spectra (LAL-E2 and LAL-E3) (**Figure 10b**).

944   Carbonate C-O associated features are seen at ~2.3 µm in all the microbialite samples.

945 Two superimposed absorption bands appear in the Atlin sample spectra, making up the wide 2.3

946 µm feature, which has a downturned slope towards longer wavelengths, with band centers at 2.31

947 µm and 2.33 µm. The sample is likely a mixture of magnesite (2.3 µm) and aragonite (2.33 µm)

948 (Gaffey, 1987; Ehlmann et al., 2008b) (**Table 3 and Figures 8a-c**). The ATH, LAL-C, and LS

949 spectra exhibit differences in their C-O band position compared to other magnesite samples

950 (Russell et al., 1999), with minima present at 2.26, 2.32, and 2.43 µm, consistent with

951 hydromagnesite (Harner and Gilmore, 2015) (**Table 3 and Figures 8d, 10a, and 11**). XRD of

952 the Atlin samples identified aragonite as the primary mineral apart from ATH, which identified a

953 mixture of hydromagnesite and magnesite (**Table 2**). The Clinton Creek microbialite spectra are

954 largely featureless in the <45 µm powder spectra with absorption bands near 1.4, 1.9, and ~2.35

955 µm associated with aragonite. The Clinton creek XRD identified aragonite and some

956 phyllosilicate minerals (lizardite and antigorite) which may indicate the shift to further

957 wavelengths away from pure aragonite (2.33 µm).

958   The LAL-E spectra show an absorption band at ~2.33 µm, consistent with aragonite. The

959 LAL-E sample spectrum exhibits the distinct OH/ H_2O absorption band of hydromagnesite in the

960 1.4 µm region, while not having the characteristic C-O feature near 2.3 µm that would also be

961 associated with pure hydromagnesite. Instead, the spectra exhibit a likely mixture of

962 hydromagnesite as seen in the sharp hydration feature ~1.4 µm and aragonite as seen in the wide

963 absorption band centered at 2.33 µm with a downturned slope towards longer wavelengths due to

964 the influence of Ca in the spectrum (Ehlmann et al., 2008b) (**Figure 10b**). XRD indicates the

965 primary mineralogy of the LAL-E sample to be aragonite while it determined hydromagnesite to

966 dominate the LAL-C sample (**Table 2**). Chlorophyll-associated absorption bands at 0.67 µm

967 (Das et al., 2005; Wolfe et al., 2006) are found in the LAL-C, LAL-E, and LS samples (**Figures**

968 **10 and 11**). The exterior of the LAL-C whole rock sample has a potential biofilm however, all

969 spectra exhibited the 0.67 µm absorption band.

970   XRD peak matched figures can be found in the supplementary materials (**Figures 8-18**).
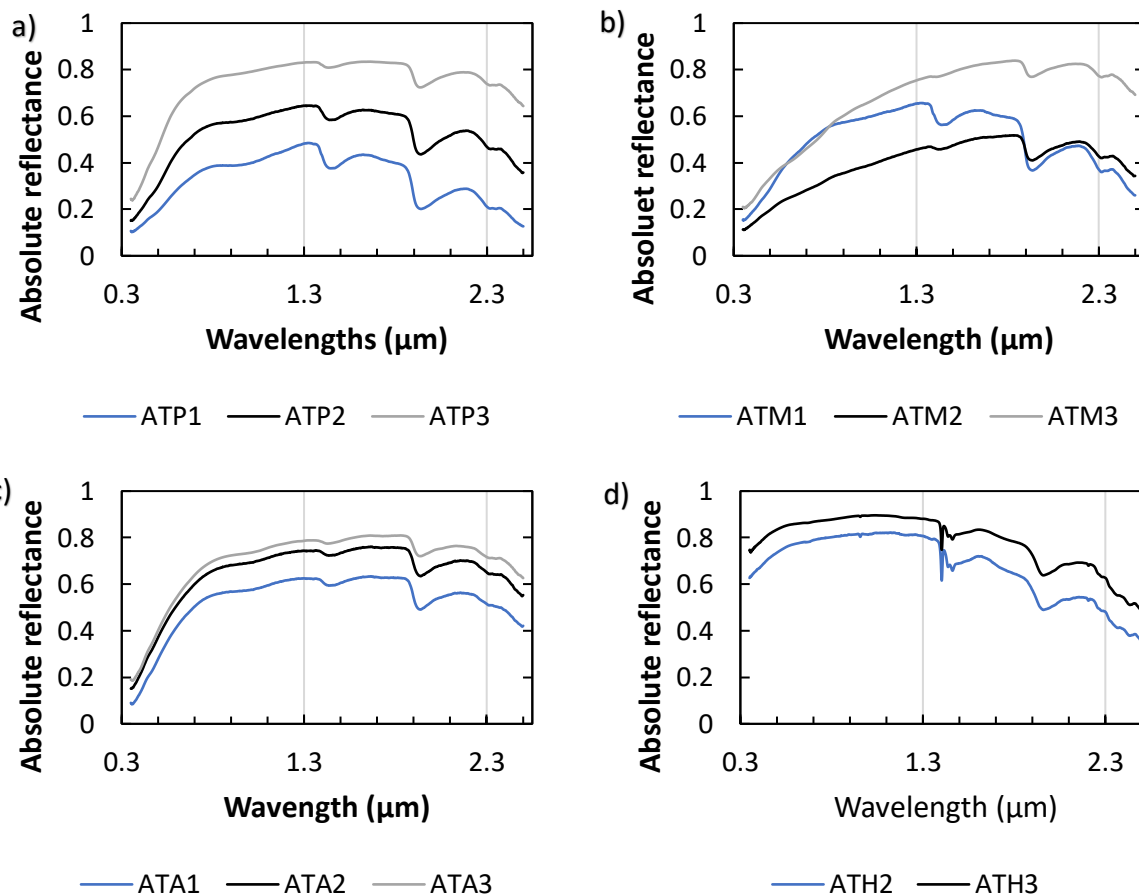
971

972

973 **Figure 8**. Reflectance spectra with a wavelength range of 0.35–2.5 µm collected at C-TAPE of a) Atlin playa
974 pisolite samples ATP1, ATP2, ATP3, b) Atlin microbialite samples ATM1, ATM2, ATM3, c) Atlin consolidated
975 sediments ATA1, ATA2, ATA3, d) Atlin hydromagnesite and magnesite sediments ATH2, ATH3. All samples
976 exhibit spectral features associated with OH/ H_2O, and H_2O around 1.4 and 1.9 µm. Figures 8a-d exhibit two
977 superimposed absorption bands making up the wide 2.3 µm magnesite and aragonite feature while figure 8d exhibit
978 a hydromagnesite feature with minima present at 2.26, 2.32, and 2.43 µm.

979 Note: 1 at the end indicates the spectrum was collected using the whole rock, 2 indicates the spectrum was collected
980 using unsorted powders (<1000 µm) and 3 indicates the spectrum was collected using <45 µm powders.
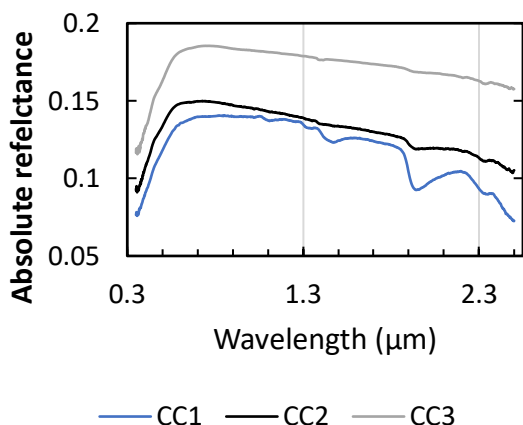
Figure 9. Reflectance spectra with a wavelength range of 0.35–2.5 µm collected at C-TAPE of Clinton Creek samples CC1, CC2, CC3. The microbialite exhibits spectral features associated with OH/ H$_2$O, and H$_2$O around 1.4 and 1.9 µm and an aragonite absorption feature at 2.3 µm.

Note: 1 at the end indicates the spectrum was collected using the whole rock, 2 indicates the spectrum was collected using unsorted powders (<1000 µm) and 3 indicates the spectrum was collected using <45 µm powders.
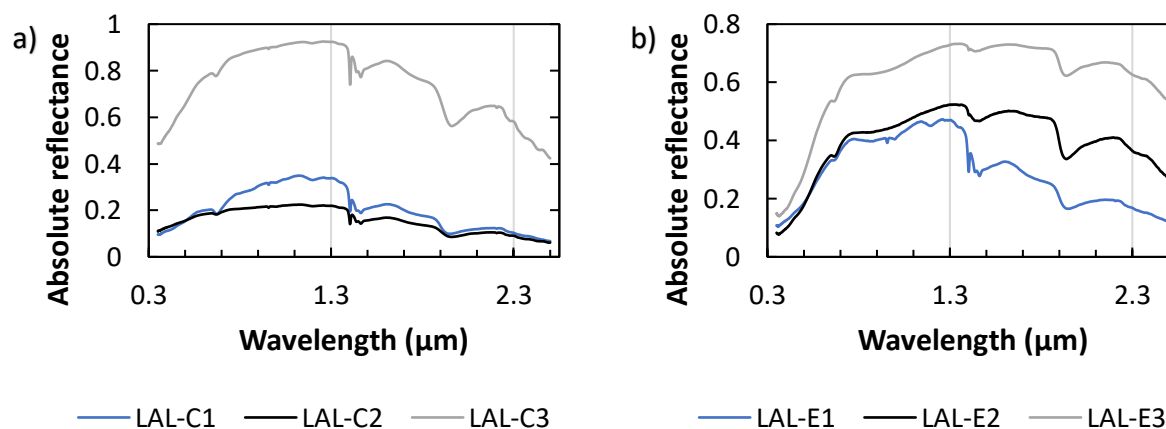
Figure 10. Reflectance spectra with a wavelength range of 0.35–2.5 µm collected at C-TAPE of a) of Lake Alchichica column-like microbialite LALC1, LALC2, LALC3 and b) Lake Alchichica esponja (sponge-like) microbialite LALE1, LALE2, LALE3. All samples exhibit spectral features associated with OH/ H$_2$O, and H$_2$O around 1.4 and 1.9 µm. Figures 10a exhibit a hydromagnesite feature with minima present at 2.26, 2.32, and 2.43 µm. Figure 10b exhibits a likely mixture of hydromagnesite as seen in the sharp 0.96, 1.4, and 1.44µm and aragonite as seen in the wide absorption band centered at 2.33 µm with a downturn to longer wavelengths.

Note: 1 at the end indicates the spectrum was collected using the whole rock, 2 indicates the spectrum was collected using unsorted powders (<1000 µm) and 3 indicates the spectrum was collected using <45 µm powders.
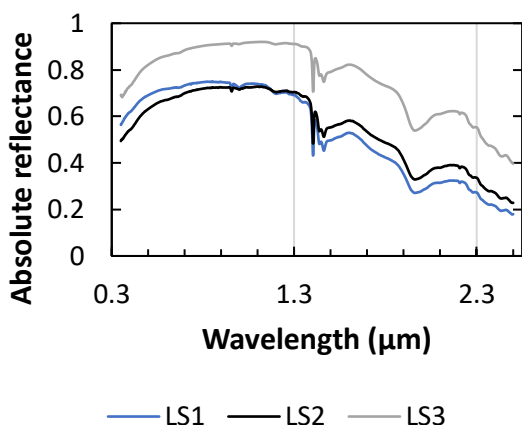
Figure 11. Reflectance spectra with a wavelength range of 0.35–2.5 µm collected at C-TAPE of Lake Salda samples LS1, LS2, LS3. The microbialite exhibits spectral features associated with OH/ H_2O, and H_2O around 1.4 and 1.9 µm and carbonate absopriton bands with minima at 2.26, 2.32, and 2.43 µm, consistent with hydromagnesite

Note: 1 at the end indicates the spectrum was collected using the whole rock, 2 indicates the spectrum was collected using unsorted powders (<1000 µm) and 3 indicates the spectrum was collected using <45 µm powders.

4.1.3. Bedrock

The listvenite bedrock samples 16AT-PI-1, 16AT-PI-2, 16AT-Anna from Atlin exhibit H_2O/OH features near 1.4 and 1.9 µm along with a distinct C-O feature at ~2.31 µm. An additional broad Fe^{2+} feature is exhibited between 1.0-1.25 µm (**Figure 12**), consistent with the compositional data (**Table 3**); it is likely present in the carbonate, as this feature is seen in siderite spectra (Gaffey, 1985). The mine samples from around Atlin are highly enriched in iron, which can be related to the breakdown of silicates and oxides in the alteration of serpentine/peridotite to form listvenites. The regional rocks surrounding the Atlin playa indicate the low-temperature carbonation of mafic minerals producing magnesite-rich deposits (Hansen et al., 2005). XRD of the listvenite samples indicated the presence of magnesite, quartz, and dolomite. The absorption feature found at ~2.31 µm is most consistent with a mixture of magnesite and dolomite as the XRD data determined the presence of magnesite and dolomite.
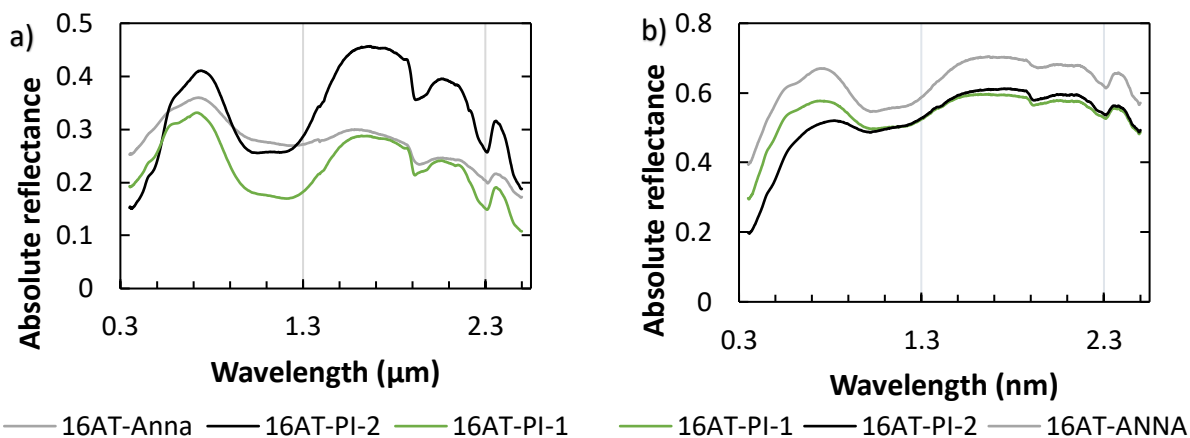
Figure 12. Reflectance spectra with a wavelength range of 0.35–2.5 µm collected at C-TAPE a) Averaged rock reflectance spectra for Pictu (16AT-PI-#) and Anna (16AT-Anna) mine samples. b) <45 µm powder spectra for Pictu (16AT-PI-#) and Anna (16AT-Anna) mine samples. All samples exhibit a broad Fe^{2+} feature is exhibited between 1.0-1.25 µm, H_2O/OH features near 1.4 and 1.9 µm along with a distinct C-O feature at ~2.31 µm associated with magnesite and dolomite.

4.2. Raman spectra

4.2.1. Magnesite and Hydromagnesite

The four Raman bands characteristic of the CO_3^{-2} group are at ~1440, 1088, 715, and 278 cm^{-1} (Sun et al., 2014). The carbonate group's symmetric stretching vibration modes appear at ~1088 cm^{-1} (Sun et al., 2014; Frost et al., 2011) while the asymmetric stretch Raman bands appear near 1400 cm^{-1} (Sun et al., 2014; Frost et al., 2011). In-plane bending mode is exhibited at ~715 cm^{-1} (Sun et al., 2014). Carbonate Raman peak positions are identified in **Table 6** for several relevant end members.

Table 6. Raman spectra peak positions for pure end member carbonates.

Carbonates	Peaks (cm^{-1})
Magnesite	213, 329, 738, 1094, 1444, 1762, (Wang et al., 2006)
	212, 332, 735, 1069, 1460 (Krishnamurti, D., 1956)
Hydromagnesite	1120 (Frost, 2011), 1117-1120 (White 1974; Edwards et al., 2005a), 183, 202, 726, and 1450 (Hopkinson et al., 2008).
Aragonite	700, 704, 852-854, 1082 (Chakrabarty and Mahapatra, 1999)
	1084 (Alia et al., 1997).
Dolomite	1393, 1098, 1069, 1019, 299, 258 and 176 (Sun et al., 2014), 288, 309, 712, 728, 1092 (Gunasekaran et al., 2006)

Sources of data: Krishnamurti (1956); Alia et al. (1997), Chakrabarty and Mahapatra (1999), Wang et al. (2006), Frost (2011), Gunasekaran and Anbalagan, (2007); and Sun et al. (2014).

Our aragonite sample CRB124 exhibits peaks at 1082 cm^{-1} similar to other studies (Chakrabarty and Mahapatra, 1999; Alia et al., 1997). The magnesite CRB106 sample exhibited

1037 Raman peaks at 214, 329, 739, 1092, 1445, and 1763 cm^{-1}, very consistent with previous studies

1038 (Wang et al., 2006), whereas our hydromagnesite sample CRB404 only exhibited a small

1039 undefined peak ~1117 cm-1, which has been attributed to hydromagnesite in previous studies

1040 (Frost, 2011) (**Figure 13**).

Figure with Intensity (y-axis) vs Raman shift (cm^{-1}) (x-axis), showing CRB404, CRB124, and CRB106 spectra.
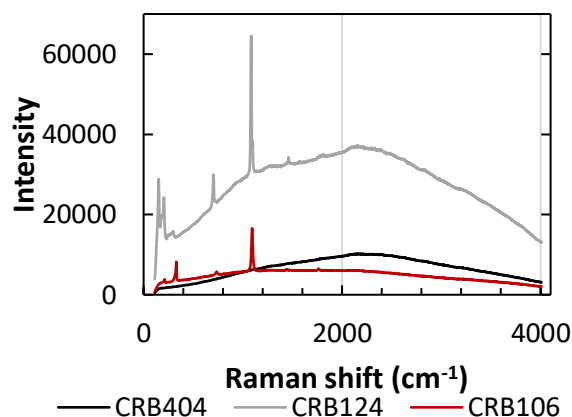
1041

1042 **Figure 13.** Raman spectra collected using a 532 nm laser Raman spectrometer with ranging from 111-4000 cm^{-1} of
1043 <45 micron powders of pure aragonite (CRB124), magnesite (CRB106), and hydromagnesite (CRB404) were
1044 collected using a 532 nm laser.

4.2.2. Microbialites

1046 The Raman spectra acquired for our field site samples were able to discern the presence

1047 and mineralogical variety of carbonates that were present, as well as some accessory phases such

1048 as quartz and organic compounds (**Figures 14-17**). However, it should be noted that a number of

1049 the samples showed no resolvable Raman peaks, perhaps due to high fluorescence, low

1050 crystallinity, or fine grain size. The Atlin playa ATP (1082 cm^{-1}) samples and ATM (1077 cm^{-1})

1051 unsorted powder exhibited weaker peaks at ~1080 cm^{-1} which can be assigned to aragonite

1052 (**Figure 14a and 14b**) (Alia et al., 1997), confirmed in at least one of the ATP samples by XRD.

1053 The Atlin playa samples did not show any clear Raman peaks related to magnesite or

1054 hydromagnesite. Lake Salda spectra presented one weak peak from the unsorted powder at

1055 ~1115 cm-1 associated with hydromagnesite (Frost, 2011) (**Figure 17**), while Clinton Creek did

1056 not exhibit any related peaks in the spectra (**Figure 15**). The LAL-C sample from Lake

1057 Alchichica exhibited clear and definite cyanobacteria/carotenoids peaks at ~1150 and 1510 cm^{-1}

1058 on the whole rock sample (**Figure 16a**) (De Oliveira et al., 2015). However, because this is a

1059 modern sample, its relevance to paleo-biosignature detection on Mars is likely limited.
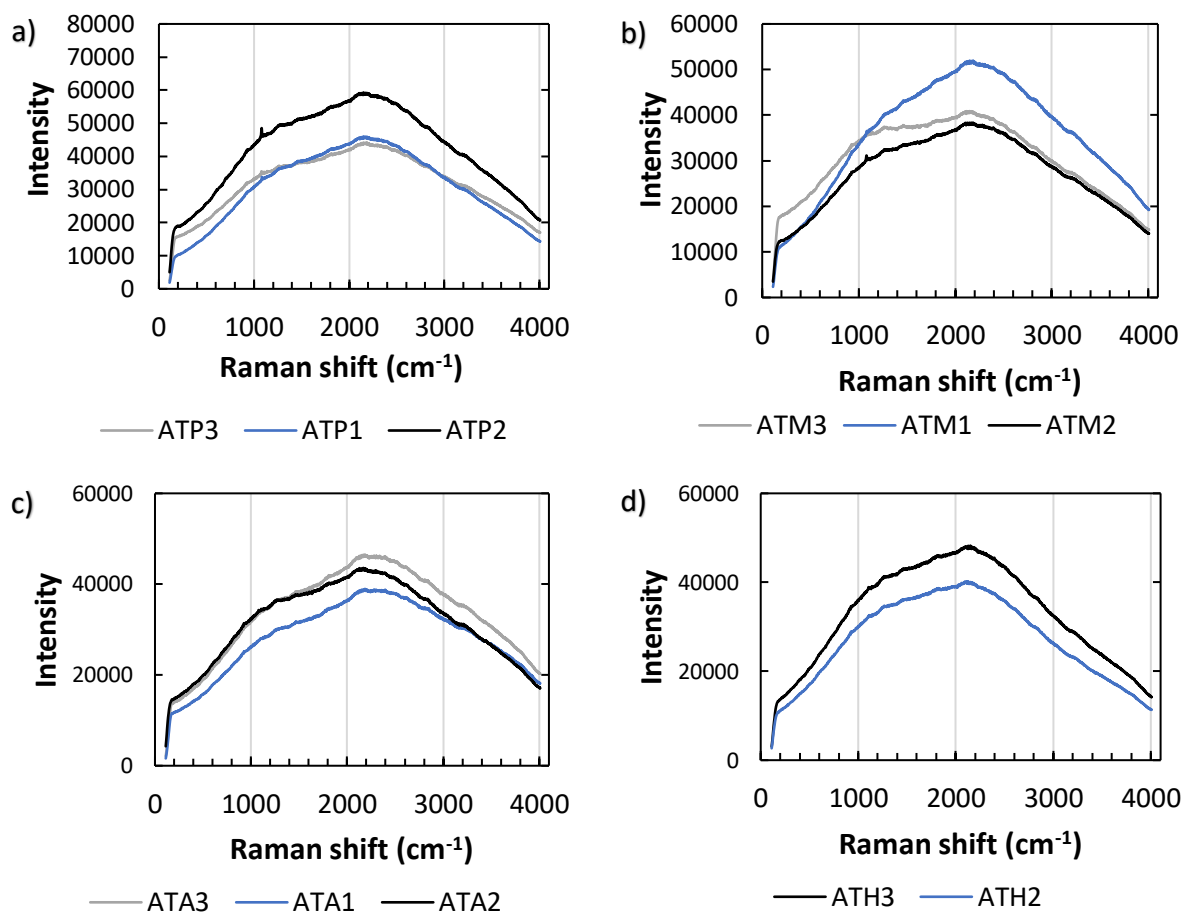
Figure 14. Raman spectra of Atlin playa pisolite samples ATP1 (rock), ATP2 (unsorted), ATP3 (<45 micron), Atlin microbialite samples ATM1, ATM2, ATM3, Atlin consolidated sediments ATA1, ATA2, ATA3, Atlin hydromagnesite and magnesite sediments ATH2, ATH3. The Atlin playa ATP samples and ATM unsorted powder spectra exhibited weaker peaks at ~1080 cm⁻¹ associated with aragonite. The fluorescence hump is seen in all figures with an intensity increase up to ~2000-2500 cm⁻¹ than decreases in intensity.

Note: 1 at the end indicates the spectrum was collected using the whole rock, 2 indicates the spectrum was collected using unsorted powders (<1000 µm) and 3 indicates the spectrum was collected using <45 µm powders.
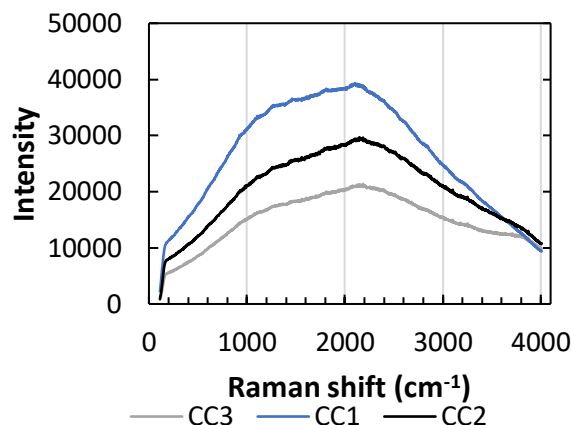
1070

Figure 15. Raman spectra of Clinton Creek CC1, CC2, CC3. The microbialite sample did not exhibited any peaks. The fluorescence hump is seen in all figures with an intensity increase up to ~2000-2500 cm^{-1} than decreases in intensity.

Note: 1 at the end indicates the spectrum was collected using the whole rock, 2 indicates the spectrum was collected using unsorted powders (<1000 µm) and 3 indicates the spectrum was collected using <45 µm powders.
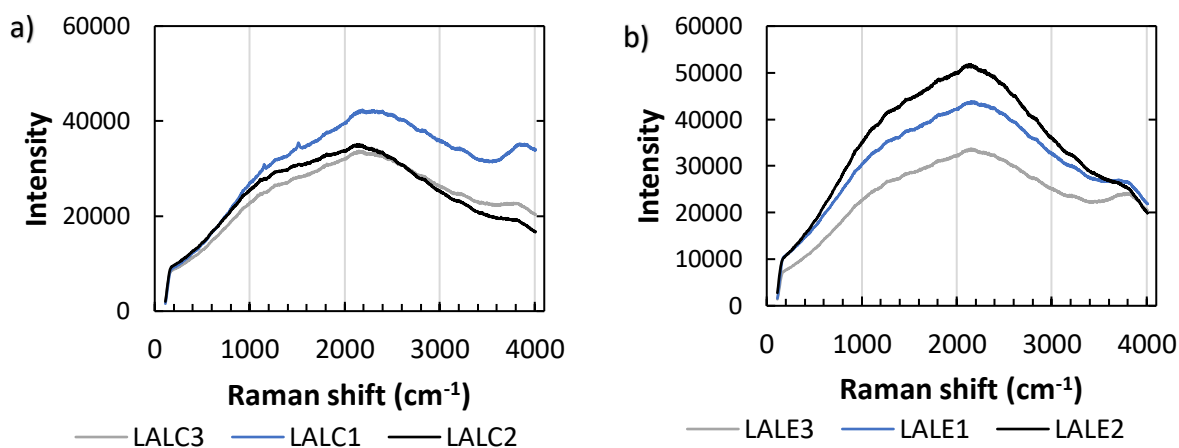
1076

Figure 16. Raman spectra of a) Lake Alchichica column-like microbialite LAL-C1, LAL-C2, LAL-C3 and b) Lake Alchichica esponja (sponge-like) microbialite LAL-E1, LAL-E2, LAL-E3. The LAL-C whole rock sample exhibited cyanobacteria/carotenoids peaks at ~1150 and 1510 cm^{-1}. No other mineralogical peaks are presented. The fluorescence hump is seen in all figures with an intensity increase up to ~2000-2500 cm^{-1} than decreases in intensity.

Note: 1 at the end indicates the spectrum was collected using the whole rock, 2 indicates the spectrum was collected using unsorted powders (<1000 µm) and 3 indicates the spectrum was collected using <45 µm powders.
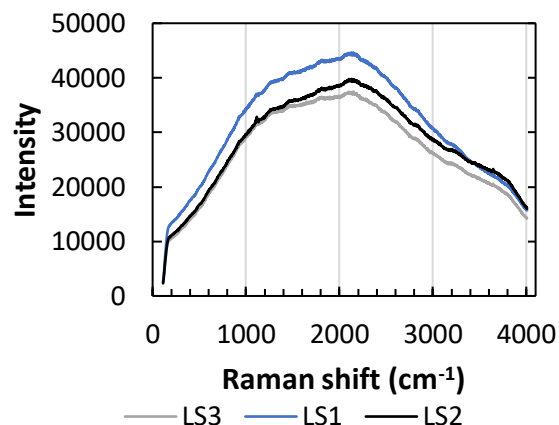
Figure 17. Raman spectra of Lake Salda samples LS1, LS2, LS3. The microbialite sample exhibited one peak from the unsorted powder spectra at ~1115 cm-1 associated with hydromagnesite. The fluorescence hump is seen in all figures with an intensity increase up to ~2000-2500 cm^{-1} than decreases in intensity.

*1 at the end indicates the spectrum was collected using the whole rock, 2 indicates the spectrum was collected using unsorted powders (<1000 µm) and 3 indicates the spectrum was collected using <45 µm powders.

4.2.3. Bedrock

The Atlin bedrock Pictu and Anna mine samples indicate characteristic peaks associated with magnesite at ~ 200, ~320, and ~1094 cm^{-1} (**Figure 18**) (Wang et al., 2012). The Anna Mine <45-micron powder sample exhibited additional magnesite-related Raman peaks at ~1450 and ~1750 cm^{-1} (**Figure 18a**) (Wang et al., 2012). Raman analysis of all the bedrock samples indicated the presence of quartz-based on a peak at 460 cm^{-1}, and the Anna mine sample exhibited a quartz peak at ~1160 cm^{-1} (**Figure 18**) (Sato and McMillan, 1987).
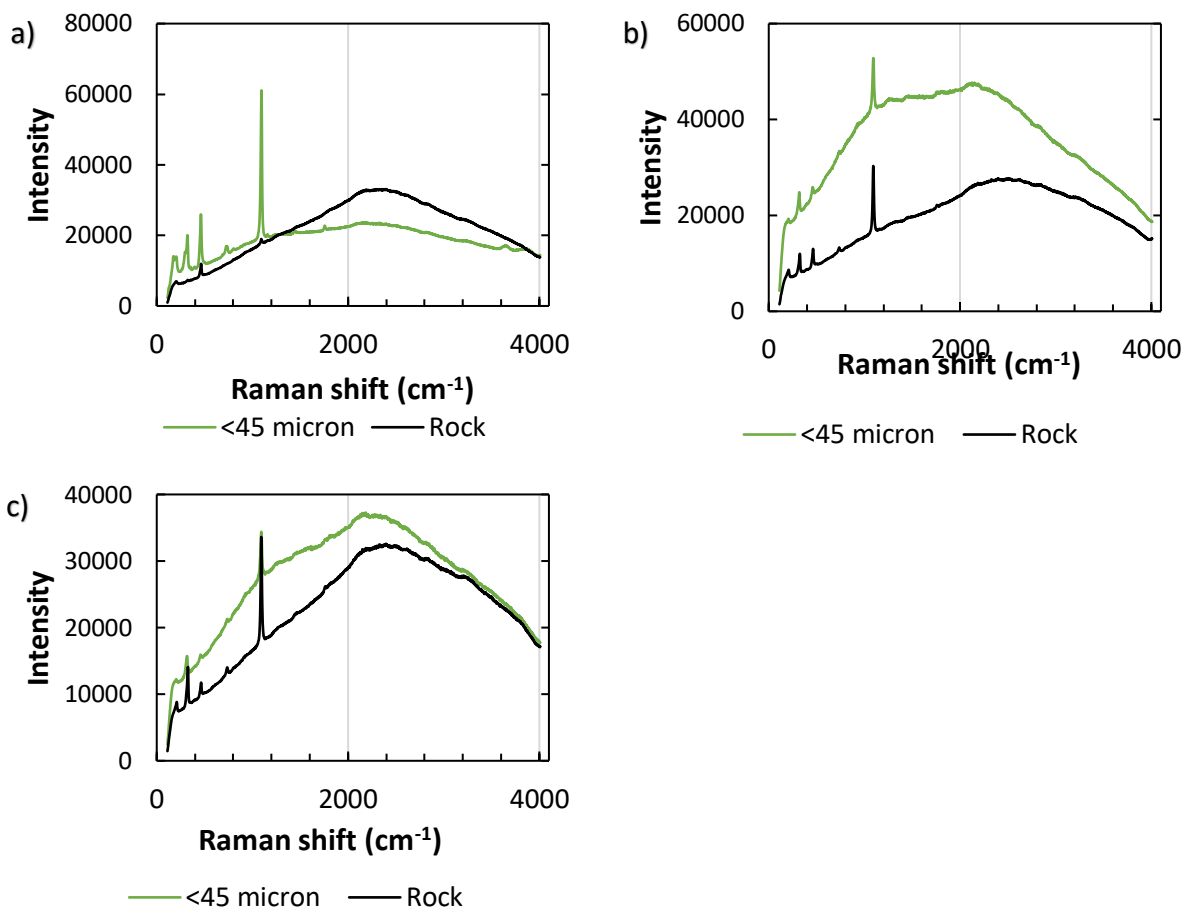
Figure 18. Raman spectra of a) 16AT-Anna, b) 16AT-PI-1, c) 16AT-PI-2 bedrock mine samples for <45 μm and whole rock samples. The Pictu and Anna mine samples exhibit peaks associated with magnesite at ~200, ~320, and ~1094 cm^{-1}. The Anna Mine <45-micron powder spectra exhibited additional magnesite-related Raman peaks at ~1450 and ~1750 cm^{-1}. A quartz-based peak is found in all spectra at ~460 cm^{-1}, and the Anna mine sample exhibited an additional peak at ~1160 cm^{-1}.

4.3.   XRF and wet chemistry (WC)

XRF and WC compositional data has been acquired for all samples in this study; the results are provided in **Table 4**. These data were used largely to support the spectral interpretations of mineralogy such as iron, magnesium and calcium for example listvenite compositions and interpretations to Jezero crater data. We found that the Raman spectra did not exhibit peaks in the microbialite spectra unless ≥90 wt.% MgO or CaO was present. This was in contrast to the lisvanite bedrock samples from Atlin. The 16-AT-Anna sample Raman spectrum showed magnesite peaks with as low as 18 wt% MgO present.

The lack of Raman peaks in many of the microbialite samples may be attributable to a number of factors including the presence of fluorescence. The lower Fe_2O_3 content of the ATP

1113 ATM, ATH, and LS samples – i.e., those that produced Raman peaks - may be attributed to their

1114 lower (<2 wt.% total Fe), while the ATA, CC, LAL-E samples – i.e., those that produced no

1115 well-defined Raman peaks - have ≥3.5 wt.% total Fe, with the exception of LAL-C.

1116 **4.4.   SEM**

1117   The SEM elemental maps depict variations of Ca and Mg content (**Table 4, Figures 1-7 in**

1118 **supplemental materials**). Samples ATP1, ATM1, ATA1, and CC1 have the most Ca content,

1119 with ATP1 and ATM1 exhibiting Mg within the exterior and porous spaces of the samples

1120 shown in yellow (**Figures 1 and 2 in the supplemental materials**); this is consistent with the

1121 reflectance results identifying the presence of both aragonite and magnesite. ATA1 did not show

1122 the presence of Mg in its elemental map (**Figure 3 in the supplemental materials**). CC1

1123 additionally exhibits Al on the exterior of the sample consistent with the presence of 5.76 wt.%

1124 Al_2O_3 from the XRF results (**Figure 4 in the supplemental materials**). LAL-C1, LAL-E1, and

1125 LS1 exhibit a greater surface area abundance of Mg content shown in orange with intermediate

1126 spots of greater Ca identified in light green (**Figures 5-7 in the supplemental materials**). These

1127 results also correspond with the presence of hydromagnesite within LAL-C and LS with a

1128 mixture of hydromagnesite and aragonite in LAL-E deduced from reflectance spectroscopy.

1129 Extensive microscopy was conducted by Burnie et al. (2023) with a focus on the environmental

1130 and mineralogical controls for biosignature preservation using similar analogue site materials.

1131 **5. Discussion**

1132   The use of analogue sites to determine paleo-environmental conditions is advantageous

1133 for the development of hypotheses within Jezero crater. The hydrothermal alteration of the

1134 Jezero crater floor and the formation of Mg-carbonates in the marginal carbonate formation

1135 through precipitation and evaporation processes that may indicate the potential habitability of

1136 Mars. that indicate the potential habitability of Mars. Hydromagnesite and magnesite

1137 microbialites are produced in very few lakes on Earth (e.g., Renaut 1993; Braithwaite and Zedef

1138 1994, 1996; 1996; Russell et al. 1999; Power et al. 2009). Most are precipitated through

1139 evaporation of lakes and groundwaters (Warren, 1998). This study was able to conduct spectral

1140 analyses of Mg-rich microbialites from four terrestrial analogue sites. Environmental conditions

1141 of the sites are identified in **Table 1** and in the introductory section.

1142 **5.1.   Comparison of pure end members to analogue site samples**

1143   The reflectance spectra from the microbialites can be compared to pure carbonate end

1144 member spectra from our lab and the literature (**Figure 4**). Samples ATP, ATM, ATA, CC, and

1145 LAL-E all spectrally deviated from a pure single carbonate member, indicating they are

1146 mixtures. The XRF data from ATP, ATM, ATA, CC and LAL-E1 samples range in Ca content

1147 but all have a high wt.% CaO compared to wt.% MgO leading to Ca-carbonate dominated

1148 spectra. The samples with greater wt.% CaO compared to wt.% MgO have a wide 2.3 µm band

1149 with a center at longer wavelengths than that of aragonite. However, the presence of wt. % MgO

1150 is not completely dominated with the presence of a shorter wavelength center consistent with

1151 magnesite found in ATP, ATM, and ATA. The sample LAL-E is unique, as the whole rock

1152 spectrum resembles hydromagnesite up to 2.2 µm; beyond that, there is a downturn towards

1153 longer wavelengths and an absorption center corresponding to aragonite with a weak longer

1154 wavelength shoulder. Although the unsorted (<1000 µm) and <45 µm particular size samples do

1155 not display the same shape of hydration feature as the whole rock at 1.4 µm, they have a distinct

1156 absorption feature at ~2.33 µm which is consistent with aragonite. Samples ATH, LAL-C, and

1157 LS are consistent with pure hydromagnesite which is consistent with both the XRD and XRF .

1158   The Raman spectra from the microbialites did not exhibit many carbonate-related peaks

1159 similar to the pure end members. The region of the exhibited peaks in the microbialite spectra

1160 ranged from 1077-1112 cm^{-1}. The Raman peaks identified within the microbialite sample ATM2

1161 had some deviation from pure end members from the literature and from our samples, however

1162 slight differences in chemical composition can be attributed to these peak shifts. An aragonite

1163 peak in ATM2 was determined to be at 1077 cm^{-1}, lower than 1082 cm^{-1} and 1084 cm^{-1}

1164 determined within this study and others (i.e., Chakrabarty and Mahapatra, 1999; Alia et al.,

1165 1997). This sample was determined to have a greater wt. % SiO_2 and lower wt. % CaO from the

1166 XRF data compared to the aragonite sample CRB124 (**Table 3**). The ATP samples Raman

1167 spectra were determined to be within the range of pure aragonite (i.e., Chakrabarty and

1168 Mahapatra, 1999; Alia et al., 1997). The LS2 Raman spectra exhibited an 1112 cm^{-1} peak that

1169 deviated from pure hydromagnesite which should be present around ~1117-1120 cm^{-1} (White

1170 1974; Edwards et al., 2005a; Frost, 2011) (**Table 6**), and may be mixed with magnesite (Wang et

1171 al., 2006) due to the high wt. % MgO within the sample.

1172   Our results indicate that through reflectance (VNIR) spectroscopy, the microbialites all

1173   identify as some sort of carbonate(s). This study also observe spectral variations that can be

1174   linked to the types of carbonates. Tarnas et al. (2021) hypothesized carbonate formation in the

1175   Jezero crater region to be attributable to one single mechanism (hydrothermal alteration), due to

1176   the carbonates' VNIR spectral non-uniqueness, morphology, and thickness of the marginal

1177   carbonates and carbonates within Jezero crater to the Regional Olivine Bedrock (ROB) unit.

1178   Tarnas et al. (2021) implied the origin of the ROB to be non-deltaic carbonate-bearing rocks.

1179   They identify the simplest explanation for all carbonates within the Nili Fossae to have formed

1180   through one single mechanism that does not involve lacustrine activity. The use of VNIR

1181   reflectance for carbonate formation and origin is difficult to undertake, no matter the the

1182   formation conditions the spectrum will exhibit the same features with the exception of absorption

1183   bands related to pigments (i.e., chlorophyll). However, VNIR is a known technique in identifying

1184   the species of carbonate (Fe, Mg, Ca, Na) which can help determine bedrock lithologies.

1185   Microbialites found within our study sites could be found as sediments spread out in a similar

1186   thickness with very little morphology. This study proposes that the identification and hypothesis

1187   of potential fluvial lacustrine origin are likely for the Mg-carbonates seen in the Marginal

1188   Carbonate unit as depicted in previous studies (i.e., Horgan et al., 2020; Zastro and Glotch,

1189   2021). As the study had determine the lack of definitive evidence for formation environments

1190   using VNIR spectroscopy, the use of our analogue sites and their regional formation of Mg-

1191   carbonates can help determine a potential lacustrine origin for the Marginal Carbonates. The near

1192   shore Mg-rich microbialites form on the periphery of the lake based analogue sites (Lake Salda

1193   and Lake Alchichica) are good analogue environments to Jezero. On Mars, similar near shore

1194   Mg-carbonate structures are being proposed to have formed potentially not lithified or gone

1195   through extensive erosion and weathering and deposited on the crater margin now as a thick

1196   carbonate deposit.

1197   **6. Applications to Mars**

1198   **6.1. Importance of Rover instruments**

1199   From the results of this study, rover-based spectrometers are useful for determining the

1200   geology and mineralogy of Mg-carbonate bearing targets. Reflectance spectroscopy was the most

1201   effective at identifying biological compounds in the precipitates, and at identifying the

1202 spectroscopic differences between hydromagnesite and magnesite. The reflectance spectra

1203 without the use of XRD and XRF data were ambiguous for the detection of carbonate mineral

1204 mixtures due to the centers being 0.01 µm separation between species. Raman spectroscopy was

1205 more efficient at determining mineralogical differences between carbonate species within the

1206 Atlin bedrock samples and in the precipitates when the high fluorescence allowed for peaks to be

1207 identified. For instance, MER in situ detection of Mg-carbonates indicated the importance of

1208 spectrometers onboard rovers. Geologic units such as Séítah have determined the importance of

1209 in situ spectrometers for detecting carbonate species in higher spatial resolution and confidence

1210 than orbiters mapping the region determining the main mineralogy/geology of the units (Clave et

1211 al., 2022; Stack et al., 2020). From our results, the reflectance and Raman spectroscopies show

1212 the capabilities of identifying carbonates absorption bands and peaks from pure end members to

1213 mixtures. These techniques have observed the *in-situ* presence of carbonates on Mars in Jezero

1214 crater (Clave et al., 2022, Wiens et al., 2022; Mandon et al., 2022) Both the reflectance and

1215 Raman have shown the potential to identify biological compounds such as chlorophyll and

1216 carotenoids. Similar to our study, Garczynski et al., (2021) determined the usefulness of rover

1217 instruments such as SuperCam and Mastcam-Z in identifying Mg-carbonate precipitates from

1218 Lake Salda. Using reflectance spectroscopy similar to the VISIR instrument on the Perseverance

1219 rover can allow for the detection of Mg-carbonates at various distances.

6.2.   Spectroscopic determination of olivine and magnesite versus listvenite

1221   Our spectral results can aid in determining differences between iron-rich (6-9 wt. % FeO)

1222 listvenite and Fe-Mg olivine absorption bands. Certain interpretations of olivine from the

1223 Perseverance rover may be due to a large amount of iron (Fe) within the sample, creating a

1224 downturn towards 1 micron and an upturn from 0.8 to lower wavelengths, as seen in the Anna

1225 and Pictou mine samples (**Figure 12**). Due to the SuperCam VISIR covering the spectral region

1226 between 0.4-0.85 and 1.3-2.6 µm wavelength ranges (Wiens et al., 2022) the shape of the

1227 absorption feature for olivine and iron-rich magnesite is covered which would be a key indicator

1228 of mineralogy. Specifically, Fe-bearing magnesite has a doublet absorption feature with bands

1229 near 1.0 and 1.2 µm, while olivine has an absorption triplet in this region, with overlapping

1230 absorption bands near 0.85, 1,05, and 1.25 µm (King and Ridley, 1987).

1231   The Jezero crater VISIR data from the target Penne sol 211 #5 taken from the Séítah unit

1232   and the listvenite reflectance spectra (Figure 9) exhibit similarities with a deep Fe-related

1233   absorption from 0.7 to ~1.6 µm, a 1.9 µm OH/ H_2O feature and a 2.31 µm magnesite absorption

1234   band (Wiens et al., 2022). The Penne spectrum was determined to be consistent with olivine

1235   however, it is also very similar to the listvenite spectrum. Since listvenite can derive from an

1236   olivine-rich precursor, LIBS data would not show marked differences from olivine. The broad

1237   olivine feature may be missing or masking the doublet created by Fe in the listvenite spectrum.

1238   In the Atlin bedrock listvenites no olivine is present due to the completed alteration. The depth of

1239   the 2.31 µm absorption in the Penne target is less than the listvenite magnesite band, which could

1240   be attributed to the lower carbonate content at that raster point, illumination condition, grain size,

1241   or surface roughness (Clave et al., 2022).

1242   **6.3.   Atlin bedrock analogue to the Séítah formation**

1243   The Atlin region consists of serpentinized, carbonatized, and deformed harzburgite with

1244   minor dunite and pyroxenite veins. The northwest British Columbia region has undergone

1245   volcanism and hydrothermal activity similar to several mechanisms hypothesized within Jezero

1246   crater. This analogue site can provide important insights for Mars astrobiology and the formation

1247   of Mg-carbonate deposits. The Mg-carbonates from this region are formed through groundwater

1248   discharge and evaporation.

1249   The ultramafic Séítah formation is elevated in Mg compared to the Máaz, Content, and

1250   Artuby formations (Wiens et al., 2023). Within the Séítah unit, LIBS has detected carbonates

1251   within the Garde_209b abrasion patch which has been suggested to be Fe-Mg carbonates (with a

1252   silicate phase) with 3-4 wt. % CaO, indicating the presence of calcium within the carbonates.

1253   The Atlin listvenite bedrock samples are compositionally similar in terms of a number of

1254   elemental wt.% using XRF techniques. In the averaged Séítah LIBS targets from sols 202-286

1255 SiO_2 content was 45.1 wt. %, MgO content was 21.4 wt.%, and CaO content was 3.8 wt. %

1256   (Wiens et al., 2022). The listvenite samples 16AT-PI-1 and 16AT-PI-2 have 48.01 and 50.88 wt.

1257   % SiO_2 content respectively, 39.12 and 37.13 wt. % MgO content respectively, and, 2.86 and

1258   1.22 wt. % CaO content, respectively (**Table 4**). A higher wt. % FeO is seen in the Séítah (23.0

1259   wt. %) formation rocks (listvenite FeO between 1.23-3.24 wt. %). We propose that the Séítah

1260   formation is similar to our listvenite bedrock at a different alteration stage and due to the

1261   additional oxidation of the Martian surface, this has lowered wt. % MgO and increased the wt. %

1262   Fe totals in the detections on Mars. The data collected by the Perseverance Rover allows the

1263   interpretation of a potentially less altered bedrock to our listvenite samples.

1264   The Séítah formation has been assumed to be related to the olivine-carbonate lithologies

1265   present inside and outside of Jezero crater. The olivine-carbonate lithologies have been

1266   previously speculated to be due to serpentinization (Brown et al., 2010). Brown et al. (2022)

1267   determined LIBS and VISIR spectral signatures most consistent with talc over serpentine in the

1268   Séítah Dourbes tailings and the Garde abrasion patch. The presence of talc and olivine within the

1269   Séítah formation bedrock has implications for the alteration history, determining the extent of

1270   interactions with hydrothermal fluids (Brown et al., 2022; Mandon et al., 2022; Clave et al.,

1271   2022). From the listvenite reaction suite outlined by Hansen et al. (2015), the Séítah formation

1272   would have undergone the early stages of R_1 alteration, however, it has not gone to completion,

1273   as the olivine crystals are still present within the ultramafic bedrock.

1274   From these data, we can posit that the rocks found in Jezero crater have gone through

1275   alteration processes that may be similar to the listvenite bedrock found around the Atlin playas.

1276   The most plausible mechanism of Jezero crater bedrock based on the spectroscopic results is

1277   fluvial hydrothermal interactions with the lake bottom or with low water rock interactions

1278   through groundwater processes. The regional rocks surrounding the Atlin playa indicate low-

1279   temperature carbonation of mafic minerals producing magnesite-rich deposits (Hansen et al.,

1280   2005), resulting in the supersaturation of carbonate ions within the groundwater precipitating as

1281   carbonates, and in the case of Atlin playas, as microbial-hosting mats (Power et al., 2009).

1282   The formation of carbonates within the ROB is posited by Tarnas et al. (2020) to

1283   potentially have formed through the later alteration of the olivine-bearing rocks by water-rock

1284   interactions under a variety of temperatures similar to those that form listvenite deposits

1285   (Beinlich et al., 2020; Falk and Kelemen 2015). The lack of presence of alteration minerals such

1286   as serpentines suggests a time-limited interaction, low water rock ratios, or ambient fluid

1287   temperatures during carbonation (Scheller et al., 2022). Van Berk and Fu (2011) proposed that

1288   serpentinization or carbonation occurred more fully at the top of the mottled terrain unit.

1289   The four analogue sites determine that even with different conditions and weathering

1290   processes experienced by the bedrock, Mg-rich carbonate microbialites are forming in similar

1291   ways in these different site environments. Farley et al. (2022) also hypothesized in situ

1292   carbonation of olivine within the Séítah formation. This provides a rationale for the usefulness of

1293   the unique formation of Mg-carbonates from fine-grained ultramafic bedrock at Clinton Creek.

1294   The Clinton Creek bedrock was serpentinized to chrysotile and antigorite from serpentine,

1295   harzburgite, lherzolite, dunite, and pyroxenite. Clinton Creek is a useful analogue site as it is

1296   predominantly serpentine minerals in terms of geological bedrock and we see continued growth

1297   of microbialites in the mine pits. This may indicate that the bedrock could have undergone

1298   different reaction mechanisms from the precursor olivine to form serpentines to then react to

1299   produce potential Mg-carbonates microbialites. This proves the usefulness of multiple analogue

1300   sites with similarities to relate to Mars spectral data and other locations where Mg-carbonates are

1301   identified.

1302   **6.4.   Implications for carbonates in Jezero crater**

1303   The analogues sites used in this study have similarities to Jezero crater in terms of their

1304   geology, low temperature, and basin systems. The analogue sites represent closed basin systems

1305   (e.g., Atlin playas, Clinton Creek, Lake Alchichica) as well as open basin systems with inflow

1306   and outflow channels (e.g., Lake Salda). The following discussion highlights a playa system

1307   hypothesis for the carbonates within the Séítah unit and the major hypothesis from Horgan et al.,

1308   (2020) for the formation of Mg-carbonates in the Marginal Carbonate unit. From the previous

1309   discussion, we posit the formation of carbonates due to the interaction of mafic and ultramafic

1310   precursors supersaturating the ancient lake within Jezero crater, depositing Mg-rich (and

1311   plausibly microbialites) carbonates in the ancient lake littoral zone and within near-shore

1312   environments during a habitable Mars.

1313   The identification of Atlin bedrock being closely related to the Jezero crater Séítah

1314   formation indicates the possibility of the formation of Mg-carbonate microbialites within the

1315   crater floor as mound deposits, coatings, or weathered and reworked deposits. The hypothesis of

1316   a potential playa system for the Light-toned-Floor unit (Horgan et al., 2015) provides evidence

1317   for the Atlin playas as a valid analogue site. The Jezero paleolake is thought to have become a

1318   closed basin as the planet-wide water budget declined (Clifford and Parker 2001), in which a

1319   playa-like environment may have formed the light-toned floor of the crater (Salese et al. 2019).

1320   Goudge et al. (2015) determined the Mg-carbonates within the Light-toned Floor unit Cf-fr and

1321 Cf-f1 now Séítah to be poorly lithified and friable. Similarly, Power et al. (2009) identified the

1322 Mg-rich carbonates of the Atlin playas to produce hydrated magnesite-hydromagnesite mats that

1323 are ~2 cm thick, are non-lithified, non-laminated, and have no sedimentary structures. The low

1324 water-rock interactions that altered parts of the Séítah bedrock could have pooled in topographic

1325 lows rich in dissolved solutes within the unit producing thin Mg-rich carbonate mats poor at

1326 entombing microbial biomass through evaporative processes (Burnie et al., 2023). The formation

1327 of these mats could have been physically altered within the crater by erosional and aeolian

1328 processes due to their fine-grained fragile nature causing the mats to be unidentifiable.

1329   Based on our results there are similarities between our microbialites hydrated magnesite

1330 mixtures and hydromagnesite spectra addressed by Horgan et al. (2020) considered to be

1331 authigenic hydrated magnesite and hydromagnesite. Observational data have determined that the

1332 Jezero carbonates are consistent with a mixture of magnesite or hydromagnesite with some Ca-

1333 substitutions in variable abundances (Horgan et al., 2020). Our results and the observational data

1334 demonstrate the compatibility of our microbialite mixtures of Mg and Ca carbonates forming

1335 from the four analogue sites. Zastro and Glotch, (2022) additionally note the differences between

1336 the Marginal Carbonates and the Mottled Terrain unit from the strength and ratio of the 2.3 and

1337 2.5 µm absorption bands and changing carbonate mineralogy which likely corresponds to

1338 differences in their formation processes and environments. Given the change from Fe-rich

1339 carbonates (siderite) in the Mottled terrain to Mg-rich carbonates (magnesite), the lack of olivine

1340 and serpentine within the marginal carbonates indicates a potential for further carbonation or

1341 serpentinization. The carbonates forming within the olivine enriched and olivine carbonates units

1342 are most likely low temperature, in situ carbonation (van Berk and Fu, 2011), or in place

1343 serpentinization reactions. Both Zastro and Glotch (2021) and Horgan et al., (2020) consider the

1344 possibility of the formation of Mg-carbonates from fluvial/lakeside authigenic precipitation.

1345   Due to Jezero crater containing evidence of a past lake (Mangold et al., 2021), the

1346 formation of carbonates through evaporation at relatively low temperatures (Ruff et al., 2014)

1347 should be addressed. Lakes can evolve from a saline state to become alkaline in basaltic

1348 environments, which can lead to the precipitation of carbonates and the potential formation of

1349 the Marginal Carbonates' unit (Horgan et al., 2020).

1350   The fluvial-lacustrine hypothesis fits well within the Lake Salda and Lake Alchichica

1351   analogue sites as they precipitate and form within a certain range in depths consistent with the

1352   elevation range of ~140m of the marginal carbonate (Horgan et al., 2020). The hydrothermal

1353   weathering of the bedrock could have saturated the lake waters and deposited microbially

1354   influenced shoreline precipitates through evaporative processes. The lake experienced a closed

1355   basin during its early stages of development likely the stage of microbialite formation due to the

1356   high dissolved solutes producing high alkaline environments for carbonate precipitation.

1357   Garczynski et al. (2021) determined that if Mg-carbonates are found to be authigenic they

1358   are likely to be fine-grained mixed with or layered with detrital muds or overgrowths of

1359   carbonates. The rover may encounter detrital cobbles, carbonate grains broken up by water

1360   action, potential microcrystalline crystals, and layering determining primary precipitation

1361   (Garczynski et al., 2021). In-situ analysis and sample return collection of the Marginal

1362   Carbonates will be essential to understand the formation mechanisms of the carbonates in this

1363   unit.

6.5.   Carbonate insight for Mars climate

1365   Carbonates on Mars may be a significant carbon sink (Teir et al., 2009; Zent and Quinn,

1366   1995) and may identify past atmospheric conditions. The carbon loss from the atmosphere may

1367   be held within the carbonates and regolith, which may have impacted the Martian climate

1368   (Jakosky et al., 2018; Lammer et al., 2013). Understanding the abundance of carbonates on the

1369   surface is critical in determining the carbon budget on Mars. It is known that carbonates that

1370   have formed at low temperatures often exhibit distinctive isotope signatures (Beinlich et al.,

1371   2012). These signatures may be used to decipher the formation mechanisms, fingerprint the

1372   carbon source, or infer paleoclimatic conditions (Beinlich et al., 2012).

1373   The reaction of low-temperature (50 °C) high-CO_2 aqueous solutions with the presence of

1374   olivine and H_2O films produces stable magnesite (Wood et al., 2019). The carbonation process

1375   produces magnesite and talc that binds large amounts of CO_2 (Teir et al., 2009). The carbonation

1376   reactions producing magnesite and quartz may be limited due to the inability of the bedrock to

1377   increase in volume associated with this phase of the reaction, thus potentially limiting the

1378   sequestration capacity by destroying the porosity and permeability. The Martian bedrock may

1379   have undergone preliminary reactions to produce limited amounts of magnesite and talc as seen

1380   by the *in-situ* data, binding CO_2 from the atmosphere. However, the bedrock could have not been

1381   capable of expansion for accommodating an additional volume of products (Hansen et al., 2005).

1382   The Atlin region is characterized by its current role as a CO_2 sequestration site that has

1383   been stable over thousands of years (Power et al., 2009). Hansen et al., 2005 also determined a

1384 CO_2-rich aqueous fluid is the most favorable water chemistry for the reactions R_1 and R_2

1385   producing alteration products and storing carbon which may have occurred 168-172 Ma ago in

1386   the Atlin region. Similar to the Atlin region the variability of groundwater percolation and space

1387   within fractures of the Atlin bedrock may have produced the spatial variability of carbonate

1388   outcrops on Mars.

1389   The study proposes that some of the CO_2 from a wetter and more habitable Mars

1390   (Noachinan and Hesperian) has been stored within carbonates due to CO_2 sequestration. This is

1391   not a new hypothesis as Tomkinson et al. (2013) and Edwards and Ehlmann (2015) have

1392   hypothesized the sequestration of Martian CO_2 by mineral carbonation. A maximum of ~20%

1393   carbonate of the Nili Fossae bedrock is composed of carbonate based on the HiRISE and CRISM

1394   orbital coupling data. These low abundances of carbonate detections may be due to the detection

1395   limits of carbonates needing to be greater than ~10 wt. % with fine grained materials to be

1396   detectable in VISIR spectra using the 2.3 and 2.5 µm absorptions features (Applin et al., 2023).

1397   The lack of carbonates identified on the Martian surface compared to the modeled amount of

1398 CO_2 in the atmosphere suggested sustaining surface waters and habitability during the Noachian

1399   and Hesperian could additionally be explained by hidden rock deposits that remain to be

1400   discovered.

1401   **6.6.   Lack of aragonite detections on Mars**

1402   The SEM results from LAL-C1 and LAL-E1 indicate a mixture of Ca-rich and Mg-rich

1403   carbonates determined as aragonite and hydromagnesite respectively. Kaźmierczak et al., (2011)

1404   has determined the diagenetic replacement of aragonite to hydromagnesite. From our results, the

1405   replacement processes cannot be documented as the samples all exhibit similar porous textures.

1406   Mineral mixtures are similar within the Alchichica samples with Ca-rich regions being

1407   predominantly in the interior or the pores or coating the outer regions. These are reversed for the

1408   Atlin samples which have Mg-rich regions predominantly in the interior or the pores or coating

1409   the outer regions. Alchichica's white microbialites are very similar to the Holocene stromatolites

1410 from the alkaline Lake Walyngup in Western Australia (Coshell et al., 1998). Both regions have

1411 aragonite being replaced by hydromagnesite (Kaźmierczak et al., 2011). Ca-rich aragonite is

1412 precipitated in the living cyanobacteria mat which transitions downwards into hydromagnesite

1413 replacing the diagenetic primary aragonite (Kaźmierczak et al., 2011). This process is poorly

1414 understood and needs to be studied to understand the mechanisms of mineral replacement.

1415   No spectral identifications of aragonite have occurred to date from orbiters or *in situ*

1416 detections. This study determined that if aragonite where to be found in a mixture with Mg-

1417 carbonates the shape of the absorption bands will changes from pure end members. The

1418 absorption feature will have a shoulder and downturned slope towards longer wavelengths with a

1419 minimum ~2.31-2.33 µm as mixtures. Some mixtures will be characterized as having two

1420 superimposed absorption bands similar to pure aragonite with another band minima present

1421 ~2.34 µm, unlike pure magnesite which has a shoulder towards longer wavelengths with a

1422 minima at 2.3-2.31 µm.

1423   Based on the findings from Kaźmierczak et al. (2011), the microbialites - in the form of

1424 precipitated aragonite, the metastable Ca-rich carbonate - could have been replaced with more

1425 stable mineral forms such as magnesite based on known Earth occurrences (i.e., Lake

1426 Alchichica, Lake Walyngup, etc.). Additionally, aragonite could also be present in Jezero crater

1427 at a spatial resolution below that of orbiter detection limits (Hays et al. 2017) or is present in

1428 areas and targets not examined by the Perseverance rover to date.

1429   Kaźmierczak et al. (2011) identified that the aragonite found at Lake Alchichica is usually

1430 microlaminated, while the hydromagnesite is structureless and the identification of cyanobacteria

1431 remains is extremely rare in the "white" microbialites as also documented in Burnie et al.,

1432 (2023). Burnie et al. (2023) determined Mg-carbonates as poor preservation mediums over Ca-

1433 carbonates due to their subaerial formation under evaporative conditions, slow formation rates,

1434 and their tendencies to not lithify. This has implications for mineralogical detections as Ca-

1435 carbonates such as aragonite have yet to be spectrally identified. However, if found in the same

1436 environment as Mg-carbonates, Ca-carbonates may point to a past fluvial-lacustrine environment

1437 and may hold evidence of biosignatures due to their greater ability to entomb microbial biomass.

1438 **6.7.   Mg-rich microbialites biosignature detections**

1439   This study is directly linked to that of Burnie et al. 2023 as they have characterized the

1440 same samples used in this study to determine the preservation potential of biosignatures within

1441 minerals found in the microbialite such as aragonite and mg-carbonates. Further description of

1442 the biosignature potential can be found in their study. Our study examined the Mars

1443 spectroscopic instrument potential to characterize the microbialites to use to determine Mars

1444 habitability and potential astrobiological targets for sample return purposes.

1445   One of the main preconditions for microbialite formation for the analogue sites are the

1446 alkaline hydrochemistry linked to a high supersaturation and precipitation of carbonates, leading

1447 to the growth of biogenic structures (i.e., microbialites) (Kaźmierczak et al., 2011). This offers a

1448 positive test for the hypothesis of the early soda ocean on Mars for the formation of Mg-

1449 carbonate microbialites in these alkaline environments (Kempe and Kazmierczak, 1997). Mars

1450 could have produced microbialites from the interaction of microbes and the precipitation of

1451 carbonates within and on the shores from the supersaturated water bodies. The possibility of

1452 these microbialites retaining their macrostructure is unlikely due to the increased exposure to

1453 harsh Martian conditions such as UV irradiation, dehydration, erosion, and weathering.

1454 Microbial mats associated with Mg-carbonate mineralogy have a low preservation potential

1455 regarding forming and fossilizing a sedimentary structure (i.e., microbialite) on Earth (Renaut,

1456 1993; Burnie et al., 2023). Poor preservation factors include desiccation, cryogranulation,

1457 interstitial carbonate precipitation, recrystallization, bioturbation, compaction, and erosion

1458 (Renaut, 1993) all of which could be facilitated on the current Martian surface. The

1459 microbialite's texture and formation may not have been preserved on the surface of Mars;

1460 therefore, the presence of hydrated Mg-carbonates could be the only way to infer biogenicity.

1461   The SEM was used to identify the textures and mixture of Mg and Ca-rich carbonate

1462 intergrowths, which can be evidence for the formation of microbialites in similar conditions to

1463 our analogue sites. Due to Jezero crater having similar formation conditions to the low-

1464 temperature microbially-influenced carbonate precipitates of the analogue sites, similar deposits

1465 could have formed on Mars and be detectable using spectroscopic instruments on the rover. The

1466 Perseverance rover will be able to acquire carbonate species-specific spectral data for the

1467 carbonate-bearing units.

1468   From our results discussed in an above section 5.1, Mg-carbonate microbialites are not

1469   distinguishable spectrally from others formed through non-biogenic processes. The only

1470   potential distinguishing factor through VISIR spectroscopy is the chlorophyll absorption bands

1471   centered at 0.67 µm, but which are not identified in all microbialite samples. A previous study

1472   conducted by Stromberg et al., (2014) identified the stability of chlorophyll absorption for

1473   several months in a Mars surface environment chamber. However, the stability is not known for

1474   longer time frames. The high-resolution instruments onboard the Perseverance rover such as

1475   Pixel, Sherlock, and Watson with their known capabilities to be able to detect formations and

1476   textures of microbialites (i.e., stromatolites). In addition to the in-situ instruments that may aid in

1477   determining a potential microbialite is to identify and search for carbonates due to their high

1478   biosignature potential and to return them to Earth for further biosignature identification. Sample

1479   return will provide a unique opportunity to observe and analyze carbonate samples from Mars to

1480   determine past environmental conditions and search for signs of past or present life.

7. Conclusions

1481

1482   The Mg-carbonate microbialite and bedrock geology from the Atlin playas, Clinton

1483   Creek, Lake Salda, and Lake Alchichica serve as important analogue sites. The formation of Mg-

1484   rich biogenic carbonates in low-temperature ultramafic and mafic environments are similar to

1485   those at Jezero crater. The results agree with the hypothesis of fluvial-lacustrine authigenic

1486   carbonates within the Jezero crater Marginal Carbonates unit. The analogue sites can provide

1487   insight into the formation conditions of carbonates on Mars to infer their formation in the paleo-

1488   lacustrine environments found in Jezero crater. Specifically, the low-temperature alkaline

1489   aqueous environment with influences from the ultramafic and mafic bedrock weathering. It can

1490   also provide insight into depositional processes associated with other occurrences of carbonates

1491   on Mars such as formation through precipitation in water-rich environments, deposition and

1492   evaporation processes in playa environments, or scenarios of formation through weathering

1493   processes.

1494   Mg-carbonate microbialites are not distinguishable spectrally from others formed through

1495   non-biogenic processes. This indicates that the best way to determine a potential microbialite is

1496   to search for carbonates due to their high biosignature potential and to return them to Earth for

1497   further biosignature identification. In-situ analysis and Mars sample return of the carbonates and

1498 bedrock floor will be essential to understand the formation mechanisms of the carbonates within
1499 Jezero crater. Mars sample return will increase our understanding of past environmental
1500 conditions and determine the potential of life within carbonate samples. Although, reflectance
1501 and Raman spectroscopy are able to determine chlorophyll and carotenoid related spectral
1502 features.

1503   To build upon this study the C-TAPE Lab plans to exposure the microbialite precipitates to
1504 Mars-like surface conditions to determine any spectral changes. Additionally, analysis of the
1505 weathering processes of the Atlin bedrock will be undertaken using several alteration stages of
1506 bedrock found in the area. This will be done to determine the likelihood of which reaction stage
1507 the Séítah bedrock may have undergone.

9. References

1518 1.   Alcocer, J., Merino-Ibarra, M., Ramírez-Zierold, J.A., Oseguera, L.A., Cortés-Guzmán, D.,
1519   Castillo-Sandoval, F.S., Guzmán-Arias, A.P. and Pérez-Ramírez, M.G., 2021. Lake Alchichica
1520   limnology. *Lake Alchichica Limnology. The Uniqueness of a Tropical Maar Lake; Springer*
1521   *Nature: Berlin/Heidelberg, Germany*, p.491.
1522 2.   Alcocer, J. and Hammer, U.T., 1998. Saline lake ecosystems of Mexico. *Aquatic Ecosystem*
1523   *Health & Management*, *1*(3-4), pp.291-315.
1524 3.   Alia, J.M., De Mera, Y.D., Edwards, H.G.M., Martín, P.G. and Andrés, S.L., 1997. FT-Raman
1525   and infrared spectroscopic study of aragonite-strontianite (CaxSr1− xCO3) solid
1526   solution. *Spectrochimica Acta Part A: Molecular and Biomolecular Spectroscopy*, *53*(13),
1527   pp.2347-2362.

1528   4.   Allwood, A.C., Wade, L.A., Foote, M.C., Elam, W.T., Hurowitz, J.A., Battel, S., Dawson, D.E.,
1529   Denise, R.W., Ek, E.M., Gilbert, M.S. and King, M.E., 2020. PIXL: Planetary instrument for X-
1530   ray lithochemistry. *Space Science Reviews*, *216*(8), pp.1-132.

1531   5.   Altermann, W. and Kazmierczak, J., 2003. Archean microfossils: a reappraisal of early life on
1532   Earth. *Research in Microbiology*, *154*(9), pp.611-617.

1533   6.   Altermann, W., Kazmierczak, J., Oren, A. and Wright, D.T., 2006. Cyanobacterial calcification
1534   and its rock-building potential during 3.5 billion years of Earth history. *Geobiology*, *4*(3), pp.147-
1535   166.

1536   7.   Andrew, K., 1985. Fluid inclusion and chemical studies of gold-quartz veins in the Atlin Camp,
1537   Northwestern British Columbia. *Unpublished B. Sc. Thesis, The University qf British Columbia,*
1538   *I*.

1539   8.   Armienta, M.A., Vilaclara, G., De la Cruz-Reyna, S., Ramos, S., Ceniceros, N., Cruz, O.,
1540   Aguayo, A. and Arcega-Cabrera, F., 2008. Water chemistry of lakes related to active and inactive
1541   Mexican volcanoes. *Journal of Volcanology and Geothermal Research*, *178*(2), pp.249-258.

1542   9.   Ash, C.H. (1994) Origin and tectonic setting of ophiolitic ultramafic and related rocks in the Atlin
1543   area, British Columbia (NTS 104N). B.C. Ministry of Energy, Mines and Petroleum Resources,
1544   Bull. 94.

1545   10.   Ash, C.H. Relationship between ophiolites and gold– quartz veins in the North American
1546   Cordillera. B.C. Dep. of Energy, Mines and Petroleum Resources, Bull. 108.

1547   11.   Balci, N., Gunes, Y., Kaiser, J., On, S.A., Eris, K., Garczynski, B. and Horgan, B.H., 2020. Biotic
1548   and abiotic imprints on Mg-rich stromatolites: Lessons from lake Salda, SW
1549   Turkey. *Geomicrobiology Journal*, *37*(5), pp.401-425.

1550   12.   Bea, S.A., Wilson, S.A., Mayer, K.U., Dipple, G.M., Power, I.M. and Gamazo, P., 2012. Reactive
1551   transport modeling of natural carbon sequestration in ultramafic mine tailings. *Vadose Zone*
1552   *Journal*, *11*(2).

1553   13.   Beegle, L., Bhartia, R., White, M., DeFlores, L., Abbey, W., Wu, Y.H., Cameron, B., Moore, J.,
1554   Fries, M., Burton, A. and Edgett, K.S., 2015, March. SHERLOC: scanning habitable
1555   environments with Raman & luminescence for organics & chemicals. In *2015 IEEE aerospace*
1556   *conference* (pp. 1-11). IEEE.

1557   14.   Beinlich, A. and Austrheim, H., 2012. In situ sequestration of atmospheric CO2 at low
1558   temperature and surface cracking of serpentinized peridotite in mine shafts. Chemical Geology,
1559   332, pp.32-44.

1560   15.   Beinlich, A., Plümper, O., Hövelmann, J., Austrheim, H. and Jamtveit, B., 2012. Massive
1561   serpentinite carbonation at Linnajavri, N–Norway. *Terra Nova*, *24*(6), pp.446-455.

1562   16.   Beinlich, A., Plümper, O., Boter, E., Müller, I.A., Kourim, F., Ziegler, M., Harigane, Y., Lafay,
1563   R., Kelemen, P.B. and Oman Drilling Project Science Team, 2020. Ultramafic rock carbonation:
1564   Constraints from listvenite core BT1B, Oman Drilling Project. *Journal of Geophysical Research:*
1565   *Solid Earth*, *125*(6), p.e2019JB019060.

1566   17.   Bell, J.F., Maki, J.N., Mehall, G.L., Ravine, M.A., Caplinger, M.A., Bailey, Z.J., Kinch, K.M.,
1567   Madsen, M.B., Betts, B., Cisneros, E. and Ehlmann, B.L., 2020, March. The mars 2020 rover
1568   mast camera zoom (mastcam-z) multispectral, stereoscopic imaging investigation. In *51st Annual*
1569   *Lunar and Planetary Science Conference* (No. 2326, p. 1305).

1570   18.   Bell, J.F., Maki, J.N., Mehall, G.L., Ravine, M.A., Caplinger, M.A., Bailey, Z.J., Brylow, S.,
1571   Schaffner, J.A., Kinch, K.M., Madsen, M.B. and Winhold, A., 2021. The Mars 2020 perseverance
1572   rover mast camera zoom (Mastcam-Z) multispectral, stereoscopic imaging investigation. *Space*
1573   *science reviews*, *217*(1), pp.1-40.

1574   19.   Benzerara, K., Skouri-Panet, F., Li, J., Férard, C., Gugger, M., Laurent, T., Couradeau, E., Ragon,
1575   M., Cosmidis, J., Menguy, N. and Margaret-Oliver, I., 2014. Intracellular Ca-carbonate
1576   biomineralization is widespread in cyanobacteria. *Proceedings of the National Academy of*
1577   *Sciences*, *111*(30), pp.10933-10938.

1578   20.   Berg, B.L., Ronholm, J., Applin, D.M., Mann, P., Izawa, M., Cloutis, E.A. and Whyte, L.G.,
1579   2014. Spectral features of biogenic calcium carbonates and implications for
1580   astrobiology. *International Journal of Astrobiology*, *13*(4), pp.353-365.

1581   21.   Beyssac O. et al. (sub., manuscript #2022JE007638) 2022. Petrological traverse of an olivine
1582   pyroxene cumulate on the floor of Jezero Crater, Mars: a perspective from SuperCam onboard
1583   Perseverance, *JGR*.

1584   22.   Bishop, J.L., Schelble, R.T., McKay, C.P., Brown, A.J. and Perry, K.A., 2011. Carbonate rocks in
1585   the Mojave Desert as an analogue for Martian carbonates. *International Journal of*
1586   *Astrobiology*, *10*(4), pp.349-358.

1587   23.   Bishop, J.L., Perry, K.A., Darby Dyar, M., Bristow, T.F., Blake, D.F., Brown, A.J. and Peel, S.E.,
1588   2013. Coordinated spectral and XRD analyses of magnesite-nontronite-forsterite mixtures and
1589   implications for carbonates on Mars. *Journal of Geophysical Research: Planets*, *118*(4), pp.635-
1590   650.

1591   24.   Blaney, D.L. and McCord, T.B., 1989. An observational search for carbonates on Mars. *Journal*
1592   *of Geophysical Research: Solid Earth*, *94*(B8), pp.10159-10166.

1593   25.   Bosak, T., 2022. Aqueously altered igneous rocks sampled on the floor of Jezero crater, Mars.

1594   26.   Braithwaite, C.J.R. and Zedef, V., 1994. Living hydromagnesite stromatolites from
1595   Turkey. *Sedimentary Geology*, *92*(1-2), pp.1-5. https://doi.org/10.1016/0037-0738(94)90051-5.

27. Braithwaite, C.J.R. and Zedef, V., 1996. Hydromagnesite stromatolites and sediments in an alkaline lake, Salda Golu, Turkey. *Journal of Sedimentary Research*, *66*(5), pp.991-1002.

28. Bramble, M.S., Mustard, J.F. and Salvatore, M.R., 2017. The geological history of northeast Syrtis Major, Mars. *Icarus*, *293*, pp.66-93.

29. Brown, A.J., Hook, S.J., Baldridge, A.M., Crowley, J.K., Bridges, N.T., Thomson, B.J., Marion, G.M., de Souza Filho, C.R. and Bishop, J.L., 2010. Hydrothermal formation of clay-carbonate alteration assemblages in the Nili Fossae region of Mars. *Earth and Planetary Science Letters*, *297*(1-2), pp.174-182.

30. Buick, R., Dunlop, J.S.R. and Groves, D.I., 1981. Stromatolite recognition in ancient rocks: an appraisal of irregularly laminated structures in an Early Archaean chert-barite unit from North Pole, Western Australia. *Alcheringa*, *5*(3), pp.161-181.

31. Burne, R.V. and Moore, L.S., 1987. Microbialites: organosedimentary deposits of benthic microbial communities. *Palaios*, pp.241-254.

32. Burnie, T., Power, I., Paulo, C., Alcicek, H., Falcon, L., Lin, Y., and Wilson, S., 2023. Environmental and Mineralogical controls on biosignature preservation in magnesium carbonate systems analogous to Jezero Crater, Mars. Astrobiology.

33. Burns, R.G. and Fisher, D.S., 1990. Iron-sulfur mineralogy of Mars: Magmatic evolution and chemical weathering products. *Journal of Geophysical Research: Solid Earth*, *95*(B9), pp.14415-14421.

34. Caballero, M., Vilaclara, G., Rodríguez, A. and Juárez, D., 2003. Short-term climatic change in lake sediments from lake Alchichica, Oriental, Mexico. *Geofísica Internacional*, *42*(3), pp.529-537.

35. Cabrol, N.A. and Grin, E.A., 1999. Distribution, classification, and ages of Martian impact crater lakes. *Icarus, 142*(1), pp.160-172.

36. Calvin, W.M., King, T.V. and Clark, R.N., 1994. Hydrous carbonates on Mars?: Evidence from Mariner 6/7 infrared spectrometer and ground-based telescopic spectra. *Journal of Geophysical Research: Planets*, *99*(E7), pp.14659-14675. https://doi.org/10.1029/94JE01090

37. Canaveras, J.C., Hoyos, M., Sanchez-Moral, S., Sanz-Rubio, E., Bedoya, J., Soler, V., Groth, I., Schumann, P., Laiz, L., Gonzalez, I. and Saiz-Jimenez, C., 1999. Microbial communities associated with hydromagnesite and needle-fiber aragonite deposits in a karstic cave (Altamira, Northern Spain). *Geomicrobiology Journal*, *16*(1), pp.9-25. https://doi.org/10.1080/ 014904599270712.

38. Carrasco-Núñez, G. and Chako-Tchamabé, B., 2022. Geological Evolution of the Alchichica Crater. In *Lake Alchichica Limnology* (pp. 15-32). Springer, Cham.

1630   39.   Carter, J. and Poulet, F., 2012. Orbital identification of clays and carbonates in Gusev
1631   crater. *Icarus*, *219*(1), pp.250-253.
1632   40.   Catling, D.C., 1999. A chemical model for evaporites on early Mars: Possible sedimentary tracers
1633   of the early climate and implications for exploration. *Journal of Geophysical Research:*
1634   *Planets*, *104*(E7), pp.16453-16469.
1635   41.   Chako-Tchamabé, B.C., Carrasco-Núñez, G., Miggins, D.P. and Németh, K., 2020. Late
1636   Pleistocene to Holocene activity of Alchichica Maar volcano, eastern trans-Mexican volcanic
1637   belt. *Journal of South American Earth Sciences*, *97*, p.102404.
1638   42.   Chakrabarty, D. and Mahapatra, S., 1999. Aragonite crystals with unconventional
1639   morphologies. *Journal of Materials Chemistry*, *9*(11), pp.2953-2957.
1640   43.   Clave, E., Benzerara, K., Meslin, P.Y., Forni, O., Royer, C., Mandon, L., Beck, P., Quantin-
1641   Nataf, C., Beyssac, O., Cousin, A. and Bousquet, B., 2022. Carbonate detection with SuperCam
1642   in igneous rocks on the floor of Jezero Crater, Mars. *Journal of Geophysical Research: Planets*,
1643   p.e2022JE007463.
1644   44.   Cloutis, E.A., Craig, M.A., Kruzelecky, R.V., Jamroz, W.R., Scott, A., Hawthorne, F.C. and
1645   Mertzman, S.A., 2008. Spectral reflectance properties of minerals exposed to simulated Mars
1646   surface conditions. *Icarus, 195*(1), pp.140-168.
1647   45.   Couradeau, E., Benzerara, K., Moreira, D., Gerard, E., Kaźmierczak, J., Tavera, R. and López-
1648   García, P., 2011. Prokaryotic and eukaryotic community structure in field and cultured
1649   microbialites from the alkaline Lake Alchichica (Mexico). *PloS one*, *6*(12), p.e28767.
1650   46.   Coshell, L., Rosen, M.R. and McNamara, K.J., 1998. Hydromagnesite replacement of
1651   biomineralized aragonite in a new location of Holocene stromatolites, Lake Walyungup, Western
1652   Australia. *Sedimentology*, *45*(6), pp.1005-1018.
1653   47.   Das, B., Vinebrooke, R.D., Sanchez-Azofeifa, A., Rivard, B. and Wolfe, A.P., 2005. Inferring
1654   sedimentary chlorophyll concentrations with reflectance spectroscopy: a novel approach to
1655   reconstructing historical changes in the trophic status of mountain lakes. *Canadian Journal of*
1656   *Fisheries and Aquatic Sciences*, *62*(5), pp.1067-1078.
1657   48.   de Oliveira, V.E., Miranda, M.A.N., Soares, M.C.S., Edwards, H.G. and de Oliveira, L.F.C.,
1658   2015. Study of carotenoids in cyanobacteria by Raman spectroscopy. *Spectrochimica Acta Part*
1659   *A: Molecular and Biomolecular Spectroscopy*, *150*, pp.373-380.
1660   49.   De Sanctis, M.C., Ammannito, E., Raponi, A., Marchi, S., McCord, T.B., McSween, H.Y.,
1661   Capaccioni, F., Capria, M.T., Carrozzo, F.G., Ciarniello, M. and Longobardo, A., 2015.
1662   Ammoniated phyllosilicates with a likely outer Solar System origin on (1)
1663   Ceres. *Nature*, *528*(7581), pp.241-244.

1664   50.   Dupraz, C., Reid, R.P., Visscher, P.T., Reitner, J. and Thiel, V., 2011. Microbialites,
1665   modern. *Encyclopedia of geobiology*, pp.617-635.

1666   51.   Edwards, C.S. and Ehlmann, B.L., 2015. Carbon sequestration on Mars. *Geology*, *43*(10), pp.863-
1667   866.

1668   52.   Edwards, H.G., Villar, S.E.J., Jehlicka, J. and Munshi, T., 2005. FT–Raman spectroscopic study
1669   of calcium-rich and magnesium-rich carbonate minerals. *Spectrochimica Acta Part A: Molecular*
1670   *and Biomolecular Spectroscopy*, *61*(10), pp.2273-2280.

1671   53.   Ehlmann, B.L., Mustard, J.F., Fassett, C.I., Schon, S.C., Head III, J.W., Des Marais, D.J., Grant,
1672   J.A. and Murchie, S.L., 2008a. Clay minerals in delta deposits and organic preservation potential
1673   on Mars. *Nature Geoscience*, *1*(6), pp.355-358. doi:10.1038/ngeo207.

1674   54.   Ehlmann, B.L., Mustard, J.F., Murchie, S.L., Poulet, F., Bishop, J.L., Brown, A.J., Calvin, W.M.,
1675   Clark, R.N., Marais, D.J.D., Milliken, R.E. and Roach, L.H., 2008b. Orbital identification of
1676   carbonate-bearing rocks on Mars. *Science*, *322*(5909), pp.1828-1832.
1677   doi:10.1126/science.1164759.

1678   55.   Ehlmann, B.L., Mustard, J.F., Swayze, G.A., Clark, R.N., Bishop, J.L., Poulet, F., Des Marais,
1679   D.J., Roach, L.H., Milliken, R.E., Wray, J.J. and Barnouin-Jha, O., 2009. Identification of
1680   hydrated silicate minerals on Mars using MRO-CRISM: Geologic context near Nili Fossae and
1681   implications for aqueous alteration.

1682   56.   Ehlmann, B.L., Mustard, J.F. and Murchie, S.L., 2010. Geologic setting of serpentine deposits on
1683   Mars. *Geophysical research letters*, *37*(6).

1684   57.   Ehlmann, B.L. and Edwards, C.S., 2014. Mineralogy of the Martian surface. *Annual Review of*
1685   *Earth and Planetary Sciences*, *42*(1), pp.291-315.

1686   58.   Ehlmann, B.L. and Mustard, J.F., 2012. An in-situ record of major environmental transitions on
1687   early Mars at Northeast Syrtis Major. *Geophysical research letters, 39*(11).

1688   59.   Fairén, A.G., Davila, A.F., Lim, D., Bramall, N., Bonaccorsi, R., Zavaleta, J., Uceda, E.R.,
1689   Stoker, C., Wierzchos, J., Dohm, J.M. and Amils, R., 2010. Astrobiology through the ages of
1690   Mars: the study of terrestrial analogues to understand the habitability of
1691   Mars. *Astrobiology*, *10*(8), pp.821-843.

1692   60.   Falk, E.S. and Kelemen, P.B., 2015. Geochemistry and petrology of listvenite in the
1693   Samail ophiolite, Sultanate of Oman: Complete carbonation of peridotite during ophiolite
1694   emplacement. *Geochimica et Cosmochimica Acta*, *160*, pp.70-90.

1695   61.   Farley, K.A., Stack, K.M., Shuster, D.L., Horgan, B.H.N., Hurowitz, J.A., Tarnas, J.D., Simon,
1696   J.I., Sun, V.Z., Scheller, E.L., Moore, K.R. and McLennan, S.M., 2022. Aqueously altered
1697   igneous rocks sampled on the floor of Jezero crater, Mars. *Science*, *377*(6614), p.eabo2196.

1698   62.   Farmer, V.C., 1974. The infrared spectra of minerals: Mineralogical Society. *London,*
1699   *Monograph*, *4*, p.539.

1700   63.   Fischbeck, R. and Müller, G., 1971. Monohydrocalcite, hydromagnesite, nesquehonite, dolomite,
1701   aragonite, and calcite in speleothems of the Fränkische Schweiz, Western
1702   Germany. *Contributions to Mineralogy and Petrology*, *33*(2), pp.87-92.

1703   64.   Fassett, C.I. and Head III, J.W., 2005. Fluvial sedimentary deposits on Mars: Ancient deltas in a
1704   crater lake in the Nili Fossae region. *Geophysical Research Letters*, *32*(14).
1705   doi:10.1029/2005GL023456.

1706   65.   Fassett, C.I. and Head III, J.W., 2008. Valley network-fed, open-basin lakes on Mars:
1707   Distribution and implications for Noachian surface and subsurface hydrology. *Icarus*, *198*(1),
1708   pp.37-56.

1709   66.   Fassett, C.I. and Head, J.W., 2011. Sequence and timing of conditions on early
1710   Mars. *Icarus*, *211*(2), pp.1204-1214.

1711   67.   Frost, R.L., 2011. Raman spectroscopic study of the magnesium carbonate mineral
1712   hydromagnesite (Mg5 [(CO3) 4 (OH) 2]· 4H2O). *Journal of raman spectroscopy*, *42*(8), pp.1690-
1713   1694.

1714   68.   Gaffey, S.J., 1985. Reflectance spectroscopy in the visible and near-infrared (0.35–2.55 µm):
1715   Applications in carbonate petrology. *Geology*, *13*(4), pp.270-273.

1716   69.   Gaffey, S.J., 1987. Spectral reflectance of carbonate minerals in the visible and near infrared
1717   (0.35–2.55 um): Anhydrous carbonate minerals. *Journal of Geophysical Research: Solid*
1718   *Earth*, *92*(B2), pp.1429-1440.

1719   70.   Gaffey, S.J., McFadden, L.A., Nash, D. and Pieters, C.M., 1993. Ultraviolet, visible, and near-
1720   infrared reflectance spectroscopy: Laboratory spectra of geologic materials. *Remote geochemical*
1721   *analysis: Elemental and mineralogical composition*, *43*, p.77.

1722   71.   Garczynski, B., Horgan, B., Kah, L., Balci, N., Gunes, Y., Williford, K., Cloutis, E. and Dromart,
1723   G., 2021. Expected results of carbonate investigations by the perseverance rover in jezero crater:
1724   lessons from a fluviolacustrine analog at Lake Salda, Turkey. *Planetary and Space*
1725   *Science*, *67*(1), pp.28-45.

1726   72.   Glein, C.R. and Waite, J.H., 2020. The carbonate geochemistry of Enceladus' ocean. *Geophysical*
1727   *Research Letters*, *47*(3), p.e2019GL085885.

1728   73.   Gomez, F.J., Mlewski, C., Boidi, F.J., Farías, M.E. and Gérard, E., 2018. Calcium carbonate
1729   precipitation in diatom-rich microbial mats: the Laguna Negra hypersaline lake, Catamarca,
1730   Argentina. *Journal of Sedimentary Research*, *88*(6), pp.727-742.

1731　74.　Gooding, J.L., 1978. Chemical weathering on Mars thermodynamic stabilities of primary
1732　　　　minerals (and their alteration products) from mafic igneous rocks. *icarus*, *33*(3), pp.483-513.

1733　75.　Goudge, T.A., Mustard, J.F., Head, J.W., Fassett, C.I. and Wiseman, S.M., 2015. Assessing the
1734　　　　mineralogy of the watershed and fan deposits of the Jezero crater paleolake system,
1735　　　　Mars. *Journal of Geophysical Research: Planets*, *120*(4), pp.775-808.

1736　76.　Govindaraju, K., 1994. 1994 compilation of working values and sample description for 383
1737　　　　geostandards. *Geostandards newsletter*, *18*, pp.1-158.

1738　77.　Grant, J.A., Irwin III, R.P., Grotzinger, J.P., Milliken, R.E., Tornabene, L.L., McEwen, A.S.,
1739　　　　Weitz, C.M., Squyres, S.W., Glotch, T.D. and Thomson, B.J., 2008. HiRISE imaging of impact
1740　　　　megabreccia and sub-meter aqueous strata in Holden Crater, Mars. *Geology*, *36*(3), pp.195-198.

1741　78.　Grant, J.A., Wilson, S.A., Mangold, N., Calef III, F. and Grotzinger, J.P., 2014. The timing of
1742　　　　alluvial activity in Gale crater, Mars. *Geophysical Research Letters*, *41*(4), pp.1142-1149.

1743　79.　Grotzinger, J.P. and Knoll, A.H., 1995. Anomalous carbonate precipitates: is the Precambrian the
1744　　　　key to the Permian?. *Palaios*, pp.578-596.

1745　80.　Grotzinger, J.P. and Knoll, A.H., 1999. Stromatolites in Precambrian carbonates: evolutionary
1746　　　　mileposts or environmental dipsticks?. *Annual review of earth and planetary sciences*, *27*(1),
1747　　　　pp.313-358.

1748　81.　Grotzinger, J.P., Gupta, S., Malin, M.C., Rubin, D.M., Schieber, J., Siebach, K., Sumner, D.Y.,
1749　　　　Stack, K.M., Vasavada, A.R., Arvidson, R.E. and Calef III, F., 2015. Deposition, exhumation,
1750　　　　and paleoclimate of an ancient lake deposit, Gale crater, Mars. *Science*, *350*(6257), p.aac7575.

1751　82.　Gunasekaran, S. and Anbalagan, G., 2007. Spectroscopic study of phase transitions in dolomite
1752　　　　mineral. *Journal of Raman Spectroscopy: An International Journal for Original Work in all*
1753　　　　*Aspects of Raman Spectroscopy, Including Higher Order Processes, and also Brillouin and*
1754　　　　*Rayleigh Scattering*, *38*(7), pp.846-852.

1755　83.　Hamilton, V.E. and Christensen, P.R., 2005. Evidence for extensive, olivine-rich bedrock on
1756　　　　Mars. *Geology*, *33*(6), pp.433-436.

1757　84.　Hansen, L.D., Dipple, G.M., Gordon, T.M. and Kellett, D.A., 2005. Carbonated serpentinite
1758　　　　(listwanite) at Atlin, British Columbia: A geological analogue to carbon dioxide
1759　　　　sequestration. *The Canadian Mineralogist*, *43*(1), pp.225-239.

1760　85.　Harner, P.L. and Gilmore, M.S., 2015. Visible–near infrared spectra of hydrous carbonates, with
1761　　　　implications for the detection of carbonates in hyperspectral data of Mars. *Icarus*, *250*, pp.204-
1762　　　　214. https://doi.org/10.1016/j.icarus.2014.11.037

86. Hays, L.E., Graham, H.V., Des Marais, D.J., Hausrath, E.M., Horgan, B., McCollom, T.M., Parenteau, M.N., Potter-McIntyre, S.L., Williams, A.J. and Lynch, K.L., 2017. Biosignature preservation and detection in Mars analog environments. *Astrobiology*, *17*(4), pp.363-400.

87. Hendrix, A.R., Hurford, T.A., Barge, L.M., Bland, M.T., Bowman, J.S., Brinckerhoff, W., Buratti, B.J., Cable, M.L., Castillo-Rogez, J., Collins, G.C. and Diniega, S., 2019. The NASA roadmap to ocean worlds. *Astrobiology*, *19*(1), pp.1-27.

88. Hexter, R.M., 1958. High-resolution, temperature-dependent spectra of calcite. *Spectrochimica Acta*, *10*(3), pp.281-290.

89. Hoefen, T.M., Clark, R.N., Bandfield, J.L., Smith, M.D., Pearl, J.C. and Christensen, P.R., 2003. Discovery of olivine in the Nili Fossae region of Mars. *Science*, *302*(5645), pp.627-630.

90. Hollingbery, L.A. and Hull, T.R., 2010. The thermal decomposition of huntite and hydromagnesite—a review. *Thermochimica Acta*, *509*(1-2), pp.1-11. https://doi.org/10.1016/j.tca.2010.06.012.

91. Hopkinson, L., Rutt, K. and Cressey, G., 2008. The transformation of nesquehonite to hydromagnesite in the system CaO-MgO-H2O-CO2: An experimental spectroscopic study. *The Journal of Geology*, *116*(4), pp.387-400.

92. Horgan, B.H., Anderson, R.B., Dromart, G., Amador, E.S. and Rice, M.S., 2020. The mineral diversity of Jezero crater: Evidence for possible lacustrine carbonates on Mars. *Icarus*, *339*, pp.113526.

93. Htoon, M., 1979. *Geology of the Clinton Creek asbestos deposit, Yukon Territory* (Doctoral dissertation, University of British Columbia).

94. Hunt, G. R., and J. W., Salisbury (1971), Visible and near-infrared spectra of minerals and rocks: II. Carbonates, *Modern Geology*, 2, pp. 23–30.

95. Irwin III, R.P., Maxwell, T.A., Howard, A.D., Craddock, R.A. and Leverington, D.W., 2002. A large paleolake basin at the head of Ma'adim Vallis, Mars. *Science*, *296*(5576), pp.2209-2212.

96. Jakosky, B., 2018. Loss of the Martian atmosphere to space: Present-day loss rates from MAVEN observations and integrated loss through time. *42nd COSPAR Scientific Assembly*, *42*, pp.C3-2.

97. Jarwar, M.A., Dumontet, S., Pasquale, V. and Chen, C., 2022. Microbial Induced Carbonate Precipitation: Environments, Applications, and Mechanisms. *Geomicrobiology Journal*, *39*(10), pp.833-851.

98. Kasting, J.F., 1991. CO2 condensation and the climate of early Mars. *Icarus*, *94*(1), pp.1-13.

99. Kaźmierczak, J. and Altermann, W., 2002. Neoarchean biomineralization by benthic cyanobacteria. *science*, *298*(5602), pp.2351-2351.

1796   100.   Kaźmierczak J., Kempe S., Altermann W., 2004 Microbial origin of Precambrian carbonates:
1797   lessons from modern analogues. In: Eriksson PG, Altermann W, Nelson DR, Mueller WU,
1798   Catuneanu O (eds) The Precambrian earth–tempos and events. Elsevier, Amsterdam, pp 33–52.
1799   101.   Kaźmierczak, J., Kempe, S., Kremer, B., López-García, P., Moreira, D. and Tavera, R., 2011.
1800   Hydrochemistry and microbialites of the alkaline crater lake Alchichica, Mexico. *Facies*, *57*(4),
1801   pp.543-570.
1802   102.   Kempe, S. and Kazmierczak, J., 1997. A terrestrial model for an alkaline martian
1803   hydrosphere. *Planetary and space science*, *45*(11), pp.1493-1499.
1804   103.   King, T.V. and Ridley, W.I., 1987. Relation of the spectroscopic reflectance of olivine to mineral
1805   chemistry and some remote sensing implications. *Journal of Geophysical Research: Solid
1806   Earth*, *92*(B11), pp.11457-11469.
1807   104.   Kite, E.S., Steele, L.J., Mischna, M.A. and Richardson, M.I., 2021. Warm early Mars surface
1808   enabled by high-altitude water ice clouds. *Proceedings of the National Academy of
1809   Sciences*, *118*(18), p.e2101959118.
1810   105.   Königsberger, E., Königsberger, L.C. and Gamsjäger, H., 1999. Low-temperature thermodynamic
1811   model for the system Na_2CO_3- $MgCO_3-$ $CaCO_3-$ H_2O. *Geochimica et Cosmochimica
1812   Acta*, *63*(19-20), pp.3105-3119.
1813   106.   Kremer, C.H., Mustard, J.F. and Bramble, M.S., 2019. A widespread olivine-rich ash deposit on
1814   Mars. *Geology, 47*(7), pp.677-681.
1815   107.   Krishnamurti, D., 1956, April. Raman spectrum of magnesite. In *Proceedings of the Indian
1816   Academy of Sciences-Section A* (Vol. 43, No. 4, pp. 210-212). Springer India.
1817   108.   Lammer, H., Chassefière, E., Karatekin, Ö., Morschhauser, A., Niles, P.B., Mousis, O., Odert, P.,
1818   Möstl, U.V., Breuer, D., Dehant, V. and Grott, M., 2013. Outgassing history and escape of the
1819   Martian atmosphere and water inventory. *Space Science Reviews*, *174*, pp.113-154.
1820   109.   Lane, M.D. and Christensen, P.R., 1997. Thermal infrared emission spectroscopy of anhydrous
1821   carbonates. *Journal of Geophysical Research: Planets*, *102*(E11), pp.25581-25592.
1822   110.   Lepot, K., Benzerara, K., Brown, G.E. and Philippot, P., 2008. Microbially influenced formation
1823   of 2,724-million-year-old stromatolites. *Nature Geoscience*, *1*(2), pp.118-121.
1824   111.   Lepot, K., Benzerara, K., Rividi, N., Cotte, M., Brown Jr, G.E. and Philippot, P., 2009. Organic
1825   matter heterogeneities in 2.72 Ga stromatolites: alteration versus preservation by sulfur
1826   incorporation. *Geochimica et Cosmochimica Acta*, *73*(21), pp.6579-6599.
1827   112.   Lellouch, E., Encrenaz, T., de Graauw, T., Erard, S., Morris, P., Crovisier, J., Feuchtgruber, H.,
1828   Girard, T. and Burgdorf, M., 2000. The 2.4–45μm spectrum of Mars observed with the infrared
1829   space observatory. *Planetary and Space Science*, *48*(12-14), pp.1393-1405.

1830 113. Li, P., Feng, W., Xue, C., Tian, R. and Wang, S., 2017. Spatiotemporal variability of
1831   contaminants in lake water and their risks to human health: a case study of the Shahu Lake tourist
1832   area, northwest China. *Exposure and health*, *9*(3), pp.213-225.

1833 114. Liu, Y., Tice, M.M., Schmidt, M.E., Treiman, A.H., Kizovski, T.V., Hurowitz, J.A., Allwood,
1834   A.C., Henneke, J., Pedersen, D.A.K., VanBommel, S.J. and Jones, M.W.M., 2022. An olivine
1835   cumulate outcrop on the floor of Jezero crater, Mars. *Science*, *377*(6614), pp.1513-1519.

1836 115. Malin, M.C. and Edgett, K.S., 2003. Evidence for persistent flow and aqueous sedimentation on
1837   early Mars. *Science*, *302*(5652), pp.1931-1934.

1838 116. Mandon, L., Quantin-Nataf, C., Royer, C., Beck, P., Fouchet, T., Johnson, J.R., Dehouck, E., Le
1839   Mouélic, S., Poulet, F., Montmessin, F. and Pilorget, C., 2022. Reflectance of Jezero crater floor:
1840   2. Mineralogical interpretation. *Journal of Geophysical Research: Planets*, p.e2022JE007450.

1841 117. McGetchin, T.R. and Smith, J.R., 1978. The mantle of Mars: Some possible geological
1842   implications of its high density. *Icarus*, *34*(3), pp.512-536.

1843 118. McMahon, S., Bosak, T., Grotzinger, J.P., Milliken, R.E., Summons, R.E., Daye, M., Newman,
1844   S.A., Fraeman, A., Williford, K.H. and Briggs, D.E.G., 2018. A field guide to finding fossils on
1845   Mars. *Journal of Geophysical Research: Planets*, *123*(5), pp.1012-1040.

1846 119. Metz, J.M., Grotzinger, J.P., Mohrig, D., Milliken, R., Prather, B., Pirmez, C., McEwen, A.S. and
1847   Weitz, C.M., 2009. Sublacustrine depositional fans in southwest Melas Chasma. *Journal of*
1848   *Geophysical Research: Planets*, *114*(E10).

1849 120. Moore, J.M. and Howard, A.D., 2005. Large alluvial fans on Mars. *Journal of Geophysical*
1850   *Research: Planets*, *110*(E4). https://doi.org/10.1029/2004JE002352.

1851   Müller, G., Irion, G. and Förstner, U., 1972. Formation and Diagenesis of Inorganic Ca-Mg
1852   Carbonates. *Naturwissenschaften*, *59*, pp.158-164. https://doi.org/10.1007/BF00637354.

1853 121. Mertzman, S.A., 2000. K-Ar results from the southern Oregon-northern California Cascade
1854   Range. *Oregon Geology*, *62*(4), pp.99-122.

1855 122. Morris, R.V., Ruff, S.W., Gellert, R., Ming, D.W., Arvidson, R.E., Clark, B.C., Golden, D.C.,
1856   Siebach, K., Klingelhöfer, G., Schröder, C. and Fleischer, I., 2010. Identification of carbonate-
1857   rich outcrops on Mars by the Spirit rover. *Science*, *329*(5990), pp.421-424.

1858 123. Murchie, S.L., Mustard, J.F., Ehlmann, B.L., Milliken, R.E., Bishop, J.L., McKeown, N.K., Noe
1859   Dobrea, E.Z., Seelos, F.P., Buczkowski, D.L., Wiseman, S.M. and Arvidson, R.E., 2009. A
1860   synthesis of Martian aqueous mineralogy after 1 Mars year of observations from the Mars
1861   Reconnaissance Orbiter. *Journal of Geophysical Research: Planets*, *114*(E2).

124. Mustard, J.F., Ehlmann, B.L., Murchie, S.L., Poulet, F., Mangold, N., Head, J.W., Bibring, J.P. and Roach, L.H., 2009. Composition, morphology, and stratigraphy of Noachian crust around the Isidis basin. *Journal of Geophysical Research: Planets*, *114*(E2). doi:10.1029/2009JE003349.

125. Mustard, J.F., Poulet, F., Head, J.W., Mangold, N., Bibring, J.P., Pelkey, S.M., Fassett, C.I., Langevin, Y. and Neukum, G., 2007. Mineralogy of the Nili Fossae region with OMEGA/Mars Express data: 1. Ancient impact melt in the Isidis Basin and implications for the transition from the Noachian to Hesperian. *Journal of Geophysical Research: Planets*, *112*(E8). doi:10.1029/2006JE002834.

126. Mustard, J.F. and Sunshine, J.M., 1995. Seeing through the dust: Martian crustal heterogeneity and links to the SNC meteorites. *Science*, *267*(5204), pp.1623-1626.

127. Neveu, M., Anbar, A.D., Davila, A., Glavin, D.P., MacKenzie, S.M., Phillips-Lander, C., Sherwood, B., Takano, Y., Williams, P. and Yano, H., 2021. Returning Samples from Enceladus for Life Detection. *Bulletin of the American Astronomical Society*, *53*(4), p.052.

128. Oskierski, H.C., Beinlich, A., Mavromatis, V., Altarawneh, M. and Dlugogorski, B.Z., 2019. Mg isotope fractionation during continental weathering and low temperature carbonation of ultramafic rocks. *Geochimica et Cosmochimica Acta*, *262*, pp.60-77.

129. Palomba, E., Longobardo, A., De Sanctis, M.C., Stein, N.T., Ehlmann, B., Galiano, A.N.N.A., Raponi, A., Ciarniello, M., Ammannito, E., Cloutis, E. and Carrozzo, F.G., 2019. Compositional differences among Bright Spots on the Ceres surface. *Icarus*, *320*, pp.202-212.

130. Pecoraino, G., D'Alessandro, W., & Inguaggiato, S. (2015). The other side of the coin: geochemistry of alkaline lakes in volcanic areas. In D. Rouwet, B. Christenson, F. Tassi, & J. Vandemeulebrouck (Eds.), Volcanic lakes, *Advances in Volcanology*.

131. Pinet, P. and Chevrel, S., 1990. Spectral identification of geological units on the surface of Mars related to the presence of silicates from Earth-based near-infrared telescopic charge-coupled device imaging. *Journal of Geophysical Research: Solid Earth*, *95*(B9), pp.14435-14446.

132. Pollack, J.B., Roush, T., Witteborn, F., Bregman, J., Wooden, D., Stoker, C., Toon, O.B., Rank, D., Dalton, B. and Freedman, R., 1990. Thermal emission spectra of Mars (5.4–10.5 μm): Evidence for sulfates, carbonates, and hydrates. *Journal of Geophysical Research: Solid Earth*, *95*(B9), pp.14595-14627.

133. Poulet, F., Mangold, N., Platevoet, B., Bardintzeff, J.M., Sautter, V., Mustard, J.F., Bibring, J.P., Pinet, P., Langevin, Y., Gondet, B. and Aléon-Toppani, A., 2009. Quantitative compositional analysis of Martian mafic regions using the MEx/OMEGA reflectance data: 2. Petrological implications. *Icarus*, *201*(1), pp.84-101.

1895 134. Power, I.M., Wilson, S.A., Thom, J.M., Dipple, G.M. and Southam, G., 2007. Biologically
1896   induced mineralization of dypingite by cyanobacteria from an alkaline wetland near Atlin, British
1897   Columbia, Canada. *Geochemical Transactions*, *8*(1), pp.1-16.
1898 135. Power, I.M., Wilson, S.A., Thom, J.M., Dipple, G.M., Gabites, J.E. and Southam, G., 2009. The
1899   hydromagnesite playas of Atlin, British Columbia, Canada: A biogeochemical model for CO2
1900   sequestration. *Chemical Geology*, *260*(3-4), pp.286-300.
1901 136. Power, I.M., Wilson, S.A., Dipple, G.M. and Southam, G., 2011. Modern carbonate microbialites
1902   from an asbestos open pit pond, Yukon, Canada. *Geobiology*, *9*(2), pp.180-195.
1903 137. Power, I.M., Wilson, S.A., Harrison, A.L., Dipple, G.M., McCutcheon, J., Southam, G. and
1904   Kenward, P.A., 2014. A depositional model for hydromagnesite–magnesite playas near Atlin,
1905   British Columbia, Canada. *Sedimentology*, *61*(6), pp.1701-1733.
1906   https://doi.org/10.1111/sed.12124.
1907 138. Ramírez-García, P. and Vázquez-Gutiérrez, F., 1989. Contribuciones al estudio limnobotánico de
1908   la zona litoral de seis lagos cráter del estado de Puebla. In *Anales del Instituto de Ciencias del*
1909   *Mar y Limnología* (Vol. 323, pp. 1-16). Universidad Nacional Autónoma de México.
1910 139. Reichen, L.E., Fahey, J.J. 1962, An improved method for the determination of FeO in rocks and
1911   minerals including garnet. *U.S. Geological Survey Bulletin*, 1144-B, pp. 1-5.
1912 140. Renaut, R.W., 1993. Morphology, distribution, and preservation potential of microbial mats in the
1913   hydromagnesite-magnesite playas of the Cariboo Plateau, British Columbia,
1914   Canada. *Hydrobiologia*, *267*(1), pp.75-98.
1915 141. Riding, R., 2011. Microbialites, stromatolites, and thrombolites. In *Encyclopedia of geobiology*.
1916 142. Ronholm, J., Schumann, D., Sapers, H.M., Izawa, M., Applin, D., Berg, B., Mann, P., Vali, H.,
1917   Flemming, R.L., Cloutis, E.A. and Whyte, L.G., 2014. A mineralogical characterization of
1918   biogenic calcium carbonates precipitated by heterotrophic bacteria isolated from cryophilic polar
1919   regions. *Geobiology*, *12*(6), pp.542-556.
1920 143. Ruesch, O., Platz, T., Schenk, P., McFadden, L.A., Castillo-Rogez, J.C., Quick, L.C., Byrne, S.,
1921   Preusker, F., O'Brien, D.P., Schmedemann, N. and Williams, D.A., 2016. Cryovolcanism on
1922   ceres. *Science*, *353*(6303).
1923 144. Ruff, S.W., Niles, P.B., Alfano, F. and Clarke, A.B., 2014. Evidence for a Noachian-aged
1924   ephemeral lake in Gusev crater, Mars. *Geology*, *42*(4), pp.359-362.
1925 145. Russell, M.J., Ingham, J.K., Zedef, V., Maktav, D., Sunar, F., Hall, A.J. and Fallick, A.E., 1999.
1926   Search for signs of ancient life on Mars: expectations from hydromagnesite microbialites, Salda
1927   Lake, Turkey. *Journal of the Geological Society*, *156*(5), pp.869-888.

1928   146.   Russell, M.J. and Hall, A.J., 1999. On the inevitable emergence of life on Mars. In Proc. 1st UK
1929   Conference Search for Life on Mars. *British Interplanetary Society* 26-36.

1930   147.   Salisbury, J.W., Walter, L.S. and Vergo, N., 1991. D, Aria, DM Infrared ($2.1-25$ μm) Spectra of
1931   Minerals. John Hopkins Univ. Press, Baltimore, MD, USA.

1932   148.   Sánchez-Román, M., Romanek, C.S., Fernández-Remolar, D.C., Sánchez-Navas, A., McKenzie,
1933   J.A., Pibernat, R.A. and Vasconcelos, C., 2011. Aerobic biomineralization of Mg-rich carbonates:
1934   Implications for natural environments. *Chemical Geology*, *281*(3-4), pp.143-150.

1935   149.   Sato, R.K. and McMillan, P.F., 1987. An infrared and Raman study of the isotopic species of.
1936   alpha.-quartz. *Journal of Physical Chemistry*, *91*(13), pp.3494-3498.

1937   150.   Schandl, E.S. and Naldrett, A.J., 1992. CO 2 metasomatism of serpentinites, south of Timmons,
1938   Ontario. *The Canadian Mineralogist*, *30*(1), pp.93-108.

1939   151.   Schon, S.C., Head, J.W. and Fassett, C.I., 2012. An overfilled lacustrine system and
1940   progradational delta in Jezero crater, Mars: Implications for Noachian climate. *Planetary and*
1941   *Space Science*, *67*(1), pp.28-45.doi:10.1016/j.pss.2012.02.003.

1942   152.   Schultz, R.A. and Frey, H.V., 1990. A new survey of multiring impact basins on Mars. *Journal of*
1943   *Geophysical Research: Solid Earth*, *95*(B9), pp.14175-14189. doi:10.1029/JB095iB09p14175.

1944   153.   Schroeder, R.A., Weir, C.E. and Lippincott, E.R., 1962. Lattice frequencies and rotational
1945   barriers for inorganic carbonates and nitrates from low temperature infrared
1946   spectroscopy. *Journal of Research of the National Bureau of Standards*, *66*, pp.407-434.

1947   154.   Senel, M., Selçuk, H., Bilgin, Z. R., Sen, A. M., Karaman, T., & Dinçer, M. A., et al. (1989).
1948   Geology of the Çameli (Denizli)-Yesilova (Burdur)-Elmalı (Antalya) and the northern part.
1949   Mineral Research & Exploration General Directorate Rep: 9429 (unpublished), Ankara-Turkey
1950   (in Turkish).

1951   155.   Shapiro, R.S. and Konhauser, K.O., 2015. Hematite-coated microfossils: primary ecological
1952   fingerprint or taphonomic oddity of the Paleoproterozoic?. *Geobiology*, *13*(3), pp.209-224.

1953   156.   Shirokova, L.S., Mavromatis, V., Bundeleva, I.A., Pokrovsky, O.S., Bénézeth, P., Gérard, E.,
1954   Pearce, C.R. and Oelkers, E.H., 2013. Using Mg isotopes to trace cyanobacterially mediated
1955   magnesium carbonate precipitation in alkaline lakes. *Aquatic Geochemistry*, *19*(1), pp.1-24.

1956   157.   Silva-Aguilera, R.A., Vilaclara, G., Armienta, M.A. and Escolero, Ó., 2022. Hydrogeology and
1957   hydrochemistry of the Serdán-Oriental Basin and the Lake Alchichica. In *Lake Alchichica*
1958   *Limnology* (pp. 63-74). Springer, Cham.

1959   158.   Spadafora, A., Perri, E., McKenzie, J.A. and Vasconcelos, C., 2010. Microbial biomineralization
1960   processes forming modern Ca: Mg carbonate stromatolites. *Sedimentology*, *57*(1), pp.27-40.

1961   159.   Stack, K.M., Williams, N.R., Calef, F., Sun, V.Z., Williford, K.H., Farley, K.A., Eide, S.,
1962   Flannery, D., Hughes, C., Jacob, S.R. and Kah, L.C., 2020. Photogeologic map of the
1963   perseverance rover field site in Jezero Crater constructed by the Mars 2020 Science Team. *Space*
1964   *science reviews*, *216*, pp.1-47.

1965   160.   Stromberg, J.M., Applin, D.M., Cloutis, E.A., Rice, M., Berard, G. and Mann, P., 2014. The
1966   persistence of a chlorophyll spectral biosignature from Martian evaporite and spring analogues
1967   under Mars-like conditions. *International Journal of Astrobiology*, *13*(3), pp.203-223.

1968   161.   Stromberg, J.M., Parkinson, A., Morison, M., Cloutis, E., Casson, N., Applin, D., Poitras, J.,
1969   Marti, A.M., Maggiori, C., Cousins, C. and Whyte, L., 2019. Biosignature detection by Mars
1970   rover equivalent instruments in samples from the CanMars Mars Sample Return Analogue
1971   Deployment. *Planetary and Space Science*, *176*, p.104683.

1972   162.   Sun, J., Wu, Z., Cheng, H., Zhang, Z. and Frost, R.L., 2014. A Raman spectroscopic comparison
1973   of calcite and dolomite. *Spectrochimica Acta Part A: Molecular and Biomolecular*
1974   *Spectroscopy*, *117*, pp.158-162.

1975   163.   Sun, V.Z. and Stack, K.M., 2020. Geologic map of Jezero crater and the Nili Planum region,
1976   Mars. *US Geological Survey Scientific Investigations Map*, *3464*(10.3133).

1977   164.   Szponar, N., Brazelton, W.J., Schrenk, M.O., Bower, D.M., Steele, A. and Morrill, P.L., 2013.
1978   Geochemistry of a continental site of serpentinization, the Tablelands Ophiolite, Gros Morne
1979   National Park: a Mars analogue. *Icarus*, *224*(2), pp.286-296.

1980   165.   Tarnas, J.D., Stack, K.M., Parente, M., Koeppel, A.H.D., Mustard, J.F., Moore, K.R., Horgan,
1981   B.H.N., Seelos, F.P., Cloutis, E.A., Kelemen, P.B. and Flannery, D., 2021. Characteristics,
1982   Origins, and Biosignature Preservation Potential of Carbonate-Bearing Rocks Within and Outside
1983   of Jezero Crater. *Journal of Geophysical Research: Planets*, *126*(11), p.e2021JE006898.

1984   166.   Taubner, R.S., Pappenreiter, P., Zwicker, J., Smrzka, D., Pruckner, C., Kolar, P., Bernacchi, S.,
1985   Seifert, A.H., Krajete, A., Bach, W. and Peckmann, J., 2018. Biological methane production
1986   under putative Enceladus-like conditions. *Nature communications*, *9*(1), pp.1-11.

1987   167.   Tavera, R. and Komárek, J., 1996. Cyanoprokaryotes in the volcanic lake of Alchichica, Puebla
1988   State, Mexico. *Algological Studies/Archiv für Hydrobiologie, Supplement Volumes*, pp.511-538.

1989   168.   Teir, S., Eloneva, S., Fogelholm, C.J., Zevenhoven, R., 2009. Fixation of carbon dioxide by
1990   producing hydromagnesite from serpentinite. Applied Energy 86 (2), 214–218.

1991   169.   Tice, M.M., Hurowitz, J.A., Allwood, A.C., Jones, M.W., Orenstein, B.J., Davidoff, S., Wright,
1992   A.P., Pedersen, D.A., Henneke, J., Tosca, N.J. and Moore, K.R., 2022. Alteration history of
1993   Séítah formation rocks inferred by PIXL x-ray fluorescence, x-ray diffraction, and multispectral
1994   imaging on Mars. *Science Advances*, *8*(47), p.eabp9084.

1995   170.   Treiman, A.H., 1986. The parental magma of the Nakhla achondrite: Ultrabasic volcanism on the
1996   shergottite parent body. *Geochimica et Cosmochimica Acta*, *50*(6), pp.1061-1070.

1997   171.   Turenne, N., Cloutis, E., Applin, D., Burnie, T. and Power, I., 2021, December. Stability of
1998   Hydromagnesite on Mars Under Current Surface Conditions and (Impact) Heating. In *AGU Fall*
1999   *Meeting Abstracts* (Vol. 2021, pp. EP55A-1105).

2000   172.   Udry, A., Ostwald, A., Sautter, V., Cousin, A., Beyssac, O., Forni, O., Dromart, G., Benzerara,
2001   K., Nachon, M., Horgan, B. and Mandon, L., 2022. A Mars 2020 Perseverance SuperCam
2002   Perspective on the Igneous Nature of the Máaz formation at Jezero crater and link with Séítah,
2003   Mars. *Journal of Geophysical Research: Planets*, p.e2022JE007440.

2004   173.   Vágvölgyi, V., Frost, R.L., Hales, M., Locke, A., Kristóf, J. and Horváth, E., 2008. Controlled
2005   rate thermal analysis of hydromagnesite. *Journal of Thermal Analysis and Calorimetry*, *92*(3),
2006   pp.893-897. https://doi.org/10.1007/s10973-007-8845-6.

2007   174.   Vance, R.E., Mathewes, R.W. and Clague, J.J., 1992. 7000 year record of lake-level change on
2008   the northern Great Plains: A high-resolution proxy of past climate. *Geology*, *20*(10), pp.879-882.
2009   doi: https://doi.org/10.1130/0091-7613(1992)020<0879:YROLLC>2.3.CO;2

2010   175.   Vilaclara, G., Chávez, M., Lugo, A., González, H. and Gaytán, M., 1993. Comparative
2011   description of crater-lakes basic chemistry in Puebla State, Mexico. *Internationale Vereinigung*
2012   *für theoretische und angewandte Limnologie: Verhandlungen*, *25*(1), pp.435-440.

2013   176.   Viviano, C.E., Moersch, J.E. and McSween, H.Y., 2013. Implications for early hydrothermal
2014   environments on Mars through the spectral evidence for carbonation and chloritization reactions
2015   in the Nili Fossae region. *Journal of Geophysical Research: Planets*, *118*(9), pp.1858-1872.

2016   177.   Wade, L., Allwood, A., Foote, M., Dawson, D., Liebe, C., Ek, E., Schein, M., Pootrakul, S.,
2017   Hernandez, B., Sharrow, R. 2016, Overview of the Mars 2020 mission micro-XRF instrument
2018   PIXL. *251st American Chemical Society National Meeting & Exposition*, March 13-17, 2016, San
2019   Diego, CA; http://www.acs.org/content/acs/en/meetings/spring-2016.html.

2020   178.   Walter, M.R., Golubic, S. and Preiss, W.V., 1973. Recent stromatolites from hydromagnesite and
2021   aragonite depositing lakes near the Coorong Lagoon, South Australia. *Journal of Sedimentary*
2022   *Research*, *43*(4).

2023   179.   Walter, M.R., 1983. Archean stromatolites: evidence of the Earth's earliest benthos. *Earth's*
2024   *Earliest Biosphere.*, pp.187-213.

2025   180.   Wang, D., Hamm, L.M., Bodnar, R.J. and Dove, P.M., 2012. Raman spectroscopic
2026   characterization of the magnesium content in amorphous calcium carbonates. *Journal of Raman*
2027   *Spectroscopy*, *43*(4), pp.543-548.

2028 181. Wang, Q., Zhang, Y. and Wu, X., 2015. Triassic (Carnian) hexactinellid-thrombolite reef mounds
2029 and oolitic bank complex in NW Sichuan, China. *Carbonates and Evaporites*, *30*(2), pp.187-205.

2030 182. Warren, P.H., 1998. Petrologic evidence for low-temperature, possibly flood evaporitic origin of
2031 carbonates in the ALH84001 meteorite. *Journal of Geophysical Research: Planets*, *103*(E7),
2032 pp.16759-16773.

2033 183. Werner, S.C., 2008. The early Martian evolution—Constraints from basin formation
2034 ages. *Icarus*, *195*(1), pp.45-60. doi:10.1016/j.icarus.2007.12.008.

2035 184. Westall, F., Cavalazzi B. Biosignatures in rocks. In: (Reitner, J, Thiel, V., Eds.). *Encyclopedia of*
2036 *Geobiology*, Springer-Verlag, 1st Edition. 2011, XXVIII, 928, 482, 2011, *Encyclopedia of Earth*
2037 *Sciences Series*.

2038 185. Westall, F., Loizeau, D., Foucher, F., Bost, N., Betrand, M., Vago, J. and Kminek, G., 2013.
2039 Habitability on Mars from a microbial point of view. *Astrobiology*, *13*(9), pp.887-897.

2040 186. Westall, F., Foucher, F., Bost, N., Bertrand, M., Loizeau, D., Vago, J.L., Kminek, G., Gaboyer,
2041 F., Campbell, K.A., Bréhéret, J.G. and Gautret, P., 2015. Biosignatures on Mars: what, where,
2042 and how? Implications for the search for martian life. *Astrobiology*, *15*(11), pp.998-1029.

2043 187. White, W.B., 1974. The carbonate minerals. In V. C. Farmer, ed. The infrared spectra of
2044 minerals. Mineral. Soc. Monogr. 4:227–284.. https://doi.org/10.1180/mono-4.12

2045 188. Wiens, R.C., Maurice, S., Mccabe, K., Cais, P., Anderson, R.B., Beyssac, O., Bonal, L., Clegg,
2046 S., Deflores, L., Dromart, G. and Fischer, W.W., 2016. The SuperCam remote sensing instrument
2047 suite for Mars 2020. *In 47th Lunar and Planetary Science Conference*, 1322.

2048 189. Wiens, R.C., Maurice, S., Robinson, S.H., Nelson, A.E., Cais, P., Bernardi, P., Newell, R.T.,
2049 Clegg, S., Sharma, S.K., Storms, S. and Deming, J., 2021. The SuperCam instrument suite on the
2050 NASA Mars 2020 rover: body unit and combined system tests. *Space Science Reviews*, *217*(1),
2051 pp.1-87.

2052 190. Wiens, R.C., Udry, A., Beyssac, O., Quantin-Nataf, C., Mangold, N., Cousin, A., Mandon, L.,
2053 Bosak, T., Forni, O., Mclennan, S.M. and Sautter, V., 2022. Compositionally and density
2054 stratified igneous terrain in Jezero crater, Mars. *Science Advances*, *8*(34), p.eabo3399.

2055 191. Williford, K.H, Farley, K.A., Stack, K.M., Allwood, A.C., Beaty, D., Beegle, L., Bhartia, R.,
2056 Brown, A.J., de la Torre Juarez, M., Hamran, S.-E, Hecht, M.H., Hurowitz, J., Rodriguez-
2057 Manfredi, J.A., Maurice, S., Milkovich, S., Wiens, R.C., 2017. The NASA Mars 2020 rover
2058 mission and the search for extraterrestrial life, *In: From Habitability to Life on Mars,* Cabrol,
2059 N.A., and E.A. Grin, eds., Chapter 11, Elsevier.

2060 192. Wilson, S.A., Dipple, G.M., Power, I.M., Thom, J.M., Anderson, R.G., Raudsepp, M., Gabites,
2061 J.E. and Southam, G., 2009. Carbon dioxide fixation within mine wastes of ultramafic-hosted ore

deposits: Examples from the Clinton Creek and Cassiar chrysotile deposits, Canada. *Economic geology*, *104*(1), pp.95-112.

193. Wilson, S.A., Raudsepp, M. and Dipple, G.M., 2006. Verifying and quantifying carbon fixation in minerals from serpentine-rich mine tailings using the Rietveld method with X-ray powder diffraction data. *American Mineralogist*, *91*(8-9), pp.1331-1341.

194. Wilson, S.A., Dipple, G.M., Power, I.M., Barker, S.L., Fallon, S.J. and Southam, G., 2011. Subarctic weathering of mineral wastes provides a sink for atmospheric CO2. *Environmental science & technology*, *45*(18), pp.7727-7736. https://doi.org/10.1021/es202112y.

195. Wittkopp, R.W., 1983. Hypothesis for the localization of gold in quartz veins: Alleghany district. *Sierra County, California: California Geology*, *36*, pp.123-127.

196. Wood, C.E., Qafoku, O., Loring, J.S. and Chaka, A.M., 2019. Role of Fe (II) content in olivine carbonation in wet supercritical CO2. *Environmental Science & Technology Letters*, *6*(10), pp.592-599.

197. Wolfe, A.P., Vinebrooke, R.D., Michelutti, N., Rivard, B. and Das, B., 2006. Experimental calibration of lake-sediment spectral reflectance to chlorophyll a concentrations: methodology and paleolimnological validation. *Journal of Paleolimnology*, *36*(1), pp.91-100.

198. Wu, J., Xue, C., Tian, R. and Wang, S., 2017. Lake water quality assessment: a case study of Shahu Lake in the semiarid loess area of northwest China. *Environmental Earth Sciences*, *76*(5), pp.1-15.

199. Zastrow, A.M. and Glotch, T.D., 2021. Distinct carbonate lithologies in Jezero crater, Mars. *Geophysical Research Letters*, *48*(9), p.e2020GL092365.

200. Zedef, V., Russell, M.J., Fallick, A.E. and Hall, A.J., 2000. Genesis of vein stockwork and sedimentary magnesite and hydromagnesite deposits in the ultramafic terranes of southwestern Turkey: a stable isotope study. *Economic Geology*, *95*(2), pp.429-445.

201. Zent, A.P. and Quinn, R.C., 1995. Simultaneous adsorption of CO2 and H2O under Mars-like conditions and application to the evolution of the Martian climate. *Journal of Geophysical Research: Planets*, *100*(E3), pp.5341-5349.

202. Zhu, T. and Dittrich, M., 2016. Carbonate precipitation through microbial activities in natural environment, and their potential in biotechnology: a review. *Frontiers in bioengineering and biotechnology*, *4*, p.4.

203. Zolotov, M.Y. and Shock, E.L., 2003. Energy for biologic sulfate reduction in a hydrothermally formed ocean on Europa. *Journal of Geophysical Research: Planets*, *108*(E4).

2094 **10. Supplemental material**
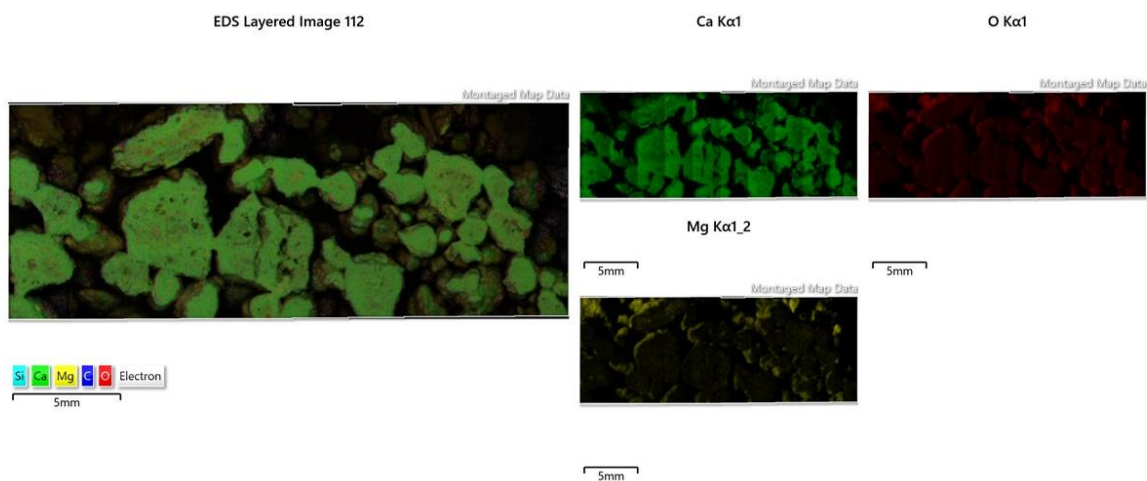
2095

2096 **Figure 1**. ATP1 SEM elemental map identifying Ca, Mg, and O.
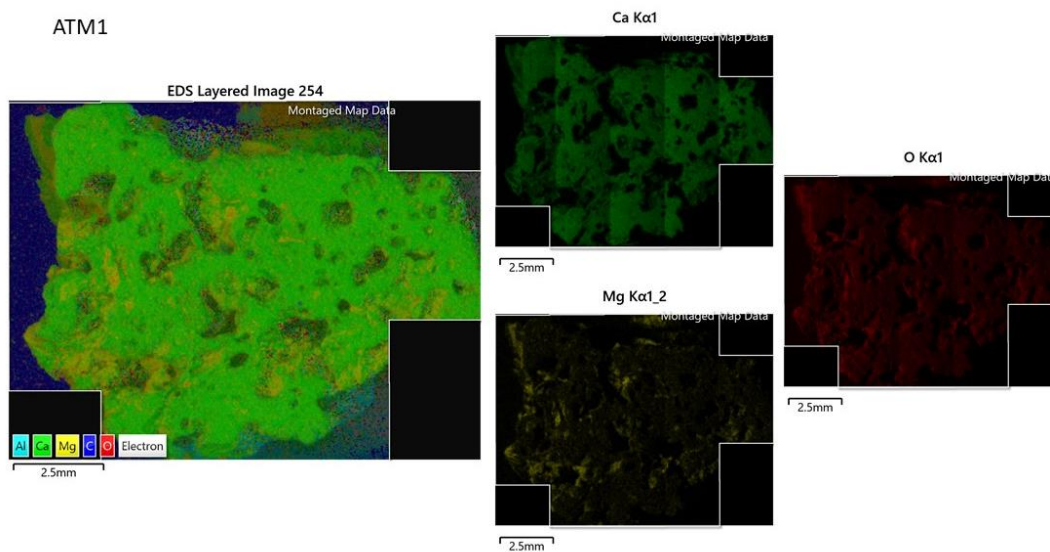
2097
2098 **Figure 2**. ATM1 SEM elemental map identifying Ca, Mg, and O.
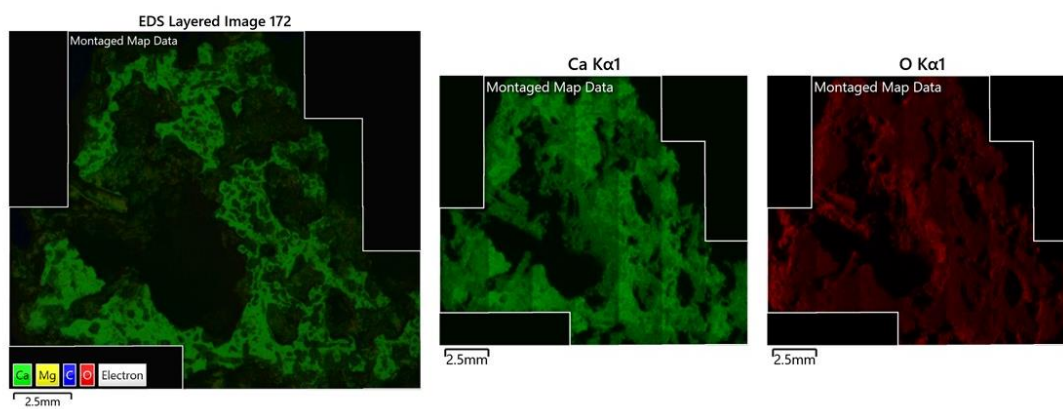
2099

2100   **Figure 3**. ATA1 SEM elemental map identifying Ca, and O.
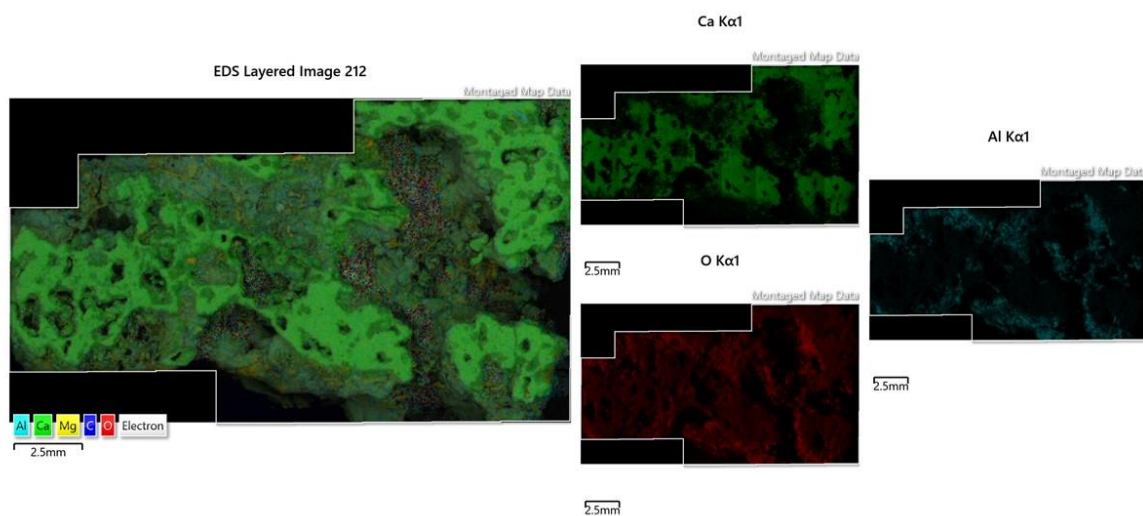

2101

2102   **Figure 4**. CC1 SEM elemental map identifying Ca, Mg, and O.
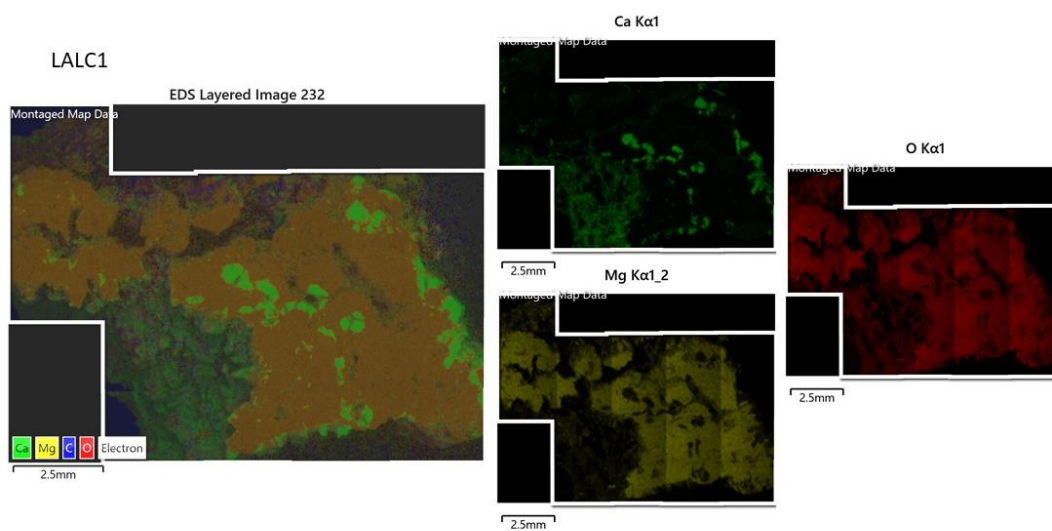
2103
2104   **Figure 5**. LAL-C1 SEM elemental map identifying Ca, Mg, and O.

2105
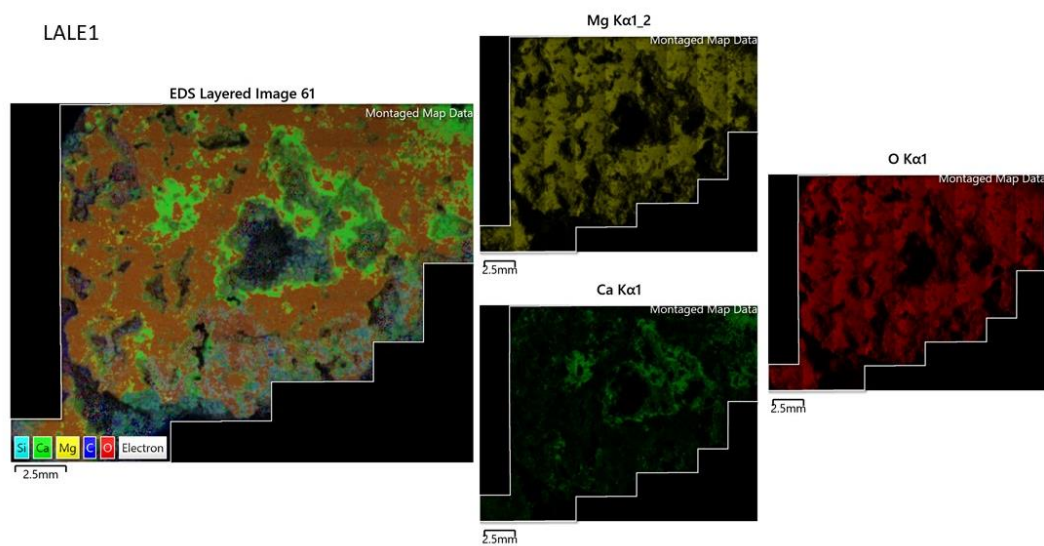
Figure 6. LAL-E1 SEM elemental map identifying Ca, Mg, and O.
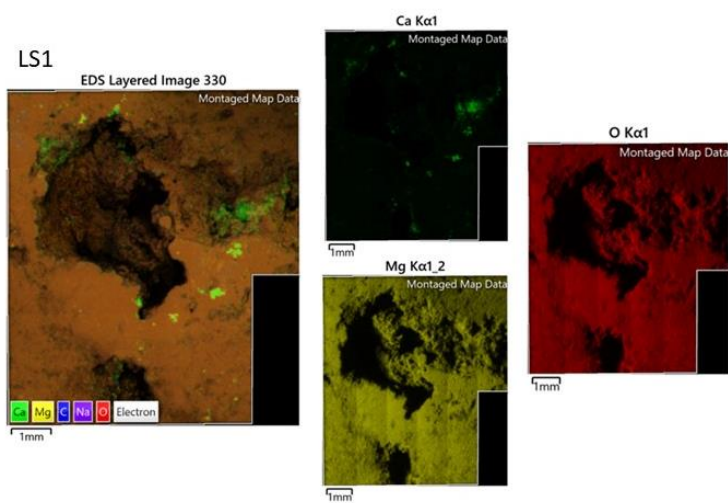
Figure 7. LS1 SEM elemental map identifying Ca, Mg, and O.
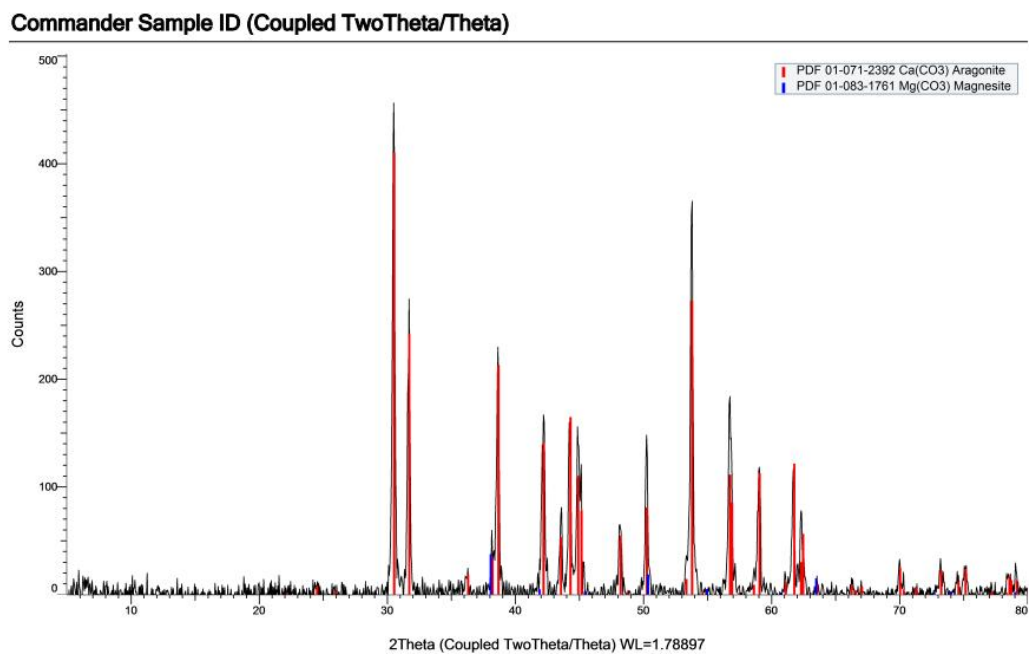
2112

2113 **Figure 8**. ATP3 XRD data
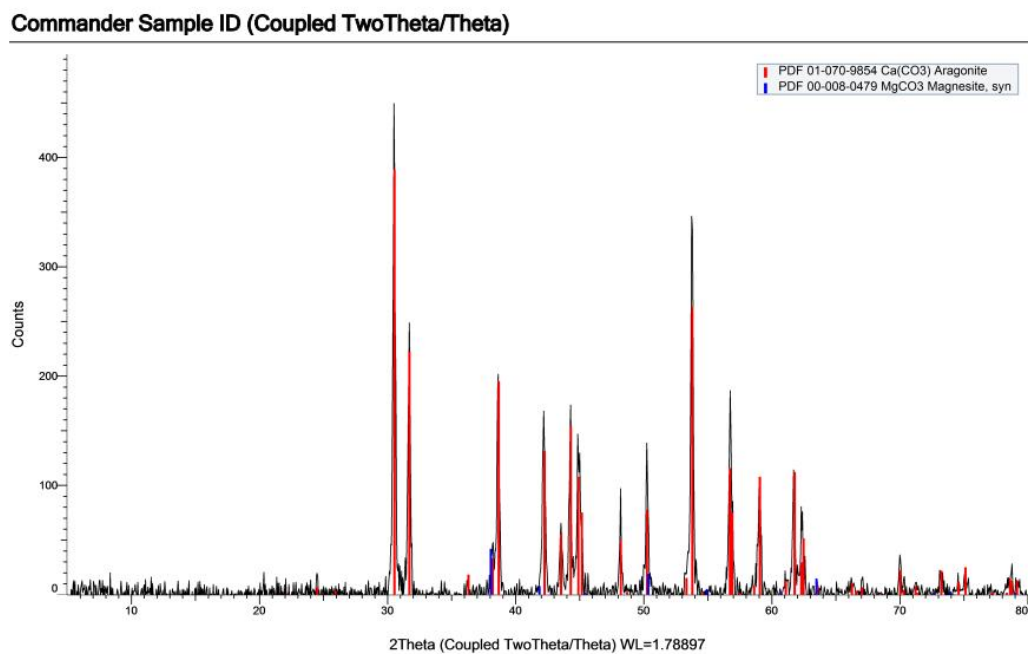
2114

Figure 9. ATM3 XRD data
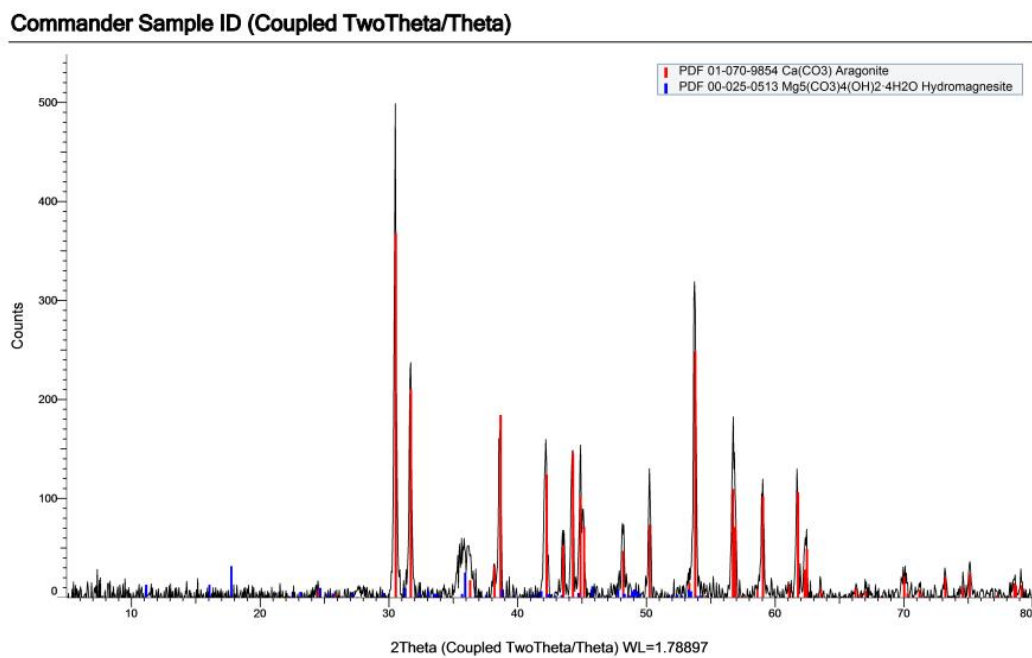
Figure 10. ATA3 XRD data
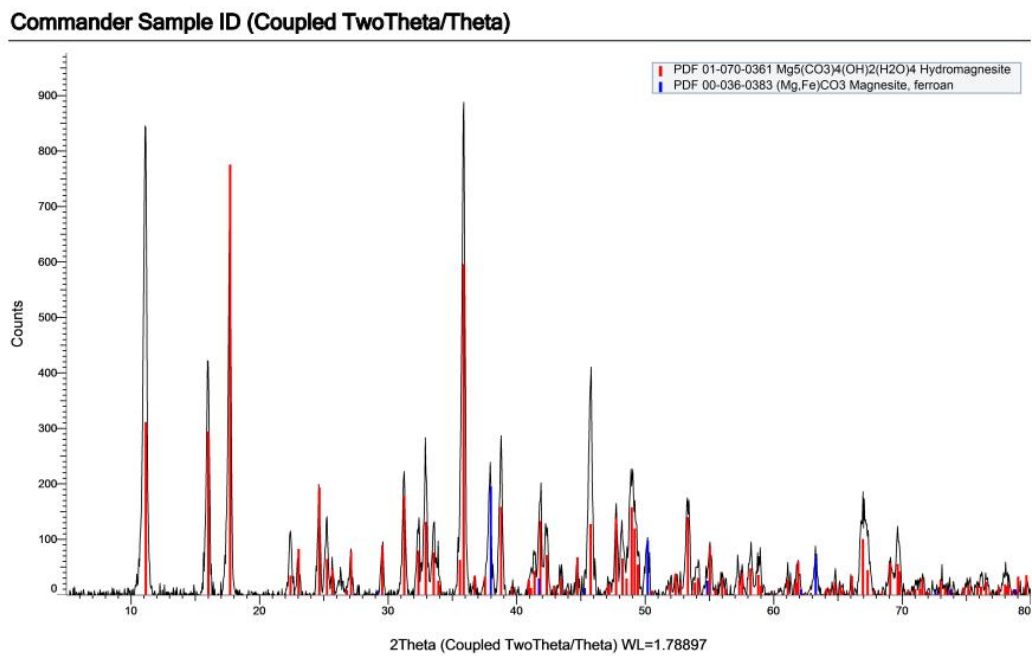
2118

Figure 11. ATH3 XRD data
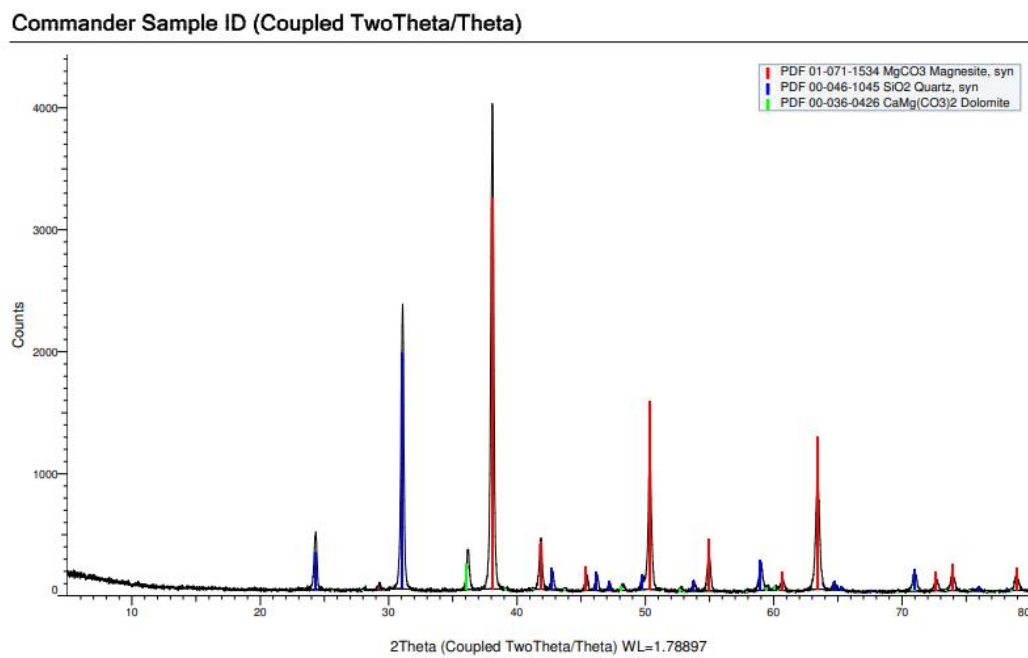
Figure 12. 16AT-PI-1 XRD data
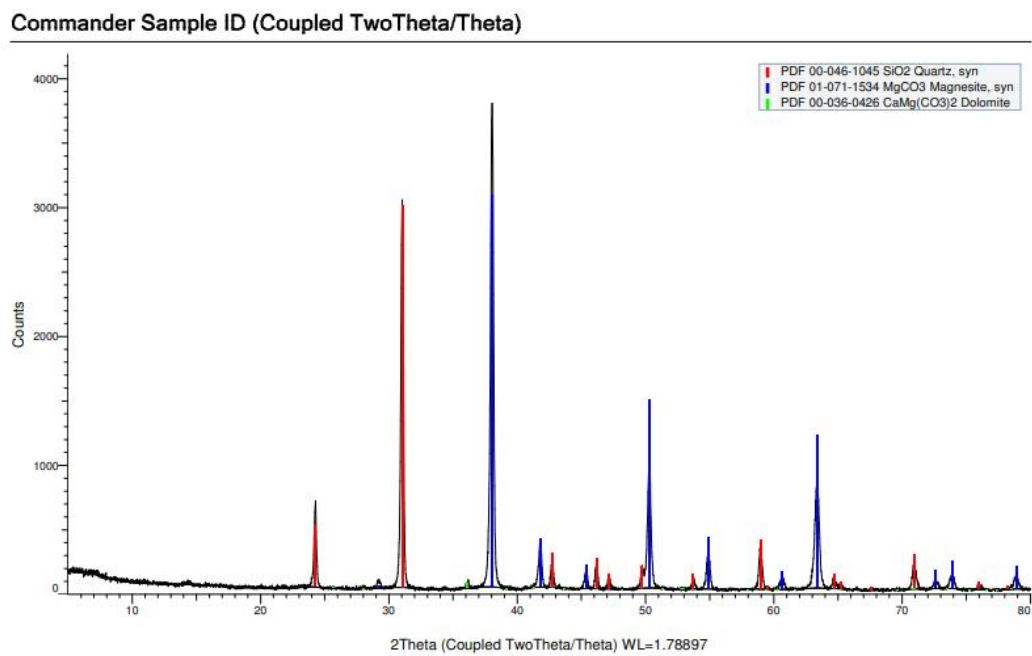
Figure 13. 16AT-PI-2 XRD data

Commander Sample ID (Coupled TwoTheta/Theta)

PDF 00-046-1045 SiO2 Quartz, syn
PDF 00-036-0426 CaMg(CO3)2 Dolomite
PDF 01-071-1534 MgCO3 Magnesite, syn

2Theta (Coupled TwoTheta/Theta) WL=1.78897
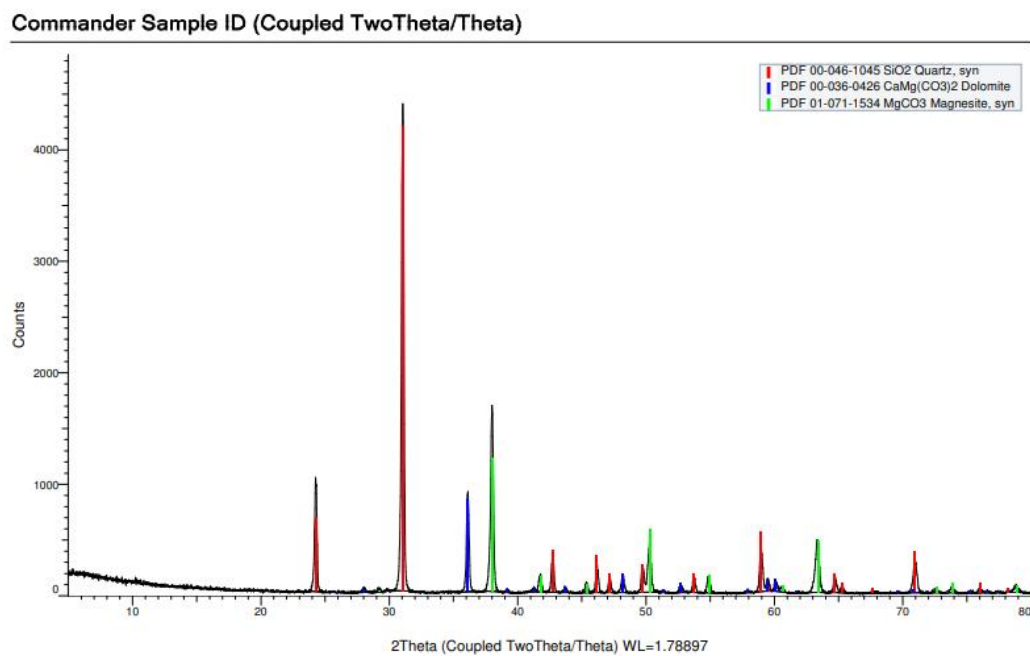
2124

2125 **Figure 14.** 16AT-ANNA XRD data
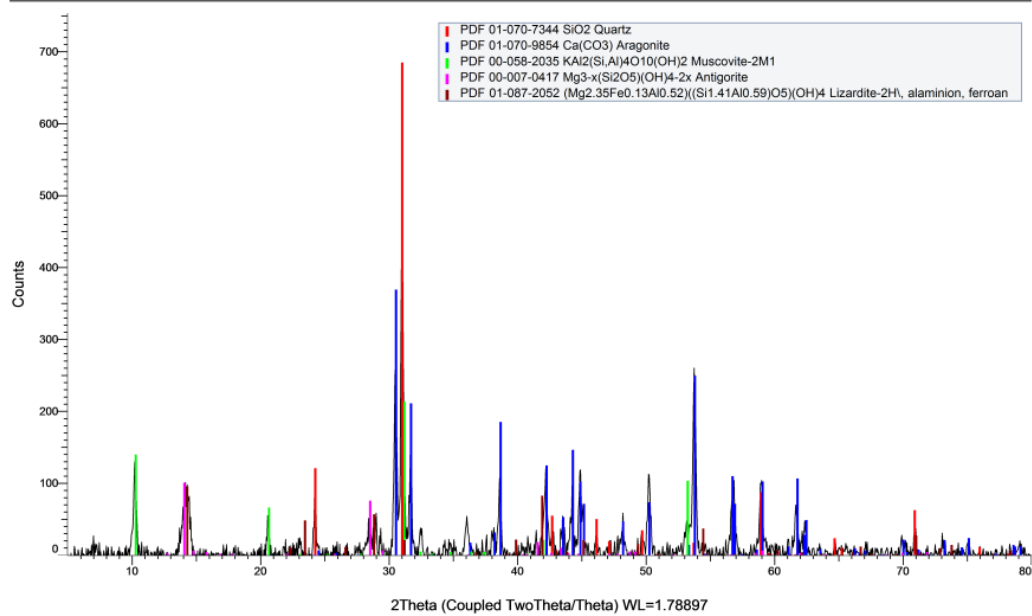
Figure 15. CC3 XRD data
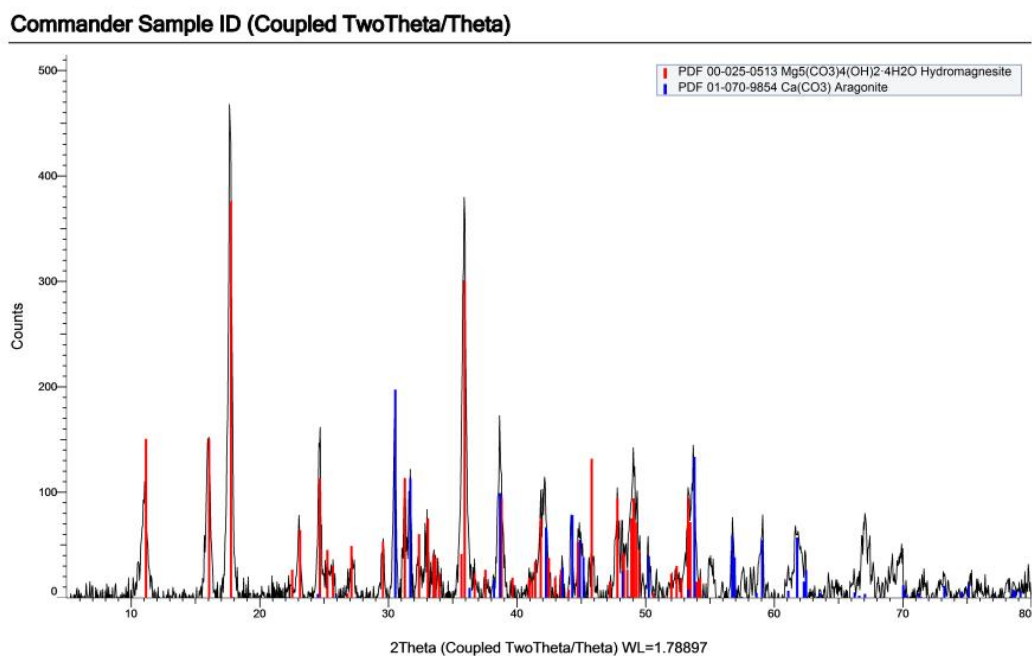
2128

2129   **Figure 16.** LAL-C3 XRD data
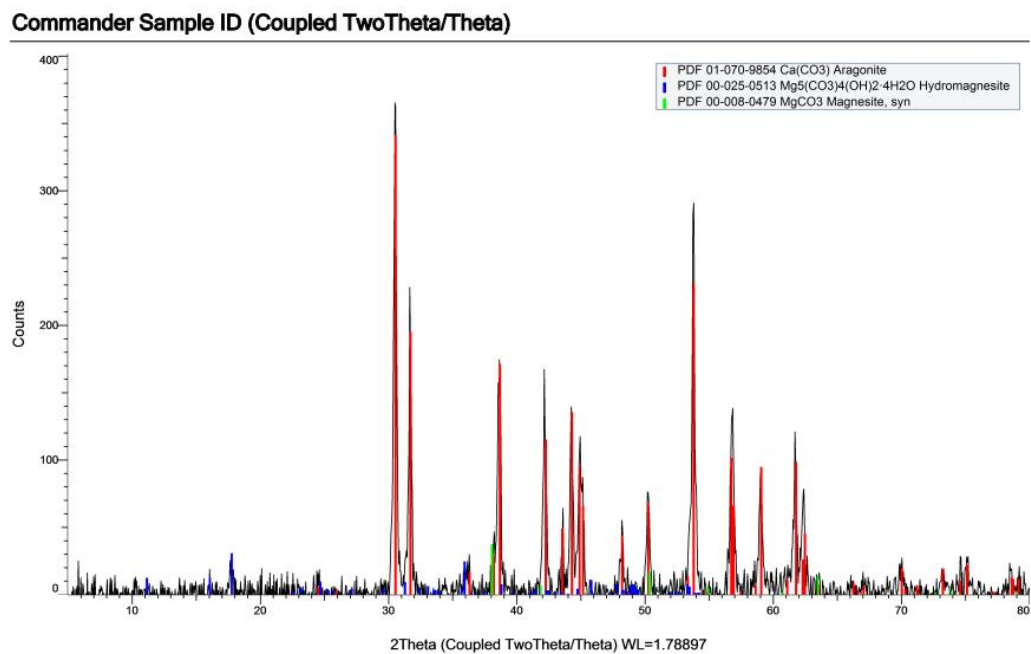
2130

2131   **Figure 17.** LAL-E3 XRD data
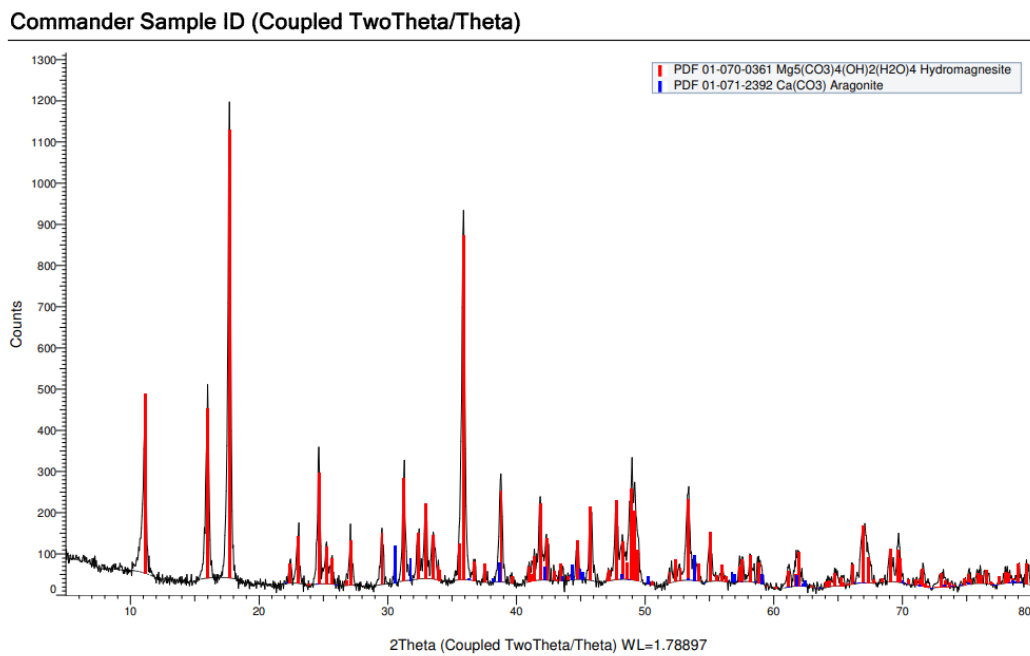
2132

2133   **Figure 18.** LS3 XRD data

2134

2135